TECHNISCHE UNIVERSITÄT WIEN

AUTOMATION & CONTROL INSTITUTE
INSTITUT FÜR AUTOMATISIERUNGS- & REGELUNGSTECHNIK

Modeling and control of a hydraulically operated manipulator for autonomous timber loading

DIPLOMA THESIS

Conducted in partial fulfillment of the requirements for the degree of a

Diplom-Ingenieur (Dipl.-Ing.)

supervised by

Dipl.-Ing. A. Lobe
Dipl.-Ing. C. Fröhlich
Assoc. Prof. Dr. techn. W. Kemmetmüller

submitted at the

TU Wien
Faculty of Electrical Engineering and Information Technology
Automation and Control Institute

by
Amanzhol Salykov
Matriculation number e01528454

Vienna, January 2025

Complex Dynamical Systems Group
A-1040 Wien, Gußhausstr. 27–29, Internet: https://www.acin.tuwien.ac.at

Die approbierte gedruckte Originalversion dieser Diplomarbeit ist an der TU Wien Bibliothek verfügbar
The approved original version of this thesis is available in print at TU Wien Bibliothek.
TU Bibliothek Your knowledge hub WIEN

Preamble

This master's thesis was conducted at the Austrian Institute of Technology in collaboration with the Automation and Control Institute of TU Wien.

First and foremost, I wish to express my profound gratitude to my supervisors, Dipl.-Ing. Amadeus-Cosimo Lobe, Dipl.-Ing. Christoph Fröhlich and Assoc. Prof. Dr.-Ing. Wolfgang Kemmetmüller, for their invaluable expertise, constructive feedback, and unwavering support throughout this work. I am also grateful to the Austrian Institute of Technology and the Automation and Control Institute of TU Wien for providing me with the opportunity and resources to conduct this master's thesis.

Finally, I would like to thank my parents and family for their endless love and support. Their belief in me has been a constant source of motivation.

Vienna, January 2025

Die approbierte gedruckte Originalversion dieser Diplomarbeit ist an der TU Wien Bibliothek verfügbar
The approved original version of this thesis is available in print at TU Wien Bibliothek.

Abstract

This thesis focuses on the mathematical modeling and model-based control of the inner boom of a forestry crane *Palfinger Epsilon TZ17*. Forestry cranes are essential for modern logging operations, yet their manual operation poses challenges such as high operator workload, reduced efficiency, and variability in performance. The automation of forestry cranes offers the potential to address these issues by improving productivity, optimizing energy consumption, and reducing operator stress.

A mathematical model is proposed to accurately represent the hydraulic system of the crane's inner boom, incorporating hydraulic components such as a pressure-compensated directional control valve, a hose burst valve and hydraulic accumulators. The model is derived from first principles, with unknown parameters estimated through parameter identification techniques, ensuring accurate representation of the system's dynamics across a broad range of operating conditions. Finally, the mathematical model is validated using experimental data in a simulation environment.

The validated model serves as the foundation for designing a model-based tracking controller. This controller employs a cascade structure, combining feedforward and feedback control strategies to regulate the motion of the inner boom for precise trajectory tracking. Robustness tests are conducted to evaluate the controller's performance under varying system parameters, including the pre-charge pressure in the hydraulic accumulators, oil bulk modulus, cylinder friction, and load mass. The results demonstrate the effectiveness of the modeling approach in capturing the system dynamics and applicability of the controller strategy for accurate and robust trajectory tracking.

Die approbierte gedruckte Originalversion dieser Diplomarbeit ist an der TU Wien Bibliothek verfügbar
The approved original version of this thesis is available in print at TU Wien Bibliothek.

Kurzzusammenfassung

Die vorliegende Arbeit beschäftigt sich mit der mathematischen Modellierung und modellbasierten Regelung des Hauptarms eines Forstkrans *Palfinger Epsilon TZ17*. Forstkräne sind für den modernen Holzeinschlag unverzichtbar, doch ihr manueller Betrieb birgt Probleme wie hohe Arbeitsbelastung des Fahrers, geringere Effizienz und Leistungsschwankungen. Die Automatisierung von Forstkränen bietet das Potenzial, diese Probleme zu lösen, indem sie die Produktivität steigert, den Energieverbrauch optimiert und die Belastung der Bediener reduziert.

Im Rahmen dieser Arbeit wird das Hydrauliksystem des Hauptarms des Krans mathematisch modelliert, wobei hydraulische Komponenten wie ein druckkompensiertes Wegeventil, ein Schlauchbruchventil und hydraulische Speicher im Modell inkludiert werden. Das mathematische Modell wird aus physikalischen Prinzipien hergeleitet und die unbekannten Parameter werden mittels Identifikationsmethoden geschätzt, um eine genaue Beschreibung der Systemdynamik über ein breites Spektrum von Betriebsbedingungen sicherzustellen. Schließlich wird das mathematische Modell anhand von experimentellen Daten in einer Simulationsumgebung validiert.

Des Weiteren wird das validierte Modell für den Entwurf eines modellbasierten Trajektorienfolgereglers verwendet. Dieser Regler hat eine Kaskadenstruktur, die Feedforward- und Feedback-Regelungsstrategien kombiniert, um die Bewegung des Hauptarms entlang gewünschter Solltrajektorien zu stabilisieren. Anschließend wird das Regelungskonzept auf Robustheit und Stabilität in einer Simulationsumgebung untersucht, indem die Modellparameter wie der Vorfülldruck im Speicher, der Kompressionsmodul, die Zylinderreibung und die Lastmasse variiert werden. Die Ergebnisse zeigen die Effektivität des Modellierungsansatzes bei der Erfassung der Systemdynamik sowie die Anwendbarkeit der Regelungsstrategie für präzise und robuste Trajektorienfolgeregelung.

Die approbierte gedruckte Originalversion dieser Diplomarbeit ist an der TU Wien Bibliothek verfügbar
The approved original version of this thesis is available in print at TU Wien Bibliothek.

Contents

Die approbierte gedruckte Originalversion dieser Diplomarbeit ist an der TU Wien Bibliothek verfügbar
The approved original version of this thesis is available in print at TU Wien Bibliothek.

List of Figures

Die approbierte gedruckte Originalversion dieser Diplomarbeit ist an der TU Wien Bibliothek verfügbar
The approved original version of this thesis is available in print at TU Wien Bibliothek.
TU Bibliothek Your knowledge hub WIEN

Die approbierte gedruckte Originalversion dieser Diplomarbeit ist an der TU Wien Bibliothek verfügbar
The approved original version of this thesis is available in print at TU Wien Bibliothek.
TU Bibliothek Your knowledge hub WIEN

List of Tables

Die approbierte gedruckte Originalversion dieser Diplomarbeit ist an der TU Wien Bibliothek verfügbar
The approved original version of this thesis is available in print at TU Wien Bibliothek.

1 Introduction

Forestry cranes play a critical role in modern logging and timber transport operations, enabling efficient handling of heavy loads in challenging outdoor environments. Despite their importance, the operation of these machines often relies heavily on manual control, requiring skilled operators to perform complex tasks under varying conditions. During daily operations, the driver is required to manage multiple tasks simultaneously, including visualizing the work area, recognizing and selecting targets, controlling the crane, and positioning the vehicle [1]. This high level of demand can be extremely stressful, as the operator must process an overwhelming amount of information and make rapid decisions under pressure. The reliance on human expertise introduces variability in efficiency, productivity, and safety. There is increasing interest in automating these machines to improve efficiency, optimize fuel consumption, and reduce operator stress. As the demand for sustainable forestry practices grows, so does the need for advanced, automated control systems [2].

Manual open-loop control of cranes is a well-established technology that has been in use for over two decades [3]. These systems typically consist of a mechanical manipulator actuated by hydraulic cylinders, which generate motion and are controlled via hydraulic valves. The operator manually controls the crane from within the cabin using joysticks and buttons. However, since neither the crane nor the vehicle is equipped with sensors, managing all degrees of freedom becomes a complex and demanding task. This lack of feedback leads to a system that is unintuitive and difficult to operate [3].

Research on alternative crane control modes has been ongoing for decades with most efforts focused on simplifying control complexity by directly commanding the end-effector's motion rather than controlling each individual link [1, 2]. This shift is already evident in the emergence of commercial solutions, including cranes equipped with Cartesian end-effector control capabilities [4, 5].

These systems provide incremental improvements but still depend heavily on human input. To address this issue, recent research efforts have focused on full automation of forestry cranes. Such control systems aim to eliminate the need for continuous operator intervention by employing sensors, actuators, and advanced control algorithms [6].

Model-free PID controllers, which resemble conventional decentralized joint control, are a classical approach widely discussed in the literature for motion control of hydraulic manipulators [6–10]. These controllers are often favored for their simplicity of implementation. However, experimental studies show that their efficiency is restricted to slow-velocity trajectories [7]. As motion speeds increase to match human-level profiles, these controllers struggle with accuracy and stability. Furthermore, model-free control lacks the robustness to handle significant variations in system parameters and external disturbances, limiting its applicability in real-world scenarios [3].

To enhance performance, there is growing interest in model-based motion control strate-

Die approbierte gedruckte Originalversion dieser Diplomarbeit ist an der TU Wien Bibliothek verfügbar
The approved original version of this thesis is available in print at TU Wien Bibliothek.
TU Bibliothek Your knowledge hub WIEN

gies that leverage mathematical models of the manipulator's hydraulic and mechanical systems. For instance, in [7], the hydraulic torque was modeled as a fourth-order transfer function relating input current to the force generated by the cylinders. While this approach is computationally simple, it overlooks the inherent nonlinearities of hydraulic systems, leading to poor performance under fast-varying trajectories or significant deviations from operating point.

To address these shortcomings, [11] proposed a more detailed mathematical model derived from first principles, incorporating cylinder pressure dynamics and nonlinear flow equations. However, this model omitted certain dynamics, such as valve behavior and nonlinear orifice areas, by assuming a direct mapping between electrical input and spool position. Building on this, [12] improved the hydraulic system model by accounting for valve nonlinearities, including dead zones and saturation.

Industrial hydraulic valves often feature additional service functions - such as pressure-relief, anti-cavitation valves, load-sensing mechanisms, and pressure compensators. While some components, such as safety valves, have minimal impact on system dynamics, others, like pressure compensators, can significantly alter the system's behavior. Additionally, modern forestry cranes often include components like hydraulic accumulators and hose burst valves, which further impact system performance [10, 13, 14].

This work presents a mathematical model of the hydraulic system for the inner boom of a forestry crane *Palfinger Epsilon TZ17*. The goal is to accurately represent the system's behavior across a wide range of operating points and develop a tracking controller based on this model. A key distinction from previous works is the inclusion of a two-stage pressure-compensated directional control valve, hydraulic accumulators, and a hose burst valve in the model. The mathematical model is validated against experimental data in a simulation environment and subsequently used to design a model-based tracking controller with the goal to control the position of the inner boom. The tracking controller utilizes a cascade structure, where the inner loop regulates the hydraulic force in the cylinder, and the outer loop controls the position of the inner boom. The controller is subsequently validated in simulations under varying model parameters to test the robustness of the control strategy and it's applicability for real-world scenarios.

This thesis is organized as follows: Chapter 2 describes the setup under study and gives a short overview of the hydraulic components of the system. Chapter 3 presents the mathematical models of the mechanical and hydraulic systems of the inner boom. Chapter 4 provides a detailed explanation of the measurements conducted in this work, along with descriptions of their respective physical setups. Chapter 5 covers the parameter estimation and system identification of the hydraulic components, as well as the validation of the mathematical model in MATLAB/SIMULINK. Chapter 6 presents the design of the tracking controller and discusses the results of the robustness tests conducted to evaluate its performance under varying model parameters. Conclusions are drawn in Chapter 7.

Die approbierte gedruckte Originalversion dieser Diplomarbeit ist an der TU Wien Bibliothek verfügbar
The approved original version of this thesis is available in print at TU Wien Bibliothek.
TU Bibliothek Your knowledge hub WIEN

2 System Overview

The setup under study is the inner boom of a forestry crane *Palfinger Epsilon TZ17* [15]. Figure 2.1 shows a schematic illustration of the hydraulic manipulator. Modeled as a rigid body, the position and orientation of the crane can be fully described by eight degrees of freedom. The manipulator is an underactuated system, where only six degrees of freedom are directly actuated by means of the hydraulic linear and rotary actuators. The inner boom, outer boom and telescope hydraulic linear actuators are depicted in the figure, whereas the rotary actuators are not shown for simplicity.

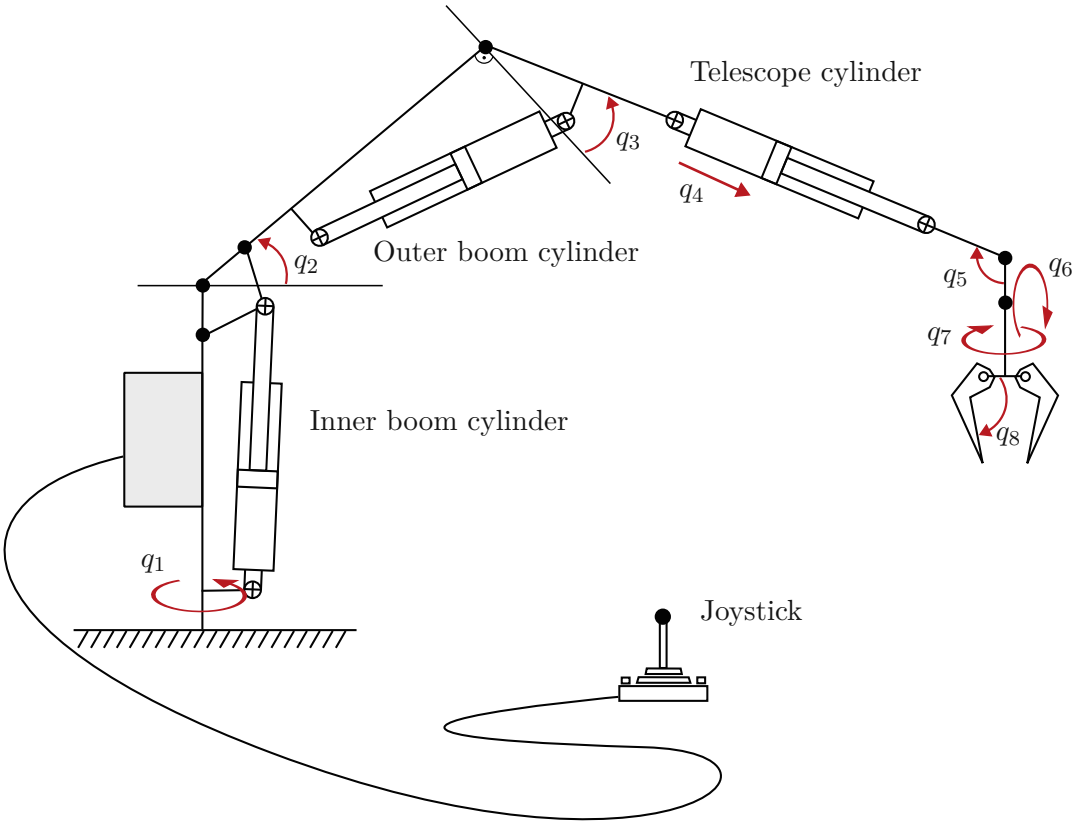

Figure 2.1: Schematic illustration of the hydraulic manipulator.

The hydraulic manipulator is equipped with *Paltronic* - control electronics from *Palfinger*, offering safety and assistance functionalities [16]. This system monitors and controls the crane, allowing it to be operated using a handheld joystick. The manipulator's electronic control units, sensors, and actuators communicate via a Controller Area Network (CAN) bus.

Die approbierte gedruckte Originalversion dieser Diplomarbeit ist an der TU Wien Bibliothek verfügbar
The approved original version of this thesis is available in print at TU Wien Bibliothek.
TU Bibliothek Your knowledge hub WIEN

The original hydraulic circuit of the inner boom, provided by the manufacturer, contains numerous components that are part of the hydraulic system. However, not all of them are equally relevant for mathematical modeling of the hydraulic system. For example, some components are required to ensure safe operation and are only active when the system's state reaches extreme, abnormal values. Therefore, the first step is to identify key components that represent the system dynamics in the operating range. After analyzing the original hydraulic circuit, a simplified version of the circuit is derived where only relevant components are included. Figure 2.2 shows the simplified hydraulic circuit of the inner boom. The hydraulic circuit consists of a pressure-compensated directional control valve, a hydraulic cylinder with integrated hose burst valve and two hydraulic accumulators.

The main valve is a two-stage pressure-compensated directional control valve *Parker K220LS* [17]. The first or pilot stage consists of two small solenoid-operated proportional pressure control valves. The pilot valves adjust the pilot control pressures proportionally to the applied electrical signal. The second or main stage of the valve consists of a larger valve that is controlled by the pilot valves. Pilot control pressure acts on the main valve spool, causing it to move and control the flow rate proportionally to the pilot control pressure. In this way, the pilot valves efficiently convert low-energy electrical signals into high-power fluid flow through the valve. The main valve is connected to the system supply pressure, whereas the pilot valves are connected to a separate pilot supply pressure, much lower than the system supply pressure. The main valve features a pre-installed pressure compensator, which ensures that the flow rate through the valve remains constant, even if the load pressure changes. The pressure compensator senses the pressure difference between the inlet and outlet ports of the valve and accordingly adjusts the orifice size of the supply port to keep the flow rate through the valve constant.

At the time of conducting the work, the model of the pilot valves was not available. As the valves are integrated within the main valve housing, they cannot be visually inspected. This lack of access precludes the derivation of a mathematical model from first principles, as neither geometrical parameters nor internal construction details are available. To overcome this limitation, the mathematical model of the pilot valves is estimated based on measured data using system identification techniques. The acquisition of this data and the subsequent model identification process will be discussed in detail in Chapter 4 and Chapter 5.

To lift, push and pull heavy loads, each link of the hydraulic manipulator contains a hydraulic cylinder. The hydraulic cylinders are designed in a single-rod, double-acting configuration so that the piston can be moved in both directions. When pressurized fluid enters the head side of the cylinder, it pushes the piston towards the rod side, extending the rod. Simultaneously, fluid from the rod side exits through the opposite port, allowing the piston to move freely. To retract the piston, fluid pressure is applied to the rod side while the head side serves as exhaust.

The hydraulic cylinder features a pre-installed hose burst valve *HAWE SB39* that reside in the piston side of the cylinder housing. The primary function of the hose burst valve is to enhance safety by automatically blocking the hydraulic flow if a sudden drop in pressure is detected, typically due to a hose or pipe burst. If a hose supplying hydraulic fluid to the boom actuator bursts, the hose burst valve prevents the boom from collapsing

Die approbierte gedruckte Originalversion dieser Diplomarbeit ist an der TU Wien Bibliothek verfügbar
The approved original version of this thesis is available in print at TU Wien Bibliothek.
TU Bibliothek Your knowledge hub WIEN

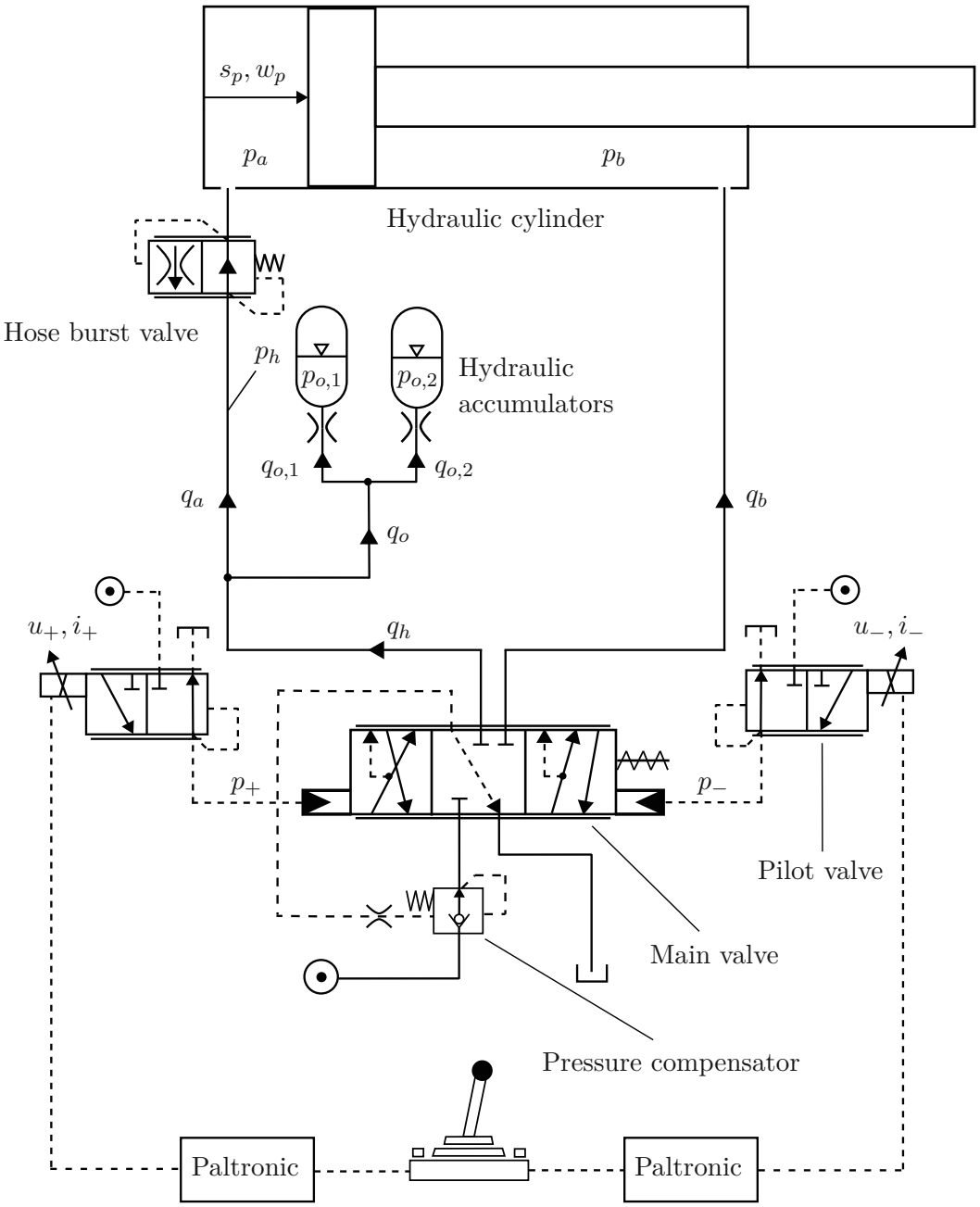

Figure 2.2: Hydraulic system of the inner boom.

Die approbierte gedruckte Originalversion dieser Diplomarbeit ist an der TU Wien Bibliothek verfügbar
The approved original version of this thesis is available in print at TU Wien Bibliothek.

by locking the fluid in the actuator. The hose burst valve behaves differently depending on the flow direction. During extension of the cylinder rod, hydraulic fluid flows through the valve to the head side of the cylinder without restriction. However, during retraction of the cylinder, the volumetric flow through the valve is limited and maintained constant after reaching some predefined threshold value. The threshold value of the valve is set to 130 L/min.

The hydraulic system of the inner boom also includes two *HYDAC* hydraulic accumulators connected to the head side of the cylinder. Both hydraulic accumulators are diaphragm accumulators filled with nitrogen as storing compressible gas. Accumulators store energy when the hydraulic system's demand is low and release it when the demand increases. They help to smooth out pulsations and fluctuations in pressure caused by pump operation or varying load conditions. This leads to more stable and reliable system performance. The hydraulic accumulators are pressurized to 55 bar and 75 bar. Additionally, two flow restrictors with diameter of 1.5 mm and 2 mm are placed in the fluid ports of the hydraulic accumulators.

In the following chapter, the hydraulic components of the inner boom's hydraulic system will be discussed, and mathematical models for these components will be derived. Throughout this work, the crane will be modeled as a single-link system, with only the inner boom cylinder actuated, while all other cylinders remain stationary.

Die approbierte gedruckte Originalversion dieser Diplomarbeit ist an der TU Wien Bibliothek verfügbar
The approved original version of this thesis is available in print at TU Wien Bibliothek.
TU Bibliothek Your knowledge hub WIEN

3 Mathematical Modeling

This chapter introduces the mathematical models of the mechanical and hydraulic systems of the inner boom. Treating the hydraulic manipulator as a rigid body, its equations of motion will be formulated using the Euler-Lagrange equations. Assuming a single-link configuration, these equations will be simplified into a single equation of motion that captures the dynamics of the inner boom link. Furthermore, the mathematical models for the hydraulic cylinder, main valve, pilot valves and hydraulic accumulators will be presented.

3.1 Rigid Body Dynamics

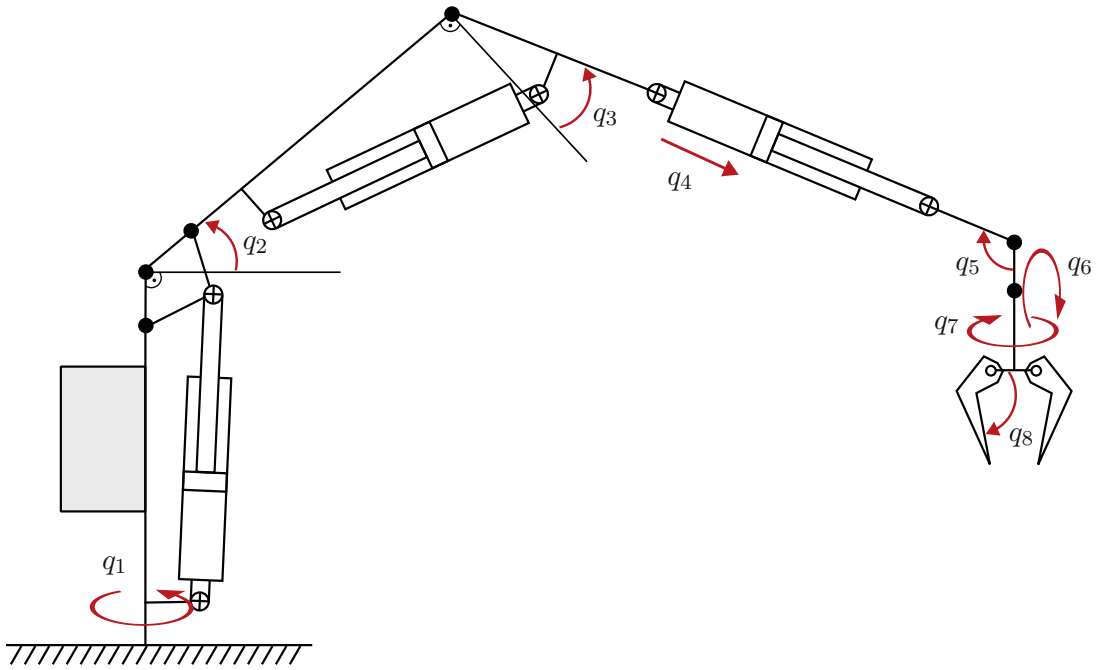

Figure 3.1: Schematic illustration of the hydraulic manipulator.

Modeled as a rigid multi-body system, the dynamics of the hydraulic manipulator in Figure 3.1 can be described by the Euler-Lagrange equations [3, 18]. The computation of the Euler-Lagrange equations of motion leads to:

$$\mathbf{D}(\mathbf{q})\ddot{\mathbf{q}} + \mathbf{C}(\mathbf{q}, \dot{\mathbf{q}})\dot{\mathbf{q}} + \mathbf{g}(\mathbf{q}) = \boldsymbol{\tau} - \boldsymbol{\tau}_f, \tag{3.1}$$

Die approbierte gedruckte Originalversion dieser Diplomarbeit ist an der TU Wien Bibliothek verfügbar
The approved original version of this thesis is available in print at TU Wien Bibliothek.
TU Bibliothek Your knowledge hub WIEN

where $\mathbf{D}(\mathbf{q})$ denotes the positive-definite, symmetric mass matrix, $\mathbf{C}(\mathbf{q}, \dot{\mathbf{q}})$ the matrix of Coriolis forces, $\mathbf{g}(\mathbf{q})$ the vector of potential forces, $\boldsymbol{\tau}$ the vector of generalized input torques, $\boldsymbol{\tau}_f$ the vector of friction torques and $\mathbf{q}^{\mathrm{T}} = \begin{bmatrix} q_1 & q_2 & \dots & q_8 \end{bmatrix}$ the vector of generalized coordinates. Since in this work only the inner boom is analyzed and all the other links remain fixed during experiments, the vector of generalized coordinates and its derivatives can be described as

$$\mathbf{q} = \begin{bmatrix} q_{1,0} & q_2 & q_{3,0} & \dots & q_{8,0} \end{bmatrix}^{\mathrm{T}} \tag{3.2a}$$

$$\dot{\mathbf{q}} = \begin{bmatrix} 0 & \dot{q}_2 & 0 & \dots & 0 \end{bmatrix}^{\mathrm{T}} \tag{3.2b}$$

$$\ddot{\mathbf{q}} = \begin{bmatrix} 0 & \ddot{q}_2 & 0 & \dots & 0 \end{bmatrix}^{\mathrm{T}}. \tag{3.2c}$$

The set of equations (3.1) can be simplified to a single equation describing the dynamics of the inner boom. Furthermore, it can be shown that $D_{22}(q_2) = D_{22}$ for all q_2 and the matrix entry $C_{22}(\mathbf{q}, \dot{\mathbf{q}}) = 0$ for all $\mathbf{q}$ and $\dot{\mathbf{q}}$. These considerations lead to

$$D_{22}\ddot{q}_2 + g_2(q_2) = \tau_2 - \tau_{f,2}, \tag{3.3}$$

or with omitted subscripts for better readability:

$$D\ddot{q}_2 + g(q_2) = \tau - \tau_f, \tag{3.4}$$

For this work, $\mathbf{D}(\mathbf{q})$ and $\mathbf{g}(\mathbf{q})$ are provided by *AIT* in the form of MATLAB functions and can be evaluated numerically at any given point $\mathbf{q}$.

The friction force in the hydraulic cylinder is modeled and estimated in the configuration space. A model often used to represent friction torque is a combination of viscous and Coulomb frictions [3, 19]. Viscous friction is proportional to the angular velocity, whereas Coulomb friction depends on the direction of motion

$$\tau_f(\dot{q}_2) = \tau_C \operatorname{sgn}(\dot{q}_2) + k_v \dot{q}_2, \tag{3.5}$$

with the Coulomb friction τ_C and the viscous friction coefficient k_v. The Coulomb term in (3.5) is a discontinuous function of $\dot{q}_2$, which necessitates small step sizes when using variable-step solvers, resulting in longer simulation times. To avoid this, the Coulomb term is approximated by differentiable tanh function

$$\tau_f(\dot{q}_2) = \tau_C \tanh\left(\frac{\dot{q}_2}{\sigma}\right) + k_v \dot{q}_2, \tag{3.6}$$

with a tunable constant parameter σ.

Many real hydraulic systems exhibit asymmetric friction forces. The model of the friction torque is therefore extended to be able to model such asymmetry

$$\tau_f = \begin{cases} \tau_{C_+} \tanh\left(\dfrac{\dot{q}_2}{\sigma}\right) + k_{v_+} \dot{q}_2, & \text{if } \dot{q}_2 \geq 0, \\ \tau_{C_-} \tanh\left(\dfrac{\dot{q}_2}{\sigma}\right) + k_{v_-} \dot{q}_2, & \text{if } \dot{q}_2 < 0. \end{cases} \tag{3.7}$$

Die approbierte gedruckte Originalversion dieser Diplomarbeit ist an der TU Wien Bibliothek verfügbar
The approved original version of this thesis is available in print at TU Wien Bibliothek.
TU Bibliothek Your knowledge hub WIEN

3.2 Hydraulic System

3.2.1 Hydraulic Cylinder

Figure 3.2 shows a hydraulic cylinder that is designed in a single-rod, double-acting configuration. It operates by utilizing hydraulic pressure to move the piston in both directions. When pressurized fluid enters the head side of the cylinder, it pushes the piston towards the rod side, extending the rod. To retract the piston, fluid pressure is applied to the rod side while the head side serves as the exhaust [20].

To derive a mathematical model of the hydraulic cylinder the continuity equation is applied to each of the cylinder chambers, which yields [19]

$$q_a = \dot{V}_a + \frac{V_a}{\beta}\dot{p}_a \tag{3.8a}$$

$$q_b = \dot{V}_b + \frac{V_b}{\beta}\dot{p}_b, \tag{3.8b}$$

where V_a and V_b are the chamber volumes, q_a and q_b describe the flows in each chamber, p_a and p_b are the pressures in the chambers and β is the bulk modulus of the oil.

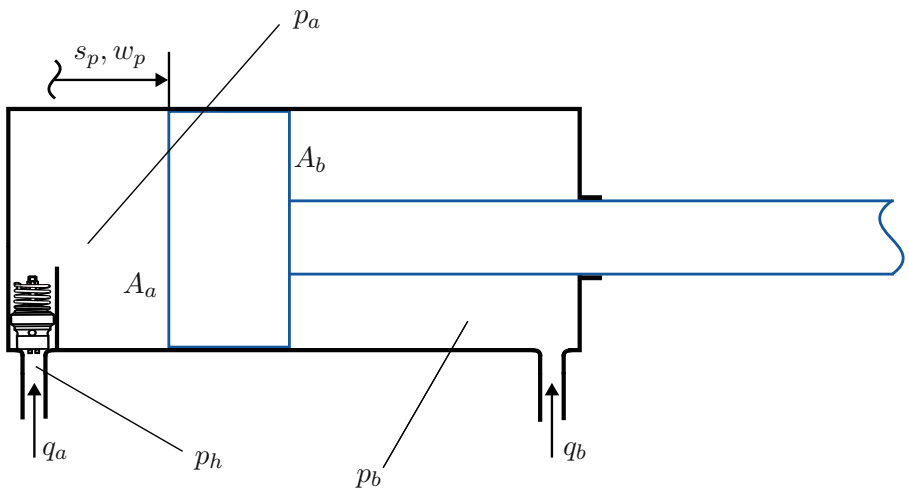

Figure 3.2: Schematic diagram of a double-acting hydraulic cylinder with single rod.

The chamber volumes can be written as

$$V_a = V_{0,a} + s_p A_a \tag{3.9a}$$

$$V_b = V_{0,b} + (l_p - s_p)A_b, \tag{3.9b}$$

with s_p being the piston position, A_a, A_b the effective piston areas, $V_{0,a}, V_{0,b}$ the dead volumes in the chambers and l_p the stroke length. The piston position is limited to $s_p \in [0, l_p]$. The time derivative of (3.9) is given by

$$\dot{V}_a = \dot{s}_p A_a = w_p A_a \tag{3.10a}$$

$$\dot{V}_b = -\dot{s}_p A_b = -w_p A_b. \tag{3.10b}$$

Die approbierte gedruckte Originalversion dieser Diplomarbeit ist an der TU Wien Bibliothek verfügbar
The approved original version of this thesis is available in print at TU Wien Bibliothek.
TU Bibliothek Your knowledge hub WIEN

By substituting (3.10) and (3.9) into (3.8), the pressure dynamics equations can be calculated as

$$\dot{p}_a = \frac{\beta}{V_{0,a} + s_p A_a}(q_a - w_p A_a), \tag{3.11a}$$

$$\dot{p}_b = \frac{\beta}{V_{0,b} + (l_p - s_p) A_b}(q_b + w_p A_b). \tag{3.11b}$$

Following the schematic illustration from the Figure 3.2, the actuator force, generated by the hydraulics, can be computed from the chamber pressures via

$$f_p = p_a A_a - p_b A_b. \tag{3.12}$$

The mapping $s_p(q_2)$ between the piston position s_p and the angular position of the inner boom q_2 can be used to calculate s_p and $\dot{s}_p$ from the measurements of the angular position q_2 and velocity $\dot{q}_2$ by

$$s_p = s_p(q_2), \tag{3.13a}$$

$$\dot{s}_p = \frac{\partial s_p(q_2)}{\partial q_2}\dot{q}_2 = J(q_2)\dot{q}_2, \tag{3.13b}$$

where $J(q_2)$ denotes the geometric manipulator Jacobian. Additionally, the geometric manipulator Jacobian is used to connect the hydraulic and mechanical systems by mapping the measurable hydraulic actuator force to the input mechanical torque

$$\tau = J(q_2) f_p = J(q_2)(p_a A_a - p_b A_b). \tag{3.14}$$

By substituting (3.14) into (3.4), the equation of motion of the inner boom is formulated as

$$D\ddot{q}_2 + g(q_2) = J(q_2)(p_a A_a - p_b A_b) - \tau_f(\dot{q}_2). \tag{3.15}$$

3.2.2 Hydraulic Accumulators

Fluids are extremely poorly compressible and, as a result, cannot store pressure energy [10]. In hydraulic accumulators, the compressibility of gases is leveraged to store energy. Diaphragm accumulators operate on this principle, using nitrogen as the compressible medium [10]. These accumulators have two sections: a fluid section and a gas section, separated by a gas-tight diaphragm. The fluid section is connected to the hydraulic circuit, allowing the diaphragm accumulator to draw in fluid when pressure increases, compressing the gas. When the pressure decreases, the compressed gas expands, pushing the stored fluid back into the circuit. Figure 3.3 depicts a schematic diagram of the diaphragm hydraulic accumulators used in the hydraulic system. The subscripts 1 and 2 are used to distinguish between the two hydraulic accumulators. However, since both hydraulic accumulators are of the same type and model, the subscripts will be omitted in the following derivation of the mathematical model, and the derived equations will apply to both hydraulic accumulators.

Die approbierte gedruckte Originalversion dieser Diplomarbeit ist an der TU Wien Bibliothek verfügbar
The approved original version of this thesis is available in print at TU Wien Bibliothek.
TU Bibliothek Your knowledge hub WIEN

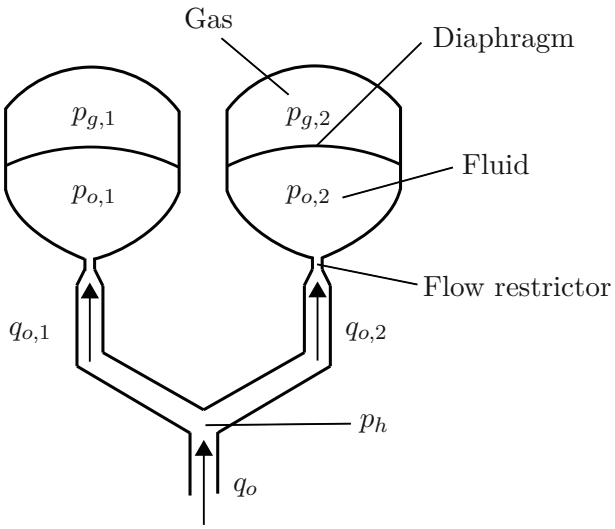

Figure 3.3: Schematic diagram of the diaphragm accumulators used in the hydraulic system.

Given that no force is required to deform the diaphragm, the pressures in the gas and fluid sections are equal, $p_g = p_o$. The gas in the accumulator is initially precharged to the pressure p_{g0} and the volume V_{g0}. Assuming that there is no heat exchange with the environment and all thermodynamic processes are reversible, the relationship between the pressure and the volume of the gas can be described by the adiabatic equation [21]

$$p_g V_g^{\kappa} = p_{g0} V_{g0}^{\kappa} = \zeta_0 = \text{const.} \tag{3.16}$$

Here κ denotes the isentropic exponent of the gas and p_g, V_g represent the current pressure and volume of the gas, respectively. For ideal diatomic gases the isentropic exponent is calculated as $\kappa = 7/5$ and is constant [22]. However, for real gases as nitrogen the isentropic exponent depends on pressure and temperature. In practice, the operation of a hydraulic accumulator typically involves only slight fluctuations in pressure and temperature. Therefore, an approximation using constant isentropic exponent κ provides sufficiently accurate description of gas behaviour [13]. By applying the mass continuity equation on the fluid section of the hydraulic accumulator

$$\frac{\mathrm{d}}{\mathrm{d}t}(\rho V_o) = \rho q_o, \tag{3.17}$$

the mathematical model of the hydraulic accumulator can be derived as:

$$\frac{\mathrm{d}}{\mathrm{d}t}(\rho V_o) = \left(\frac{\mathrm{d}\rho}{\mathrm{d}t}\right) V_o + \rho \frac{\mathrm{d}V_o}{\mathrm{d}t} = \frac{\partial \rho}{\partial p_o}\left(\frac{\mathrm{d}p_o}{\mathrm{d}t}\right) V_o + \rho \frac{\mathrm{d}V_o}{\mathrm{d}t} = \frac{1}{\beta}\left(\frac{\mathrm{d}p_o}{\mathrm{d}t}\right) V_o + \rho \frac{\mathrm{d}V_o}{\mathrm{d}t}, \tag{3.18a}$$

$$\frac{\mathrm{d}V_o}{\mathrm{d}t} = -\frac{\mathrm{d}V_g}{\mathrm{d}t} = -\frac{\mathrm{d}}{\mathrm{d}t}\left[\left(\frac{\zeta_0}{p_o}\right)^{\frac{1}{\kappa}}\right] = \frac{1}{\kappa}\left(\frac{1}{\zeta_0}\right)^{-\frac{1}{\kappa}} p_o^{-\frac{1}{\kappa}-1} \frac{\mathrm{d}p_o}{\mathrm{d}t}. \tag{3.18b}$$

Die approbierte gedruckte Originalversion dieser Diplomarbeit ist an der TU Wien Bibliothek verfügbar
The approved original version of this thesis is available in print at TU Wien Bibliothek.
TU Bibliothek Your knowledge hub WIEN

Substituting (3.18b) into (3.18a) and using the fact that $V_o = V_{g0} - V_g$, the pressure dynamics of the fluid is described as [13]:

$$\frac{\mathrm{d}}{\mathrm{d}t}p_o = \frac{\kappa\beta p_o q_o}{\kappa p_o V_{g0} + (\beta - \kappa p_o)\left(\frac{\zeta_0}{p_o}\right)^{\frac{1}{\kappa}}}. \tag{3.19}$$

Orifice flow restrictors are placed in the ports of the hydraulic accumulators. The orifice equation for turbulent flow describes the flow rate through the orifices

$$q_o = \begin{cases} 0, & \text{if } p_o \leq p_{g0}, \\ \operatorname{sign}(p_h - p_o) C_d \frac{\pi d^2}{4}\sqrt{\frac{2}{\rho}}\sqrt{|p_h - p_o|}, & \text{otherwise}, \end{cases} \tag{3.20}$$

where C_d denotes the discharge coefficient and d the internal orifice diameter.

3.2.3 Main Valve

Figure 3.4 shows a schematic representation of the main valve. The valve is a 4/3 directional control valve in closed-center configuration with the spool position controlled by pilot control pressures p_+ and p_-. The main valve has four ports: supply port s, tank port t, actuator ports a and b. The position of the spool s_s determines one of three possible flow paths. In the neutral position $s_s = 0$ all orifices are closed to flow, ensuring that the hydraulic cylinder is held in place. For negative spool displacement $s_s < 0$, the valve connects the pressure port to the actuator port a, and the actuator port b is connected to the tank. This allows the fluid to flow from the supply port s to the port a, causing the cylinder to extend. Conversely, if $s_s > 0$, the valve connects the pressure port s to the actuator port b, and the actuator port a is connected to the tank. This reverses the flow, moving the hydraulic cylinder in the opposite direction [19, 23].

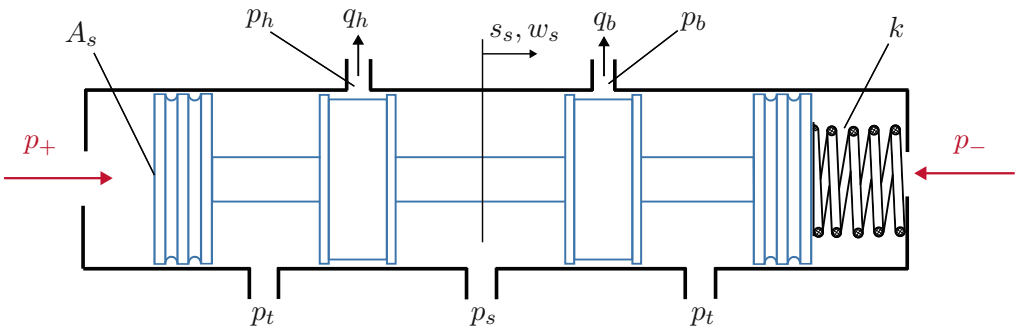

Figure 3.4: Schematic diagram of the main valve actuated by proportional pressure control pilot valves.

By summing up the forces exerted on the spool and applying Newton's second law, the equation of motion of the spool can be expressed as:

$$m_s \ddot{s}_s + k s_s = (p_+ - p_-)A_s - f_f, \tag{3.21}$$

Die approbierte gedruckte Originalversion dieser Diplomarbeit ist an der TU Wien Bibliothek verfügbar
The approved original version of this thesis is available in print at TU Wien Bibliothek.

where m_s denotes the mass of the spool, k the stiffness of return spring, A_s the cross-sectional area of the spool, s_s the position of the spool and f_f the friction force. The friction force is modeled as a function of spool velocity $\dot{s}_s$ and is assumed to be the sum of Coulomb, and viscous components:

$$f_f = d_v \dot{s}_s + f_c \tanh\left(\frac{\dot{s}_s}{\sigma_s}\right), \tag{3.22}$$

with constant parameters d_v, f_c and σ_s. Additionally, an axial steady-state flow force acts on the valve spool. However, because the spool displacement is not measurable and existing mathematical models provide only a rough approximation of this force, the effect of the flow force on the spool is neglected.

The spool position determines the area of the orifices and therefore the flow rate through the valve. The flow rate is described using the orifice equation for turbulent flow, which takes the direction of the pressure drop into account [19]:

$$q_h = \begin{cases} \operatorname{sgn}(p_s - p_h) C_d A_{sa}(s_s) \sqrt{\frac{2}{\rho}} \sqrt{|p_s - p_h|}, & \text{if } s_s < 0 \\ \operatorname{sgn}(p_t - p_h) C_d A_{ta}(s_s) \sqrt{\frac{2}{\rho}} \sqrt{|p_h - p_t|}, & \text{if } s_s \geq 0 \end{cases} \tag{3.23a}$$

$$q_b = \begin{cases} \operatorname{sgn}(p_s - p_b) C_d A_{sb}(s_s) \sqrt{\frac{2}{\rho}} \sqrt{|p_s - p_b|}, & \text{if } s_s \geq 0 \\ \operatorname{sgn}(p_t - p_b) C_d A_{tb}(s_s) \sqrt{\frac{2}{\rho}} \sqrt{|p_b - p_t|}, & \text{if } s_s < 0 \end{cases} \tag{3.23b}$$

where $A_{sa}(s_s), A_{sb}(s_s), A_{tb}(s_s), A_{ta}(s_s)$ denote nonlinear orifice areas as functions of the spool displacement s_s and

$$\operatorname{sgn}(x) = \begin{cases} 1 & \text{for } x > 0 \\ 0 & \text{for } x = 0 \\ -1 & \text{for } x < 0. \end{cases} \tag{3.24}$$

Additionally, the main valve is equipped with a pressure compensator. It continuously adjusts the flow through the spool in response to the instantaneous value of the load signal, ensuring a constant pressure drop Δp_c between the loaded port and the supply port s [24]. Here, Δp_c is a factory-set value. To model the pressure-compensated valve, the equations in (3.23) are modified as follows:

$$q_h = \begin{cases} C_d A_{sa}(s_s) \sqrt{\frac{2}{\rho}} \sqrt{\Delta p_c}, & \text{if } s_s < 0, \\ \operatorname{sgn}(p_t - p_h) C_d A_{ta}(s_s) \sqrt{\frac{2}{\rho}} \sqrt{|p_h - p_t|}, & \text{if } s_s \geq 0, \end{cases} \tag{3.25a}$$

$$q_b = \begin{cases} C_d A_{sb}(s_s) \sqrt{\frac{2}{\rho}} \sqrt{\Delta p_c}, & \text{if } s_s \geq 0, \\ \operatorname{sgn}(p_t - p_b) C_d A_{tb}(s_s) \sqrt{\frac{2}{\rho}} \sqrt{|p_b - p_t|}, & \text{if } s_s < 0. \end{cases} \tag{3.25b}$$

Die approbierte gedruckte Originalversion dieser Diplomarbeit ist an der TU Wien Bibliothek verfügbar
The approved original version of this thesis is available in print at TU Wien Bibliothek.
TU Bibliothek Your knowledge hub WIEN

3.2.4 Pilot Valves

Deriving mathematical model from first principles requires the knowledge of the design, geometry and internal parameters of the pilot valves. Except of the circuit symbol, no further information about the pilot valves is provided by the manufacturer. This circumstance makes it challenging to construct a precise analytical mathematical model that represents the dynamic behavior of the pilot valves. Instead, identification techniques can be applied to create data-driven representation of the pilot valves by fitting a model directly to the input-output data.

The subscripts + and − are used to distinguish between the two pilot valves. However, since both pilot valves are of the same type and model, the subscripts will be omitted in the following discussion and the identified model will apply to both pilot valves. The pilot valves under study are proportional pressure control valves, driven by pulse-width modulated (PWM) voltage signal u with frequency of 100 Hz. The input PWM voltage generates an electrical current in the solenoid i, which is directly proportional to the pilot control pressure p. The pilot valves are designed to be controlled by a PWM current driver, therefore the electrical current i is assumed to be the input to the system. The output of the system is the pilot control pressure p which controls the spool displacement of the main valve.

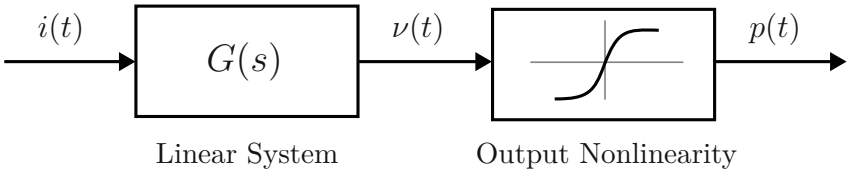

Figure 3.5: Block diagram of the mathematical model of the pilot valves.

A Wiener model [25] is used to describe the mathematical model of the pilot valves as shown in Figure 3.5. The model consists of a linear dynamic system $G(s)$ with $|G(s)| = 1$ and a static output nonlinear function $h(\cdot)$, where $\nu(t)$ represents an internal state that does not correspond to a physical quantity. The output nonlinearity $h(\cdot)$ is modeled using a second-order polynomial. The estimation of the polynomial coefficients is discussed in Chapter 5.

The linear dynamic system $G(s)$ is first identified in the discrete-time domain as $G_d(z)$ and then converted into $G(s)$ using the Tustin approximation. The transfer function $G_d(z)$ is represented via an AutoRegressive with eXogenous input (ARX) model structure due to its computational efficiency and flexibility [25, 26]. The ARX model structure is described as:

$$A\left(\delta^{-1}\right) y_k = B\left(\delta^{-1}\right) u_{k-d} + e_k, \tag{3.26}$$

where $A(\delta^{-1})$ and $B(\delta^{-1})$ are polynomials in the shift operator δ^{-1}, defined as [27, 28]

$$\delta^{-1} u_k = u_{k-1}. \tag{3.27}$$

Specifically,

$$A\left(\delta^{-1}\right) = 1 + a_1\delta^{-1} + \ldots + a_n\delta^{-n}, \tag{3.28a}$$

Die approbierte gedruckte Originalversion dieser Diplomarbeit ist an der TU Wien Bibliothek verfügbar
The approved original version of this thesis is available in print at TU Wien Bibliothek.
TU Bibliothek Your knowledge hub WIEN

$$B\left(\delta^{-1}\right) = b_0 + b_1\delta^{-1} + \ldots + a_m\delta^{-m}. \tag{3.28b}$$

y_k, u_k are the output and the input at time k, d is the input delay and e_k represents the noise. The orders (n, m) of the polynomials A and B determine the model's dynamics and are typically chosen based on the system's response characteristics. Different configurations of (m, n, d) were tested, but the best accuracy was achieved with $m = 1, n = 1, d = 0$, which corresponds to the discrete-time ARX model

$$(1 + a_1^d\delta^{-1})y_k = (b_0^d + b_1^d\delta^{-1})u_k + e_k, \tag{3.29}$$

and the discrete-time transfer function

$$G_d(z) = \frac{b_0^d z + b_1^d}{z + a_1^d}. \tag{3.30}$$

The discrete-time transfer function $G_d(z)$ can be converted into continuous-time transfer function $G(s)$ using the Tustin approximation [29, 30]:

$$G(s) = G_d(z'), \quad z' = \frac{1 + sT_s/2}{1 - sT_s/2}, \tag{3.31}$$

with sampling period T_s, which leads to

$$G(s) = \frac{b_0^c s + b_1^c}{s + a_1^c}. \tag{3.32}$$

The continuous-time transfer function can be further converted into a state-space model

$$\dot{\lambda}(t) = a_1^s\lambda(t) + i(t), \tag{3.33a}$$

$$\nu(t) = b_0^s\lambda(t) + b_1^s i(t), \tag{3.33b}$$

with the internal state $\lambda(t)$, input $i(t)$ and output $\nu(t)$. The mathematical model of the pilot valves is finally described by the following set of equations:

$$\dot{\lambda}_+(t) = a_1^s\lambda_+(t) + i_+(t), \tag{3.34a}$$

$$\nu_+(t) = b_0^s\lambda_+(t) + b_1^s i_+(t), \tag{3.34b}$$

$$p_+(t) = h(\nu_+(t)), \tag{3.34c}$$

$$\dot{\lambda}_-(t) = a_1^s\lambda_-(t) + i_-(t), \tag{3.34d}$$

$$\nu_-(t) = b_0^s\lambda_-(t) + b_1^s i_-(t), \tag{3.34e}$$

$$p_-(t) = h(\nu_-(t)). \tag{3.34f}$$

The estimation of the unknown parameters of the model will be discussed in Chapter 5.

Die approbierte gedruckte Originalversion dieser Diplomarbeit ist an der TU Wien Bibliothek verfügbar
The approved original version of this thesis is available in print at TU Wien Bibliothek.
TU Bibliothek Your knowledge hub WIEN

4 Measurements

In this work, the measurements are divided into two stages with the aim of identifying the unknown parameters of the model and verifying the mathematical model of the system. In the first stage, the measurements are conducted specifically for the system identification of the pilot valves. In the second stage, the cylinder chamber pressures, boom position, and velocity are measured to estimate the unknown parameters of the hydraulic system and validate the mathematical model of the entire system. The following sections provide detailed description of both measurement stages, including their corresponding physical setups.

4.1 First Measurement Campaign

Figure 4.1 shows a schematic of the pilot valve including measurable signals. The pilot valve, denoted with the subscript $+$ is used for illustration and explanation purposes. However, since the pilot valves are of the same type and model, everything discussed in this section also applies to the pilot valve denoted with the subscript $-$. A pressure transducer is used to measure the pilot control pressure and to convert the pressure into corresponding analog voltage signal. In total, the measurable variables include:

- Input PWM voltage u_+
- Current i_+ in the solenoid
- Pilot control pressure p_+

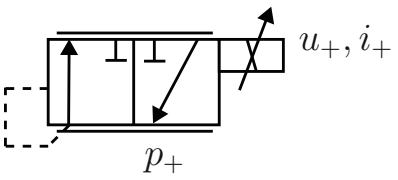

Figure 4.1: Schematic of the pilot valve including the measurable signals

The physical setup prepared by *AIT* for the first measurement stage is depicted in Figure 4.2. A *Tektronix MSO46* oscilloscope is employed to measure pilot valve signals and store them on a USB flash drive for post-processing. The signals are sampled at a rate of $f_s = 6.25\,\text{kHz}$, corresponding to a sampling period of $T_s = 0.16\,\text{ms}$. During the measurements, only the inner boom cylinder is controlled via the joystick while the other hydraulic cylinders remain stationary. The joystick is operated to generate signals that sweep through a wide range of frequencies, ensuring that the system's response to

Die approbierte gedruckte Originalversion dieser Diplomarbeit ist an der TU Wien Bibliothek verfügbar
The approved original version of this thesis is available in print at TU Wien Bibliothek.

various frequencies is captured. An example of the obtained signals is shown in Figure 4.3. As depicted in the figure, the frequency of the signal increases with time, allowing the system to be excited across a broad frequency spectrum with just one signal and providing comprehensive frequency response information. These signals are used to identify a linear dynamic model of the pilot valves. Additionally, static and ramp signals are measured to reconstruct a static output nonlinear function in the Wiener model. Finally, general-shaped signals are measured for the analysis and validation of the identified model. In total, eleven trajectories are generated and measured, including signals sweeping through a wide range of frequencies, ramp, static, and general-shaped signals. To verify the equivalence of both pilot valves, their signals are measured and compared.

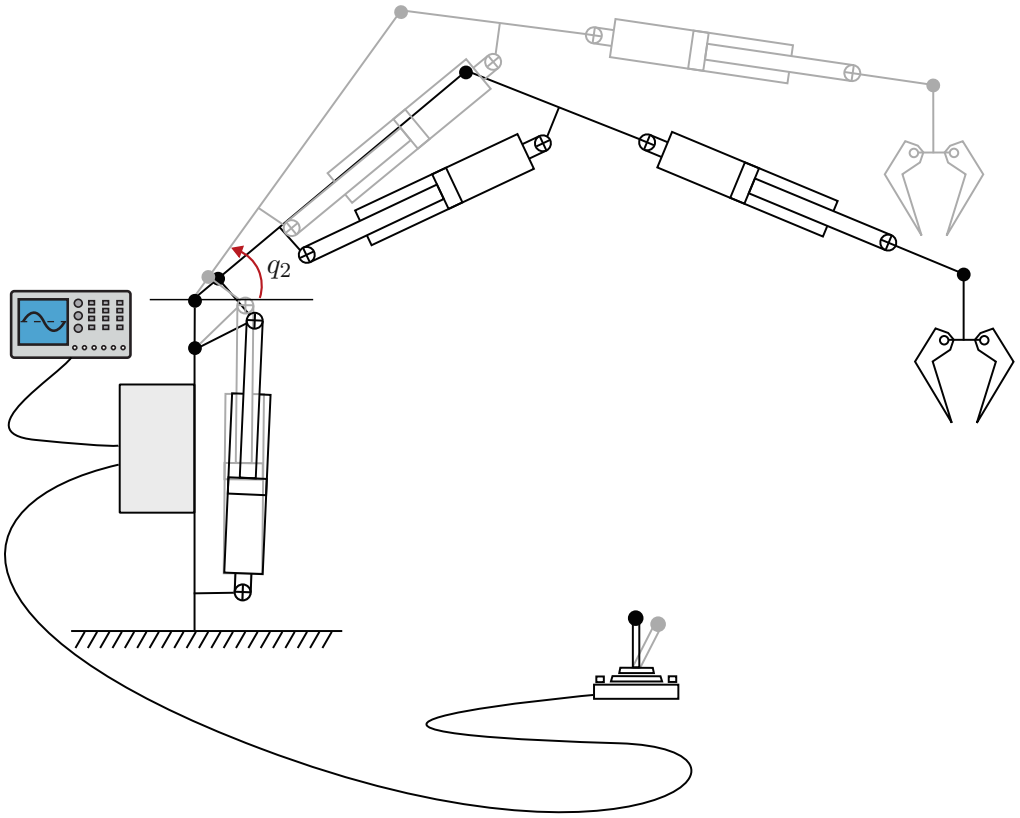

Figure 4.2: The physical setup during the first measurement stage. The inner boom cylinder is controlled via the joystick while the other hydraulic cylinders remain stationary.

Die approbierte gedruckte Originalversion dieser Diplomarbeit ist an der TU Wien Bibliothek verfügbar
The approved original version of this thesis is available in print at TU Wien Bibliothek.
TU Bibliothek Your knowledge hub WIEN

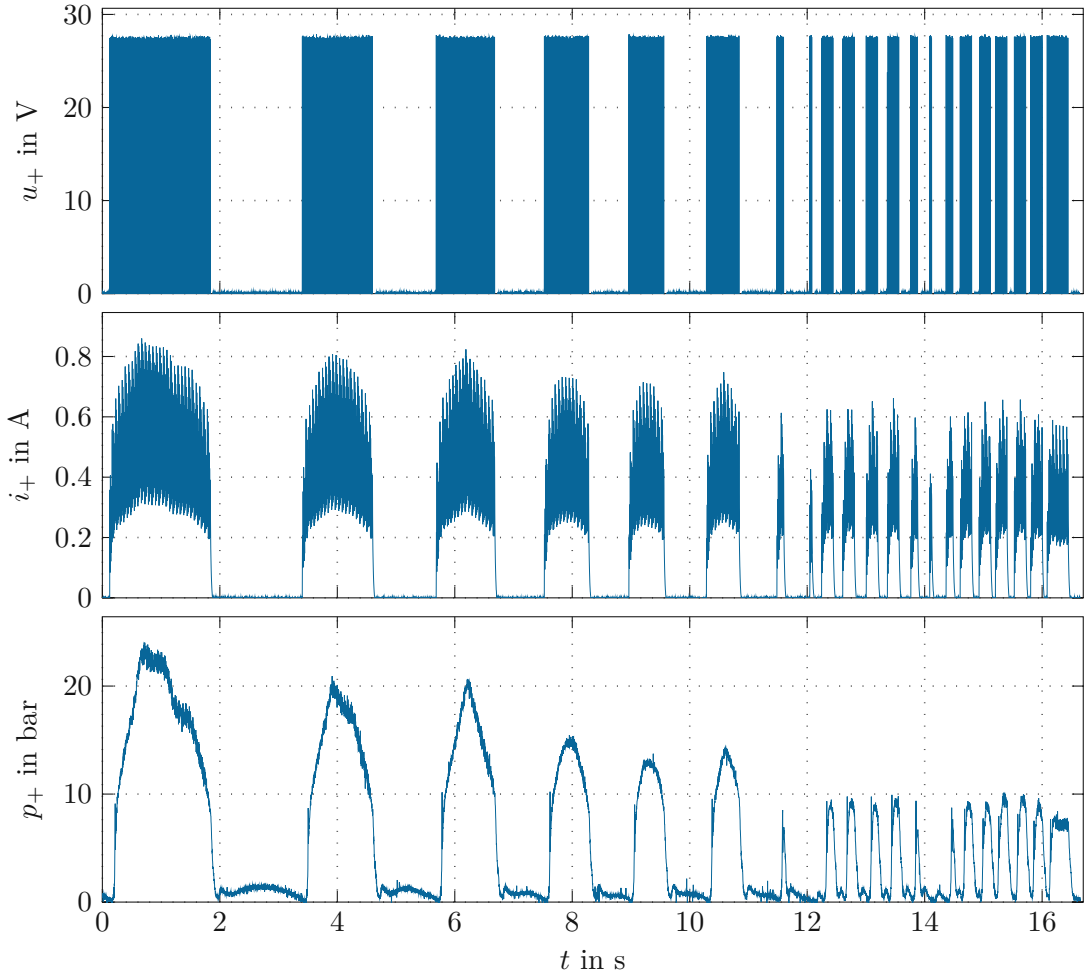

Figure 4.3: Example of measured signals during the first stage by manually controlling the crane with the joystick. The frequency of the signal increases with time, allowing the system to be excited across a broad frequency spectrum with just one signal.

4.2 Second Measurement Campaign

The physical setup prepared by *AIT* for the second measurement stage closely resembles the setup from the first measurement stage: the inner boom cylinder is controlled via the joystick while the other hydraulic cylinders remain stationary. However, unlike in the first measurement stage, the sensors are now connected to the system's CAN bus, allowing sensor signals to be directly read and stored on a USB flash drive without the need for an oscilloscope. The sensor signals are sampled at a rate of $f_s = 100\,\text{Hz}$, corresponding to a sampling period of $T_s = 10\,\text{ms}$. Figure 4.4 presents a schematic of the inner boom, including the measurable variables. Installed sensors allow to measure:

- Angle of the inner boom q_2

Die approbierte gedruckte Originalversion dieser Diplomarbeit ist an der TU Wien Bibliothek verfügbar
The approved original version of this thesis is available in print at TU Wien Bibliothek.

- Angular velocity of the inner boom $\dot{q}_2$
- Chamber pressures in the cylinder p_b
- Pressure in the hose p_h
- Currents i_+, i_- in the solenoids of the pilot valves

Chamber pressures are obtained through pressure transducers, while angular displacement and velocity are measured using an Inertial Measurement Unit (IMU) sensor mounted on the inner boom. It is important to note that, due to the integration of the hose burst valve into the hydraulic cylinder, the true chamber pressure p_a on the cap side is not directly measurable. Instead, the pressure in the hose after the hose burst valve p_h is recorded. Given the known pressure-flow characteristics of the hose burst valve, the chamber pressure p_a can be estimated from p_h in the case of slowly-varying and static signals, as will be demonstrated in Chapter 5.

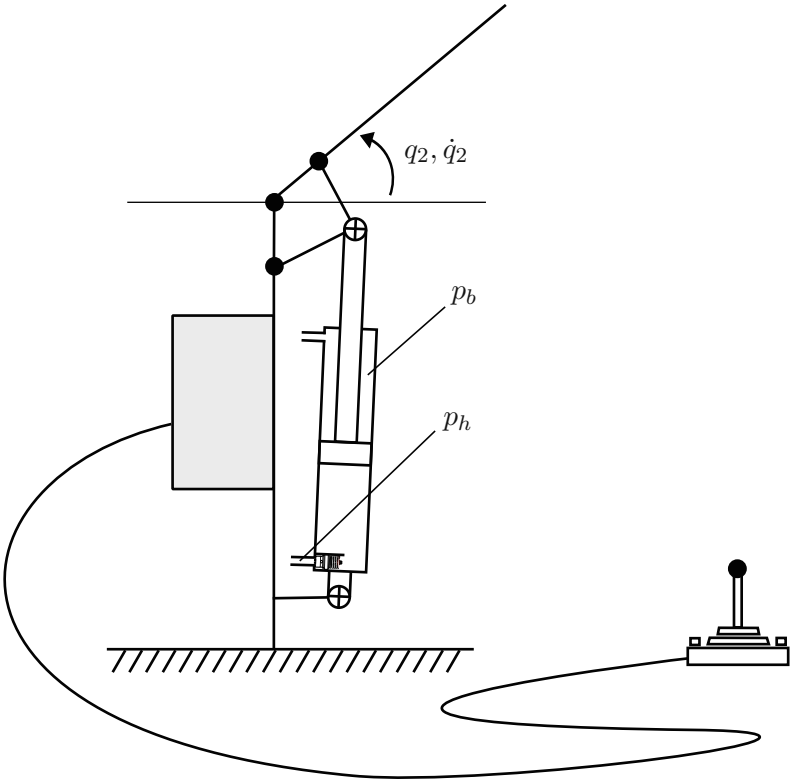

Figure 4.4: Schematic illustration of the inner boom including measurable variables during the second measurement phase.

During the measurement phase, forty-one trajectories are collected. These include static and slowly varying trajectories for model parameter identification, as well as fast-varying trajectories for model analysis and validation. To evaluate the model's performance under diverse load conditions, some trajectories are captured with a gripped wood log and with

Die approbierte gedruckte Originalversion dieser Diplomarbeit ist an der TU Wien Bibliothek verfügbar
The approved original version of this thesis is available in print at TU Wien Bibliothek.

extended telescopic and outer boom cylinders. Figure 4.5 illustrates an example of a measured trajectory during the second measurement phase. The inner boom exhibits a sinusoidal pattern, with an amplitude of approximately 0.5 rad and a period of 20 s, resulting from the alternating activation of the pilot valves during joystick control.

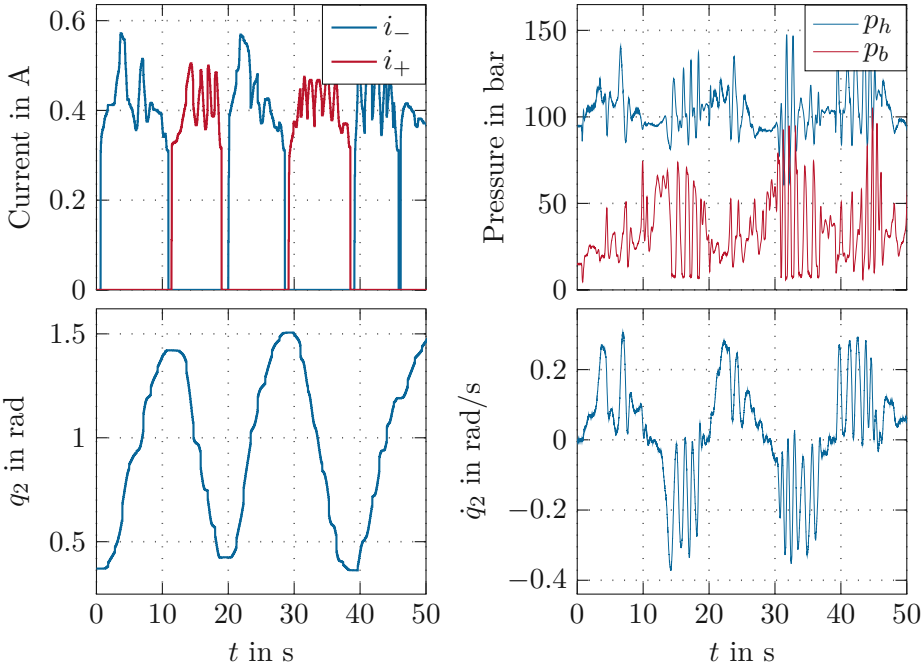

Figure 4.5: Example of measured trajectory during the second measurement phase by manually controlling the crane with the joystick.

Die approbierte gedruckte Originalversion dieser Diplomarbeit ist an der TU Wien Bibliothek verfügbar
The approved original version of this thesis is available in print at TU Wien Bibliothek.

5 System Identification

This chapter focuses on the parameter estimation and system identification of the hydraulic components. Section 5.1 describes system identification of the pilot valves based on the measured data. Section 5.2 covers parameter estimation of the main valve and the modeling of the orifice areas, using a P-Spline approach to fit the nonlinear orifice areas to the measurements. Section 5.3 discusses the modeling of the hose burst valve and parameter estimation of the friction force in the cylinder based on the measurements. By combining the mathematical models of the hydraulic components, the full model is constructed and validated in MATLAB/SIMULINK. Finally, the full model is simplified to a reduced-order model for controller design.

5.1 Pilot Valves

The subscripts $+$ and $-$ are used to distinguish between the two pilot valves. However, since both pilot valves are of the same type and model, the subscripts will be omitted in the following discussion and the identified model will apply to both pilot valves. The collected measurements of both variables $i(t), p(t)$ allow the use of system identification methods to estimate the unknown parameters.

The output nonlinearity and the linear system are estimated separately based on the measurements. Since the pilot valves are driven by PWM voltage, the measured current is a high-amplitude, periodic signal. To obtain average current, the current is filtered using the moving average algorithm [29] with a window size of $N_w = 64$ sample points, which corresponds to the period of the PWM voltage. Figure 5.1 shows the measured solenoid current and the corresponding filtered current. The same filtering algorithm is applied to the measured pilot control pressure p to compute average pressure $\bar{p}(t)$.

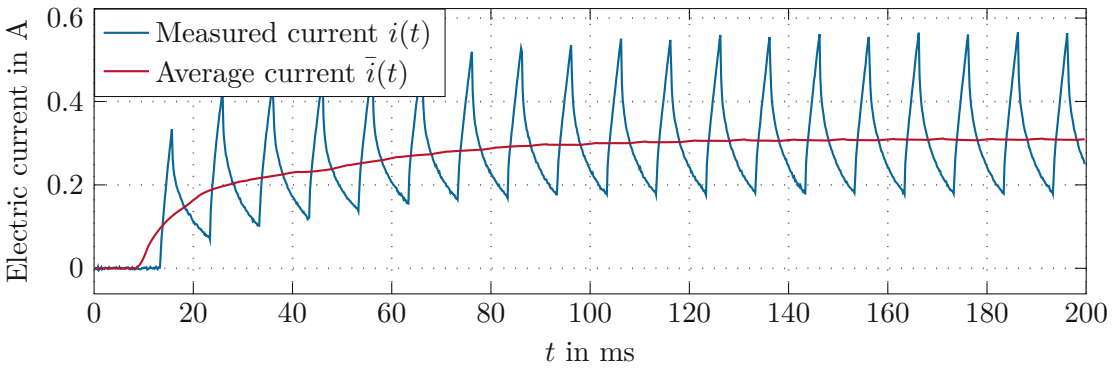

Figure 5.1: Measured solenoid current and its average value. The current is averaged using the moving average algorithm.

Die approbierte gedruckte Originalversion dieser Diplomarbeit ist an der TU Wien Bibliothek verfügbar
The approved original version of this thesis is available in print at TU Wien Bibliothek.
TU Bibliothek Your knowledge hub WIEN

The static output nonlinearity $h(\cdot)$ is reconstructed based on the stationary points of $\bar{p}(t)$ and $\bar{i}(t)$. The stationary points are defined as follows

$$\left\{ \left(\bar{i}(t), \bar{p}(t) \right) \;\middle|\; |\dot{\bar{p}}(t)| < p_{th}, |\dot{\bar{i}}(t)| < i_{th} \right\}, \tag{5.1}$$

where p_{th} and i_{th} denote constant threshold values. The time derivative of the current and the pressure signals is estimated using a Savitzky–Golay filter of polynomial order 3. Implementation of the Savitzky-Golay filter is provided by *AIT* in form of a MATLAB function. The stationary points are then collected from all experiments using the following threshold values: $p_{th} = 1\,\text{bar/s}$ and $i_{th} = 0.5\,\text{A/s}$. Figure 5.2 shows a representative example of stationary values obtained from the measured signals.

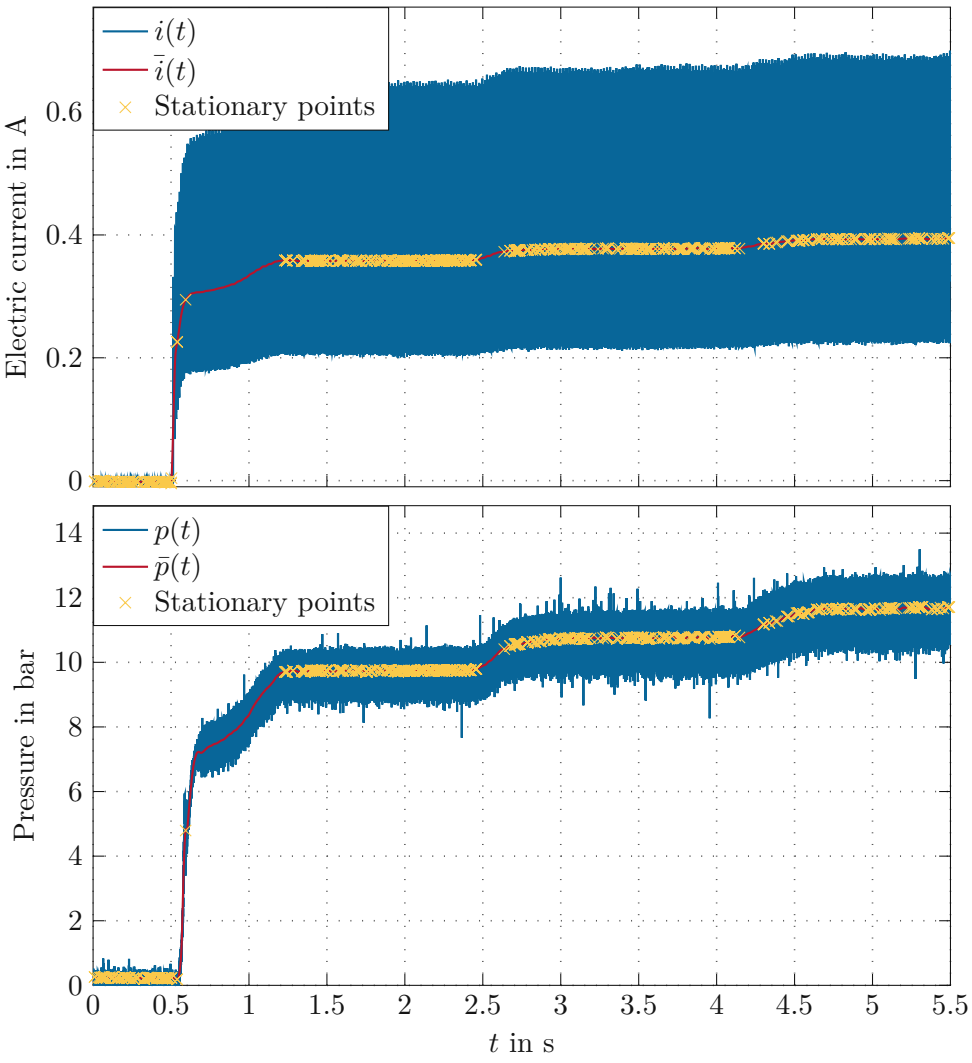

Figure 5.2: Measured solenoid current $i(t)$, its average value $\bar{i}(t)$ and stationary points calculated based on the time derivative of $\bar{p}(t), \bar{i}(t)$.

Die approbierte gedruckte Originalversion dieser Diplomarbeit ist an der TU Wien Bibliothek verfügbar
The approved original version of this thesis is available in print at TU Wien Bibliothek.
TU Bibliothek Your knowledge hub WIEN

A second-order polynomial is fitted to the estimated stationary points to derive a closed-form expression for the static output nonlinearity $h(\cdot)$. The polynomial's coefficients are determined by minimizing the squared error between the measured stationary points and the polynomial's predictions, resulting in

$$h(x) = 76.1x^2 - 0.58x + 0.247. \tag{5.2}$$

The fitted polynomial and stationary values collected from all experiments are depicted in Figure 5.3. While controlling the crane with the joystick, the minimum and maximum observed stationary values of the solenoid current are 0.3 A and 0.55 A, respectively, as can be seen from the figure.

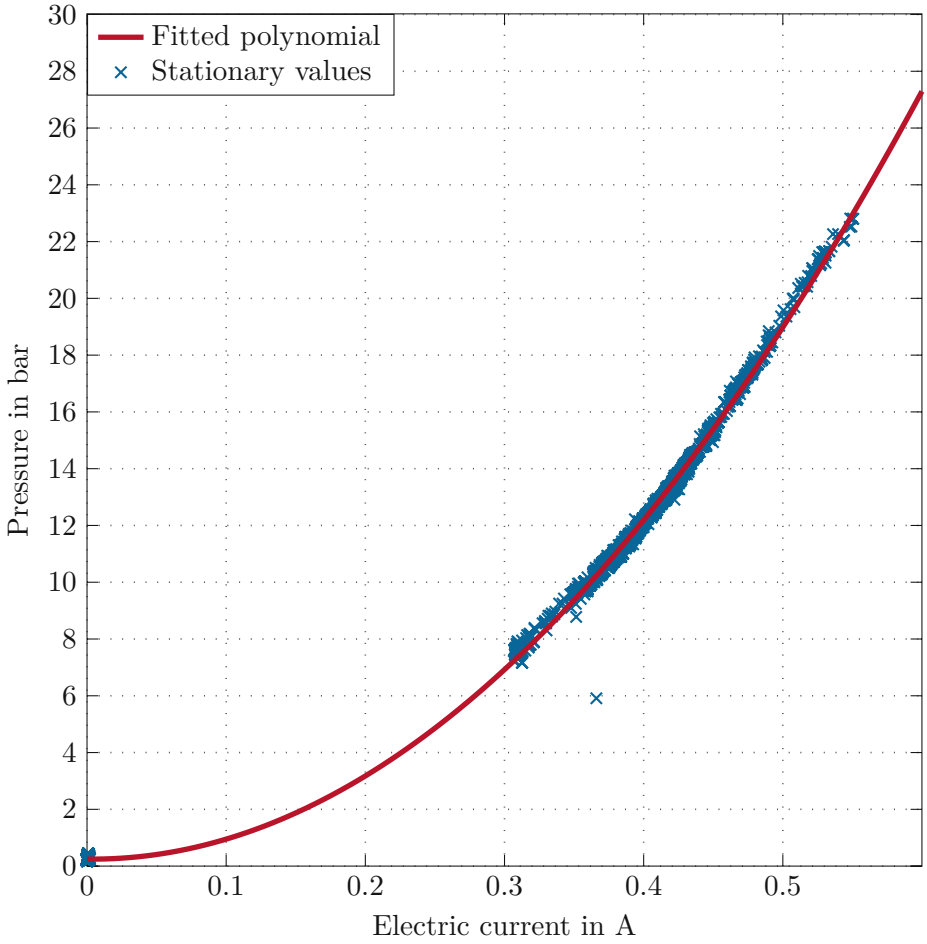

Figure 5.3: The static output nonlinearity $h(\cdot)$ is modeled by fitting a second-order polynomial to the stationary values of $\bar{i}$ and $\bar{p}$ collected from all experiments.

The Least Squares Method (LSM) is one of the most commonly used approaches in the parametric identification due to its simplicity, efficiency, and robustness [25]. The estimation of the model parameters

$$\mathbf{p} = \begin{bmatrix} a_1 & \dots & a_n & b_0 & \dots & b_m \end{bmatrix}^{\mathrm{T}}, \tag{5.3}$$

Die approbierte gedruckte Originalversion dieser Diplomarbeit ist an der TU Wien Bibliothek verfügbar
The approved original version of this thesis is available in print at TU Wien Bibliothek.

of an ARX model defined in (3.26) is performed by minimizing the sum of the squared errors between the predicted and actual outputs [25, 27]:

$$\hat{\mathbf{p}} = \underset{\mathbf{p}}{\operatorname{argmin}} \|\mathbf{e}\|^2 = \underset{\mathbf{p}}{\operatorname{argmin}} \|\mathbf{y} - \mathbf{S}\mathbf{p}\|_2^2 = \left(\mathbf{S}^{\mathrm{T}}\mathbf{S}\right)^{-1}\mathbf{S}^{\mathrm{T}}\mathbf{y}, \tag{5.4}$$

with

$$\mathbf{s}_k^{\mathrm{T}} = \begin{bmatrix} -y_{k-1} & \dots & -y_{k-n} & u_{k-d} & \dots & u_{k-d-m} \end{bmatrix}, \tag{5.5a}$$

$$\mathbf{S} = \begin{bmatrix} \mathbf{s}_1^{\mathrm{T}} \\ \vdots \\ \mathbf{s}_N^{\mathrm{T}} \end{bmatrix}, \qquad \mathbf{y} = \begin{bmatrix} y_1 & \dots & y_N \end{bmatrix}^{\mathrm{T}}. \tag{5.5b}$$

To estimate the unknown coefficients of the pilot valve's transfer function (3.30), the measured pressure values p_k are first mapped to ν_k by inverting the output nonlinearity $h(\cdot)$

$$\nu_k = h^{-1}(p_k), \tag{5.6}$$

The measured solenoid current i_k is the input to the model, and ν_k is the corresponding output. The chirp signal from Figure 4.3 with 104062 data points serves as the training data. The model parameters are computed in MATLAB using the *arx* command from the *System Identification Toolbox*. The optimization process resulted in the following estimated model parameters:

$$\mathbf{p}^d = \begin{bmatrix} a_1^d & b_0^d & b_1^d \end{bmatrix}^{\mathrm{T}} = \begin{bmatrix} -0.996 & -0.0269 & 0.031 \end{bmatrix}^{\mathrm{T}} \tag{5.7a}$$

$$\mathbf{p}^c = \begin{bmatrix} a_1^c & b_0^c & b_1^c \end{bmatrix}^{\mathrm{T}} = \begin{bmatrix} 19.67 & -0.0285 & 19.67 \end{bmatrix}^{\mathrm{T}} \tag{5.7b}$$

$$\mathbf{p}^s = \begin{bmatrix} a_1^s & b_0^s & b_1^s \end{bmatrix}^{\mathrm{T}} = \begin{bmatrix} -19.67 & 20.23 & -0.0285 \end{bmatrix}^{\mathrm{T}}. \tag{5.7c}$$

The full pilot valve model, i.e. the combination of the continuous-time transfer function $G(s)$ and the static output nonlinearity $h(\cdot)$ is subsequently tested on the validation dataset and the simulation results are compared against the measurements. The linear dynamic system $G(s)$ is simulated in MATLAB using the *lsim* command from the *Control System Toolbox*. The measured solenoid current $i(t)$ from the validation dataset serves as the input and the predicted pilot control pressure is compared against the measured pressure. Figure 5.4 illustrates the model's accuracy by comparing its predictions to the measured data. As shown in the figure, the model accurately represents the system across its entire operational range, effectively capturing both the dynamic and steady-state behavior of the system.

Die approbierte gedruckte Originalversion dieser Diplomarbeit ist an der TU Wien Bibliothek verfügbar
The approved original version of this thesis is available in print at TU Wien Bibliothek.
TU Bibliothek Your knowledge hub WIEN

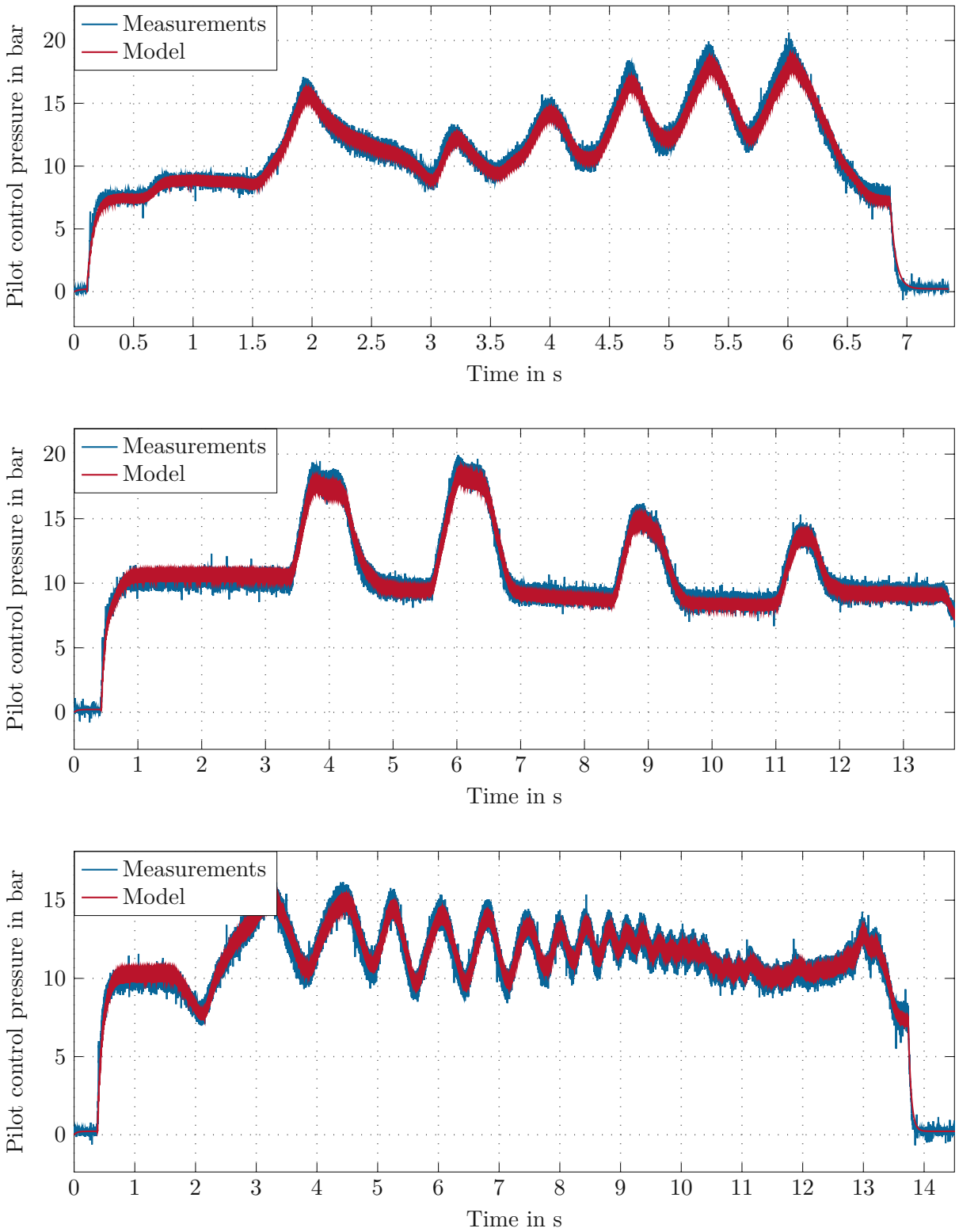

Figure 5.4: Comparison between the simulated outputs of the identified pilot valve model and the actual measurements from the validation dataset.

Die approbierte gedruckte Originalversion dieser Diplomarbeit ist an der TU Wien Bibliothek verfügbar
The approved original version of this thesis is available in print at TU Wien Bibliothek.

5.2 Main Valve

Due to the inaccessibility of the spool displacement s_s for direct measurement, precise estimation of the main valve parameters is not feasible. Therefore, an approximate estimation is employed in this work. Geometric parameters of the valve such as the volume V_s and the cross-sectional area A_s of the spool are estimated based on the dimensional drawings from the manufacture's catalogue [17]. Given the known volume of the spool, the spool mass can be computed as product of the density of iron ρ_i and the spool volume

$$m_s = V_s \rho_i. \tag{5.8}$$

The maximum and minimum spool displacement s_s^{max}, s_s^{min} are determined based on the information from the manufacture's catalogue [17]. The spring coefficient k of the valve is determined such that, when the maximum pilot control pressure p_+^{max} is applied, the valve is fully open with $s_s = s_s^{max}$. In the stationary state the equation of motion of the spool is given by

$$k s_s^{max} = p_+^{max} A_s, \tag{5.9}$$

from which the spring coefficient can be calculated as

$$k = \frac{p_+^{max} A_s}{s_s^{max}}. \tag{5.10}$$

By combining (3.21) and (3.22), the transfer function of the main valve is defined as

$$G_s(s) = \frac{1}{m_s s^2 + d_v s + k} = \frac{V_s}{(sT_s)^2 + 2\xi_s (sT_s) + 1}, \tag{5.11a}$$

where

$$T_s = \sqrt{\frac{m_s}{k}}, \quad \xi_s = \frac{d_v}{2\sqrt{k m_s}}, \quad V_s = \frac{1}{k}. \tag{5.11b}$$

The friction force coefficients are selected to match the step response and friction force characteristics typical for valves of this type [19, 31]:

$$\xi_s = 0.5 \tag{5.12a}$$
$$\sigma_s = 0.01\,\mathrm{m/s} \tag{5.12b}$$
$$d_v = 2\xi_s \sqrt{k m_s} = 160\,\mathrm{N\,s/m} \tag{5.12c}$$
$$f_c = 75\,\mathrm{N}. \tag{5.12d}$$

The total friction force

$$f_f = d_v w_s + f_c \tanh\left(\frac{w_s}{\sigma_s}\right) \tag{5.13}$$

with the estimated parameters and the step response of the spool are shown in Figure 5.5 and Figure 5.6, respectively.

Die approbierte gedruckte Originalversion dieser Diplomarbeit ist an der TU Wien Bibliothek verfügbar
The approved original version of this thesis is available in print at TU Wien Bibliothek.

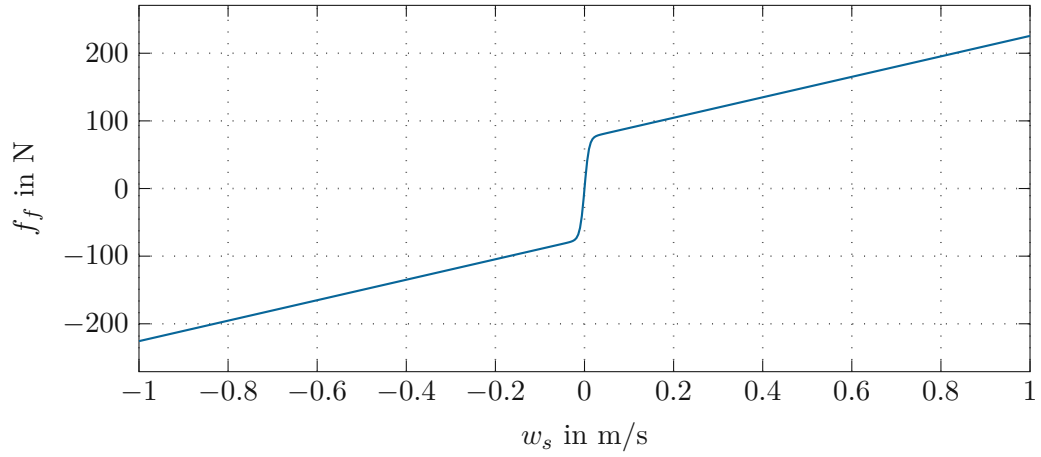

Figure 5.5: The friction force with the estimated parameters as function of the spool velocity according to (5.13).

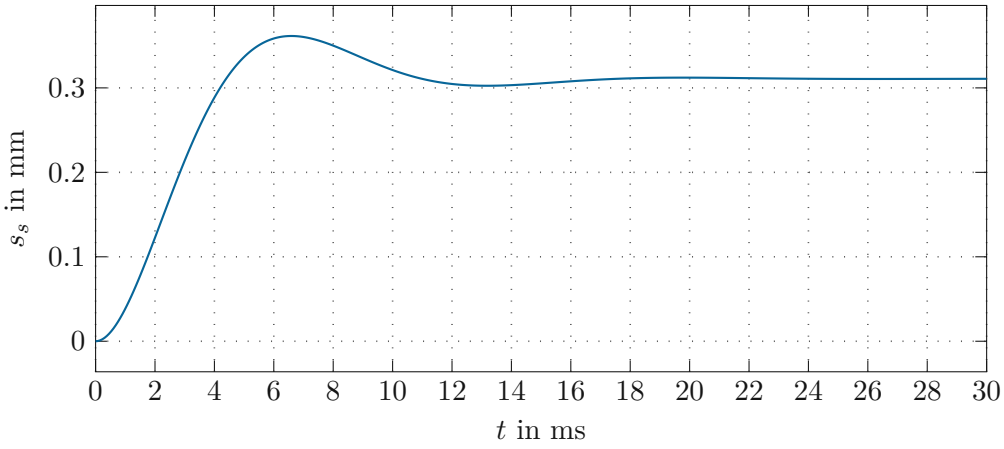

Figure 5.6: The step response of the main valve by actuating the spool with a pilot control pressure of 1 bar.

The orifice areas of the main valve are estimated based on the measurement data. Assuming a steady-state situation, i.e.

$$\dot{p}_a = 0, \quad \dot{p}_b = 0, \quad \dot{p}_{o,1} = 0, \quad \dot{p}_{o,2} = 0, \tag{5.14}$$

(3.11) and (3.19) simplify to

$$q_a = q_h = w_p A_a, \quad q_b = -w_p A_b, \tag{5.15}$$

with

$$q_h = \begin{cases} C_d A_{sa}(s_s)\sqrt{\frac{2}{\rho}}\sqrt{\Delta p_c}, & \text{if } s_s < 0, \\ \operatorname{sgn}(p_t - p_h) C_d A_{ta}(s_s)\sqrt{\frac{2}{\rho}}\sqrt{|p_h - p_t|}, & \text{if } s_s \geq 0, \end{cases} \tag{5.16a}$$

Die approbierte gedruckte Originalversion dieser Diplomarbeit ist an der TU Wien Bibliothek verfügbar
The approved original version of this thesis is available in print at TU Wien Bibliothek.
TU Bibliothek Your knowledge hub WIEN

$$q_b = \begin{cases} C_d A_{sb}(s_s)\sqrt{\frac{2}{\rho}}\sqrt{\Delta p_c}, & \text{if } s_s \geq 0, \\ \operatorname{sgn}(p_t - p_b) C_d A_{tb}(s_s)\sqrt{\frac{2}{\rho}}\sqrt{|p_b - p_t|}, & \text{if } s_s < 0. \end{cases} \tag{5.16b}$$

By combining (5.15) and (5.16) the orifice areas can be calculated as

$$A_a^{mv}(s_s) = \begin{cases} A_{sa}(s_s), & \text{if } s_s < 0, \\ A_{ta}(s_s), & \text{otherwise}, \end{cases} \tag{5.17a}$$

$$A_b^{mv}(s_s) = \begin{cases} A_{sb}(s_s), & \text{if } s_s \geq 0, \\ A_{tb}(s_s), & \text{otherwise}, \end{cases} \tag{5.17b}$$

$$A_{sa}(s_s) = \frac{w_p A_a}{C_d\sqrt{\frac{2}{\rho}}\sqrt{\Delta p_c}}, \tag{5.17c}$$

$$A_{ta}(s_s) = \frac{w_p A_a}{\operatorname{sgn}(p_t - p_h) C_d\sqrt{\frac{2}{\rho}}\sqrt{|p_h - p_t|}}, \tag{5.17d}$$

$$A_{sb}(s_s) = \frac{-w_p A_b}{C_d\sqrt{\frac{2}{\rho}}\sqrt{\Delta p_c}}, \tag{5.17e}$$

$$A_{tb}(s_s) = \frac{-w_p A_b}{\operatorname{sgn}(p_t - p_b) C_d\sqrt{\frac{2}{\rho}}\sqrt{|p_b - p_t|}}. \tag{5.17f}$$

The variables on the right-hand side of (5.17) are measurable, making it possible to estimate the orifice areas based on the measurement data. The stationary value of the spool position s_s is estimated using (3.21)

$$s_s = \frac{(p_+ - p_-)A_s}{k}. \tag{5.18}$$

Since the pilot solenoid currents i_+, i_- are both measurable, the corresponding pilot control pressures, p_+, p_-, can be determined using the identified mathematical model of the pilot valves. This enables the estimation of the spool displacement as described in (5.18) and the reconstruction of the functions $A_{sa}(s_s)$, $A_{ta}(s_s)$, $A_{sb}(s_s)$, $A_{tb}(s_s)$.

A penalized B-Spline or P-Spline model [32, 33] is utilized to fit the nonlinear orifice areas to the measured data. A B-Spline model is expressed as a linear combination of d B-spline basis functions [33]:

$$y(x) = \sum_{i=0}^{d} B_i^l(x)\beta_i, \tag{5.19}$$

Die approbierte gedruckte Originalversion dieser Diplomarbeit ist an der TU Wien Bibliothek verfügbar
The approved original version of this thesis is available in print at TU Wien Bibliothek.
TU Bibliothek Your knowledge hub WIEN

where $B_i^l(x)$ denotes i-th basis function of order l, d number of basis functions and β_i parameters to be optimized. The basis function $B_i^l(x)$ is defined recursively and has non-zero values only within the interval $x \in [\kappa_i, \kappa_{i+1})$ [33]:

$$B_i^0(x) = \begin{cases} 1, & \text{for } \kappa_i \leq x < \kappa_{i+1}, \\ 0, & \text{otherwise}, \end{cases} \tag{5.20a}$$

$$B_i^l(x) = \frac{x - \kappa_{i-l}}{\kappa_i - \kappa_{i-l}} B_{i-1}^{l-1}(x) + \frac{\kappa_{i+1} - x}{\kappa_{i+1} - \kappa_{i+1-l}} B_i^{l-1}(x), \tag{5.20b}$$

where κ_i and κ_{i+1} refer to the nodes of the region $[\kappa_i, \kappa_{i+1}]$. To fit the model to measured data, a cost function given by

$$L(\boldsymbol{\beta}) = \|\mathbf{y} - \mathbf{B}\boldsymbol{\beta}\|_2^2, \tag{5.21}$$

is minimized with respect to spline coefficients $\boldsymbol{\beta} = \begin{bmatrix}\beta_1, \beta_2, \ldots, \beta_d\end{bmatrix}^{\mathrm{T}}$. Here, $\mathbf{y}$ denotes the measured data

$$\mathbf{y} = \begin{bmatrix} y_1 & y_2 & \ldots & y_n \end{bmatrix}^{\mathrm{T}}, \tag{5.22}$$

and $\mathbf{B}$ matrix with entries $B_{ij} = B_j^l(x_i)$. To control the smoothness of the model, the loss function (5.21) is augmented with an additional regularization term [33]

$$L_P(\boldsymbol{\beta}) = \|\mathbf{y} - \mathbf{B}\boldsymbol{\beta}\|_2^2 + \lambda \int \left(\frac{\mathrm{d}^2 y(\tilde{x})}{\mathrm{d}\tilde{x}^2} \right)^2 \mathrm{d}\tilde{x}, \tag{5.23}$$

where λ is a constant smoothing parameter that penalizes curvature in the function. Using (5.19), the loss function (5.23) reduces to

$$L_P(\boldsymbol{\beta}) = \|\mathbf{y} - \mathbf{B}\boldsymbol{\beta}\|_2^2 + \lambda \boldsymbol{\beta}^{\mathrm{T}} \boldsymbol{\Omega} \boldsymbol{\beta}, \tag{5.24}$$

where $\boldsymbol{\Omega}$ denotes matrix with entries

$$\Omega_{ij} = \int \frac{\mathrm{d}^2 B_i^l(\tilde{x})}{\mathrm{d}\tilde{x}^2} \frac{\mathrm{d}^2 B_j^l(\tilde{x})}{\mathrm{d}\tilde{x}^2} \mathrm{d}\tilde{x}. \tag{5.25}$$

The fitted P-Spline is obtained by minimizing (5.24), and can be expressed as [33]:

$$\hat{\boldsymbol{\beta}} = \underset{\boldsymbol{\beta}}{\operatorname{argmin}} \left[\|\mathbf{y} - \mathbf{B}\boldsymbol{\beta}\|_2^2 + \lambda \boldsymbol{\beta}^{\mathrm{T}} \boldsymbol{\Omega} \boldsymbol{\beta} \right] = \left(\mathbf{B}^{\mathrm{T}}\mathbf{B} + \lambda \boldsymbol{\Omega} \right)^{-1} \mathbf{B}^{\mathrm{T}} \mathbf{y}, \tag{5.26a}$$

$$\hat{y}(x) = \sum_{i=0}^{d} B_i^l(x) \hat{\beta}_i. \tag{5.26b}$$

In this work, the P-Spline optimization is conducted using the MATLAB library *CDSplines*, provided by *AIT*. Prior to model fitting, the measured data is filtered to include only stationary values, ensuring that the steady-state assumption (5.14) is satisfied. The P-Spline optimization is then performed on the normalized data:

$$\bar{A}_a^{mv} = \frac{A_a^{mv}}{A_0}, \quad \bar{A}_b^{mv} = \frac{A_b^{mv}}{A_0}, \tag{5.27a}$$

Die approbierte gedruckte Originalversion dieser Diplomarbeit ist an der TU Wien Bibliothek verfügbar
The approved original version of this thesis is available in print at TU Wien Bibliothek.
TU Bibliothek Your knowledge hub WIEN

$$\bar{s}_s = \frac{s_s}{s_s^{max}}, \tag{5.27b}$$

where both $\bar{A}_a^{mv}(\bar{s}_s)$ and $\bar{A}_b^{mv}(\bar{s}_s)$ are modeled using $d = 15$ basis functions of order $l = 3$ with equidistant nodes and $\lambda = 100$. Figure 5.7 and Figure 5.8 show the measured data and the optimized P-Spline models of $\bar{A}_a^{mv}(\bar{s}_s)$ and $\bar{A}_b^{mv}(\bar{s}_s)$, respectively.

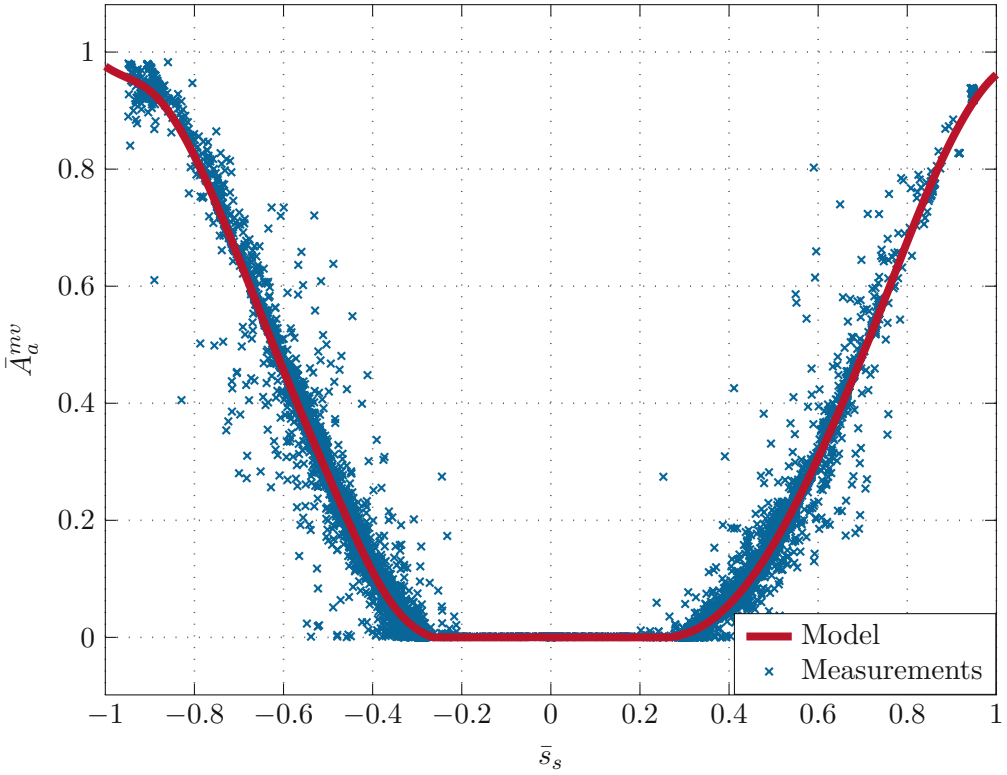

Figure 5.7: Comparison between the P-Spline model of the normalized orifice area $\bar{A}_a^{mv}$ and the measured data.

Die approbierte gedruckte Originalversion dieser Diplomarbeit ist an der TU Wien Bibliothek verfügbar
The approved original version of this thesis is available in print at TU Wien Bibliothek.
TU Bibliothek Your knowledge hub WIEN

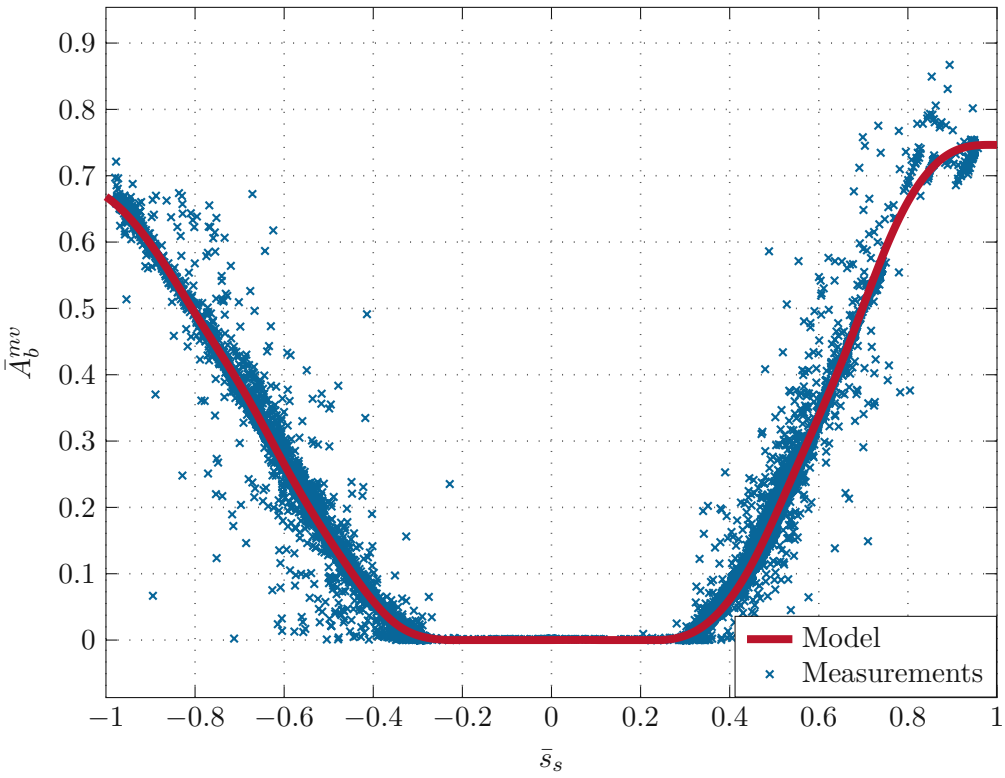

Figure 5.8: Comparison between the P-Spline model of the normalized orifice area $\bar{A}_b^{mv}$ and the measured data.

5.3 Hydraulic Cylinder

The flow through the hose burst valve q_a can be computed from the pressure drop across the valve $\Delta p_{ha} = p_h - p_a$ using the flow-pressure diagram from the manufacture's catalogue [34]. The flow-pressure curve from the datasheet is shown in Figure 5.9. Polynomial regression is utilized to fit a nonlinear model to the curve and find a closed-form expression for $q_a(\Delta p_{ha})$. To achieve this, the graph is partitioned into three regions and for each of the regions an individual polynomial is defined. The flow rate $q_a(\Delta p_{ha})$ can be expressed as

$$q_a(\Delta p_{ha}) = \begin{cases} q_{a,1}(\Delta p_{ha}) = a_{11}\Delta p_{ha} + a_{12}\sqrt{\Delta p_{ha}}, & \text{if } \Delta p_{ha} \geq 0 \\ q_{a,2}(\Delta p_{ha}) = a_{21}\Delta p_{ha} + a_{22}\Delta p_{ha}^2, & \text{if } -22\,\text{bar} \leq \Delta p_{ha} < 0 \\ q_{a,3}(\Delta p_{ha}) = a_{30} + a_{31}\Delta p_{ha}, & \text{else.} \end{cases} \tag{5.28}$$

Additionally, the functions $q_{a,2}$ and $q_{a,3}$ are required to be continuously differentiable at the node $\Delta p_{ha} = 22\,\text{bar}$ to obtain smooth transition between the regions. As depicted in Figure 5.9, the flow rate curve shows distinct behavior around the transition point $\Delta p_{ha} = 0\,\text{bar}$. As a result, it cannot be accurately modeled as differentiable at this point using polynomials while still closely approximating the datasheet values. The requirement

Die approbierte gedruckte Originalversion dieser Diplomarbeit ist an der TU Wien Bibliothek verfügbar
The approved original version of this thesis is available in print at TU Wien Bibliothek.
TU Bibliothek Your knowledge hub WIEN

for differentiability at the node $\Delta p_{ha} = 0\,\text{bar}$ is therefore omitted.

$$g_1 = \Big(q_{a,2}(\Delta p_{ha}) - q_{a,3}(\Delta p_{ha})\Big)\Big|_{\Delta p_{ha}=22\,\text{bar}} = 0 \tag{5.29a}$$

$$g_2 = \left(\frac{\mathrm{d}q_{a,2}(\Delta p_{ha})}{\mathrm{d}\Delta p_{ha}} - \frac{\mathrm{d}q_{a,3}(\Delta p_{ha})}{\mathrm{d}\Delta p_{ha}}\right)\Bigg|_{\Delta p_{ha}=22\,\text{bar}} = 0. \tag{5.29b}$$

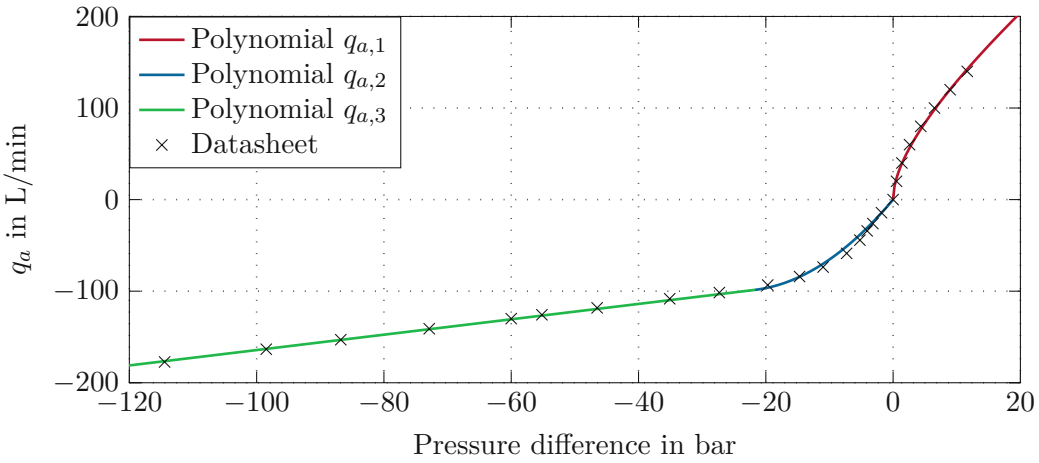

Figure 5.9: Flow-pressure graph of the hose burst valve from the manufacture's catalogue. Polynomial regression is used to fit the curve and find a closed-form expression for $q_a(\Delta p_{ha})$.

The polynomial coefficients from (5.28) can be computed by solving the following optimization problem:

$$\min_{\mathbf{a}\in\mathbb{R}^6} \quad f(\mathbf{a}) = \sum_{i=1}^{3} \|\mathbf{y}_i - \mathbf{X}_i\mathbf{a}_i\|_2, \tag{5.30a}$$

$$\begin{aligned} \text{subject to:} \quad & g_1(\mathbf{a}) = 0, \\ & g_2(\mathbf{a}) = 0, \end{aligned} \tag{5.30b}$$

where $\mathbf{a}$ denotes the polynomial coefficients

$$\mathbf{a} = \begin{bmatrix} \mathbf{a}_1 \\ \mathbf{a}_2 \\ \mathbf{a}_3 \end{bmatrix}, \quad \mathbf{a}_1 = \begin{bmatrix} a_{11} \\ a_{12} \end{bmatrix}, \quad \mathbf{a}_2 = \begin{bmatrix} a_{21} \\ a_{22} \end{bmatrix}, \quad \mathbf{a}_3 = \begin{bmatrix} a_{30} \\ a_{31} \end{bmatrix}, \tag{5.31}$$

$\mathbf{X}_i$ denotes polynomial terms evaluated at the corresponding Δp_{ha} values in the region i:

$$\mathbf{X}_1 = \begin{bmatrix} \Delta p_{1,1} & \sqrt{\Delta p_{1,1}} \\ \Delta p_{1,2} & \sqrt{\Delta p_{1,2}} \\ \vdots & \vdots \\ \Delta p_{1,n_1} & \sqrt{\Delta p_{1,n_1}} \end{bmatrix}, \mathbf{X}_2 = \begin{bmatrix} \Delta p_{2,1} & \Delta p_{2,1}^2 \\ \Delta p_{2,2} & \Delta p_{2,2}^2 \\ \vdots & \vdots \\ \Delta p_{2,n_2} & \Delta p_{2,n_2}^2 \end{bmatrix}, \mathbf{X}_3 = \begin{bmatrix} 1 & \Delta p_{3,1} \\ 1 & \Delta p_{3,2} \\ \vdots & \vdots \\ 1 & \Delta p_{3,n_3} \end{bmatrix}, \tag{5.32}$$

Die approbierte gedruckte Originalversion dieser Diplomarbeit ist an der TU Wien Bibliothek verfügbar
The approved original version of this thesis is available in print at TU Wien Bibliothek.
TU Bibliothek Your knowledge hub WIEN

and $\mathbf{y}_i \in \mathbb{R}^{n_i}$ the flow rate values from the graph in the region i. The Lagrangian function for this optimization problem is defined as

$$\mathcal{L}(\mathbf{a}, \boldsymbol{\lambda}) = f(\mathbf{a}) + \boldsymbol{\lambda}^{\mathrm{T}}\mathbf{g}(\mathbf{a}) = \sum_{i=1}^{3} \|\mathbf{y}_i - \mathbf{X}_i\mathbf{a}_i\|_2 + \boldsymbol{\lambda}^{\mathrm{T}}\mathbf{g}(\mathbf{a}), \tag{5.33}$$

with

$$\mathbf{g}^{\mathrm{T}} = \begin{bmatrix} g_1 & g_2 \end{bmatrix} \tag{5.34a}$$

$$\boldsymbol{\lambda}^{\mathrm{T}} = \begin{bmatrix} \lambda_1 & \lambda_2 \end{bmatrix}. \tag{5.34b}$$

The first-order necessary conditions for the constrained optimality can be formulated using the Lagrangian function as [35]:

$$\left(\frac{\partial \mathcal{L}}{\partial \mathbf{a}}\right)^{\mathrm{T}}(\mathbf{a}^*, \boldsymbol{\lambda}^*) = \mathbf{0} \quad \text{and} \quad \left(\frac{\partial \mathcal{L}}{\partial \boldsymbol{\lambda}}\right)^{\mathrm{T}}(\mathbf{a}^*, \boldsymbol{\lambda}^*) = \mathbf{g}^{\mathrm{T}}(\mathbf{a}^*) = \mathbf{0}. \tag{5.35}$$

The solution $(\mathbf{a}^*, \boldsymbol{\lambda}^*)$ of the optimization problem (5.30) can be found by solving the system of equations for $(\mathbf{a}^*, \boldsymbol{\lambda}^*)$. The derivatives are computed in MAPLE and the system of equations is solved using *solve* command, leading to

$$\mathbf{a}^* = \begin{bmatrix} a_{11} \\ a_{12} \\ a_{21} \\ a_{22} \\ a_{30} \\ a_{31} \end{bmatrix} = \begin{bmatrix} 3.67 \\ 29.2 \\ 8.24 \\ 0.17 \\ -80.3 \\ 0.84 \end{bmatrix}, \tag{5.36}$$

The fitted polynomials and the flow-pressure graph from the datasheet are shown in Figure 5.9.

The unknown coefficients $\tau_{C_+}, k_{v_+}, \tau_{C_-}, k_{v_-}$ in the friction force are estimated based on the performed measurements. Since the pressure in the cylinder chamber p_a is not measurable, the friction torque can't be reconstructed directly from the measurements via (3.4). The pressure in the cylinder chamber p_a is, therefore, approximated based on the pressure in the hose p_h and the flow-pressure graph of the hose burst valve. Under steady-state conditions, where the pressure change $\dot{p}_a$ is negligible, the flow rate q_a can be computed from the angular velocity $\dot{q}_2$ using (3.11):

$$q_a = w_p A_a = J(q_2)\dot{q}_2 A_a. \tag{5.37}$$

Finally, p_a can be determined from the measurable $q_2, \dot{q}_2, p_h$ using the following equation:

$$p_a = p_h - \Delta p_{ha}(q_2, \dot{q}_2), \tag{5.38}$$

with $\Delta p_{ha} = p_h - p_a$. Data points for τ_f are computed from the measured data using (3.4). The measured data is pre-filtered to include only stationary points, ensuring that steady-state conditions are met. Subsequently, the friction torque model (3.7) is fitted to the measured friction torque, whereas the unknown coefficients $\tau_{C_+}, \tau_{C_-}, k_{v_+}, k_{v_-}$ are

Die approbierte gedruckte Originalversion dieser Diplomarbeit ist an der TU Wien Bibliothek verfügbar
The approved original version of this thesis is available in print at TU Wien Bibliothek.
TU Bibliothek Your knowledge hub WIEN

identified using the Linear Least Squares method. Figure 5.10 illustrates a comparison between the friction torque predicted by the model $\tau_f(\dot{q}_2)$ and the friction torque measured experimentally. As shown in the figure, the measured friction torque exhibits asymmetric behavior and demonstrates characteristic of Coulomb and viscous friction. It's important to note that the measured torque also includes inaccuracies from the crane's hydraulic, mechanical, and load models, contributing to the observed uncertainty. The proposed mathematical model effectively captures the asymmetric friction torque, and the estimated parameters provide an average approximation of the measured torque.

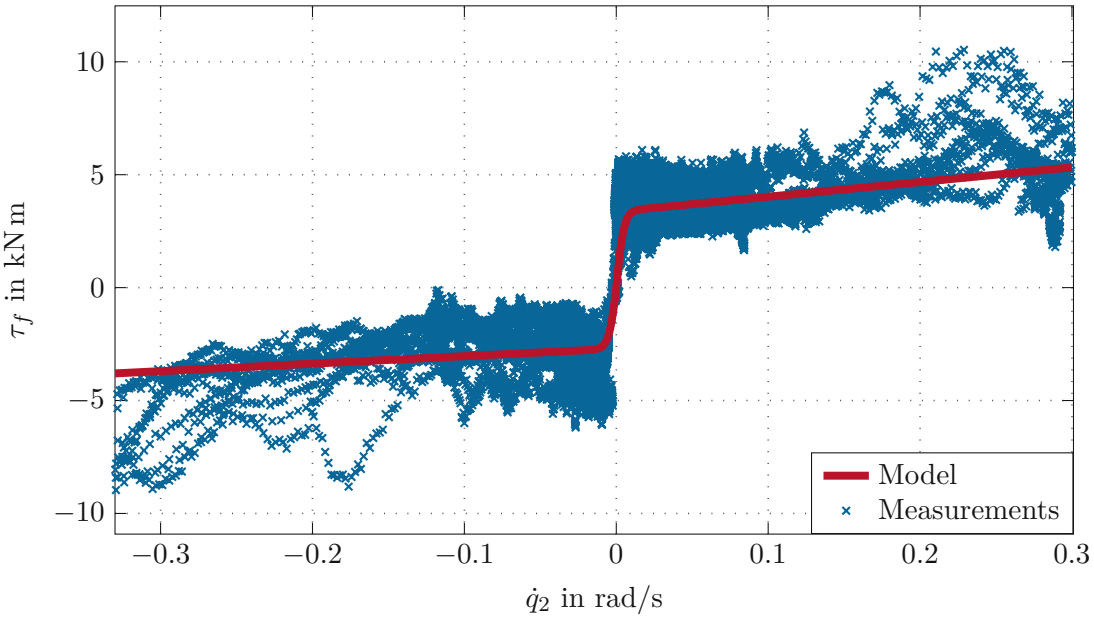

Figure 5.10: Comparison between the identified and measured friction torques.

Die approbierte gedruckte Originalversion dieser Diplomarbeit ist an der TU Wien Bibliothek verfügbar
The approved original version of this thesis is available in print at TU Wien Bibliothek.

5.4 Full Model

By combining the equations from the previous sections, the full model of the hydraulic system is constructed and shown in Figure 5.11. The mathematical model of the hydraulic system is described by the following set of equations:

$$D\ddot{q}_2 + g(q_2) = J(q_2)(p_a A_a - p_b A_b) - \tau_f(\dot{q}_2), \tag{5.39a}$$

$$\tau_f = \begin{cases} \tau_{C_+} \tanh\left(\dfrac{\dot{q}_2}{\sigma}\right) + k_{v_+}\dot{q}_2, & \text{if } \dot{q}_2 \geq 0, \\ \tau_{C_-} \tanh\left(\dfrac{\dot{q}_2}{\sigma}\right) + k_{v_-}\dot{q}_2, & \text{if } \dot{q}_2 < 0, \end{cases} \tag{5.39b}$$

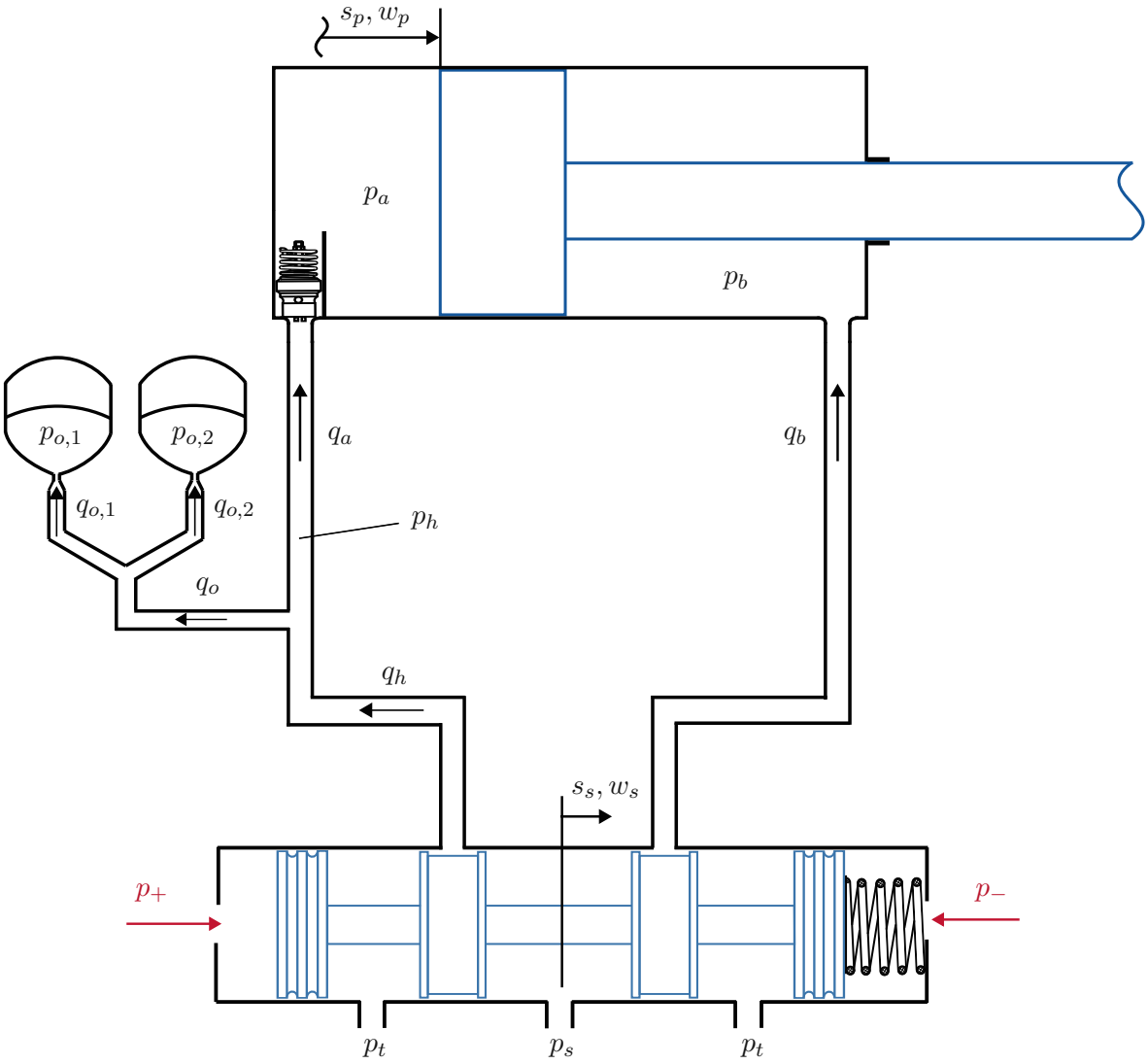

Figure 5.11: Schematic illustration of the hydraulic system of the inner boom.

Die approbierte gedruckte Originalversion dieser Diplomarbeit ist an der TU Wien Bibliothek verfügbar
The approved original version of this thesis is available in print at TU Wien Bibliothek.

$$\dot{p}_a = \frac{\beta}{V_{0,a} + s_p A_a}(q_a - w_p A_a), \tag{5.39c}$$

$$\dot{p}_b = \frac{\beta}{V_{0,b} + (l_p - s_p) A_b}(q_b + w_p A_b), \tag{5.39d}$$

$$\Delta p_{ha} = p_h - p_a, \tag{5.39e}$$

$$q_a(\Delta p_{ha}) = \begin{cases} a_{11}\Delta p_{ha} + a_{12}\sqrt{\Delta p_{ha}}, & \text{if } \Delta p_{ha} \geq 0, \\ a_{21}\Delta p_{ha} + a_{22}\Delta p_{ha}^2, & \text{if } -22\,\text{bar} \leq \Delta p_{ha} < 0\,, \\ a_{30} + a_{31}\Delta p_{ha}, & \text{otherwise,} \end{cases} \tag{5.39f}$$

$$\frac{\mathrm{d}}{\mathrm{d}t} p_{o,1} = \frac{\kappa\beta p_{o,1} q_{o,1}}{\kappa p_{o,1} V_{g0} + (\beta - \kappa p_{o,1})\left(\frac{\zeta_{0,1}}{p_{o,1}}\right)^{\frac{1}{\kappa}}}, \tag{5.39g}$$

$$\frac{\mathrm{d}}{\mathrm{d}t} p_{o,2} = \frac{\kappa\beta p_{o,2} q_{o,2}}{\kappa p_{o,2} V_{g0} + (\beta - \kappa p_{o,2})\left(\frac{\zeta_{0,2}}{p_{o,2}}\right)^{\frac{1}{\kappa}}}, \tag{5.39h}$$

$$\dot{p}_h = \frac{\beta}{V_h}(q_h - q_o - q_a), \tag{5.39i}$$

$$q_{o,1} = \begin{cases} 0, & \text{if } p_h < p_{o,1} \leq p_{g0,1}, \\ \operatorname{sign}(p_h - p_{o,1}) C_d \frac{\pi d^2}{4}\sqrt{\frac{2}{\rho}}\sqrt{|p_h - p_{o,1}|}, & \text{otherwise,} \end{cases} \tag{5.39j}$$

$$q_{o,2} = \begin{cases} 0, & \text{if } p_h < p_{o,2} \leq p_{g0,2}, \\ \operatorname{sign}(p_h - p_{o,2}) C_d \frac{\pi d^2}{4}\sqrt{\frac{2}{\rho}}\sqrt{|p_h - p_{o,2}|}, & \text{otherwise,} \end{cases} \tag{5.39k}$$

$$q_h = \begin{cases} C_d A_{sa}(s_s)\sqrt{\frac{2}{\rho}}\sqrt{\Delta p_c}, & \text{if } s_s < 0, \\ \operatorname{sgn}(p_t - p_h) C_d A_{ta}(s_s)\sqrt{\frac{2}{\rho}}\sqrt{|p_h - p_t|}, & \text{if } s_s \geq 0, \end{cases} \tag{5.39l}$$

$$q_b = \begin{cases} C_d A_{sb}(s_s)\sqrt{\frac{2}{\rho}}\sqrt{\Delta p_c}, & \text{if } s_s \geq 0, \\ \operatorname{sgn}(p_t - p_b) C_d A_{tb}(s_s)\sqrt{\frac{2}{\rho}}\sqrt{|p_b - p_t|}, & \text{if } s_s < 0, \end{cases} \tag{5.39m}$$

Die approbierte gedruckte Originalversion dieser Diplomarbeit ist an der TU Wien Bibliothek verfügbar
The approved original version of this thesis is available in print at TU Wien Bibliothek.
TU Bibliothek Your knowledge hub WIEN

$$m_s\ddot{s}_s + ks_s = (p_+ - p_-)A_s - f_f, \tag{5.39n}$$
$$f_f = d_v\dot{s}_s + f_c \tanh\frac{\dot{s}_s}{\sigma_s}, \tag{5.39o}$$
$$\dot{\lambda}_+(t) = a_1^s\lambda_+(t) + i_+(t), \tag{5.39p}$$
$$\nu_+(t) = b_0^s\lambda_+(t) + b_1^s i_+(t), \tag{5.39q}$$
$$p_+(t) = h(\nu_+(t)), \tag{5.39r}$$
$$\dot{\lambda}_-(t) = a_1^s\lambda_-(t) + i_-(t), \tag{5.39s}$$
$$\nu_-(t) = b_0^s\lambda_-(t) + b_1^s i_-(t), \tag{5.39t}$$
$$p_-(t) = h(\nu_-(t)). \tag{5.39u}$$

The full model is an 11th-order nonlinear dynamic system with the state vector defined as:

$$\mathbf{x} = \begin{bmatrix} q_2 & \dot{q}_2 & p_a & p_b & p_h & p_{o,1} & p_{o,2} & s_s & w_s & \lambda_+ & \lambda_- \end{bmatrix}^{\mathrm{T}} \in \mathbb{R}^{11}. \tag{5.40}$$

5.5 Reduced-Order Model

The goal of developing a reduced-order model is to simplify a complex system while retaining its essential dynamics and characteristics. This simplification allows for more efficient design, and implementation of control strategies. This is especially useful for high-dimensional systems where designing controllers for the full model would be too complex. While reducing the model order can simplify computations, it can also lead to a loss of accuracy. Therefore, the goal is to develop reduced-order models that capture the most important dynamics of the original system while minimizing the computational cost [25, 33].

The reduced-order model of the hydraulic system is derived in two steps. First, it is assumed that the measured pressure p_h is equal to p_a and no hose burst valve is installed in the cylinder. The effect of the hose burst valve is modeled as additional velocity-dependent pressure-compensation term $\Delta p_{ha}(q_2, \dot{q}_2)$ acting on the piston:

$$\begin{aligned} D\ddot{q}_2 + g(q_2) &= J(q_2)\Big[\Big((p_a - \Delta p_{ha}(q_2,\dot{q}_2)\Big)A_a - p_b A_b\Big] - \tau_f(\dot{q}_2) \\ &= J(q_2)(p_a A_a - p_b A_b) - \tau_f(\dot{q}_2) - A_a J(q_2)\Delta p_{ha}(q_2,\dot{q}_2). \end{aligned} \tag{5.41}$$

The term $A_a J(q_2)\Delta p_{ha}(q_2, \dot{q}_2)$ can be viewed as additional friction torque due to the installed hose burst valve:

$$D\ddot{q}_2 + g(q_2) = J(q_2)(p_a A_a - p_b A_b) - \tilde{\tau}_f(q_2, \dot{q}_2), \tag{5.42a}$$
$$\tilde{\tau}_f(q_2, \dot{q}_2) = \tau_f + A_a J(q_2)\Delta p_{ha}(q_2, \dot{q}_2). \tag{5.42b}$$

In the next step, the pressure dynamics in the hydraulic accumulators is eliminated and it is assumed that $p_{o,1} = p_{o,2} = p_a$. The chamber volume V_a is modeled as function of

Die approbierte gedruckte Originalversion dieser Diplomarbeit ist an der TU Wien Bibliothek verfügbar
The approved original version of this thesis is available in print at TU Wien Bibliothek.
TU Bibliothek Your knowledge hub WIEN

p_a and s_p:

$$V_a(p_a, s_p) = \begin{cases} V_{0,a} + A_a s_p, & \text{if } p_a \leq p_{g0,2}, \\ V_{0,a} + A_a s_p + V_{o,1}(p_a), & \text{if } p_{g0,2} < p_a < p_{g0,1}, \\ V_{0,a} + A_a s_p + V_{o,1}(p_a) + V_{o,2}(p_a), & \text{if } p_a \geq p_{g0,1}, \end{cases} \tag{5.43}$$

with

$$V_{o,1}(p_a) = V_{g0} - \left(\frac{\zeta_{0,1}}{p_a}\right)^{1/\kappa}, \quad \zeta_{0,1} = p_{g0,1} V_{g0}^{\kappa}, \tag{5.44a}$$

$$V_{o,2}(p_a) = V_{g0} - \left(\frac{\zeta_{0,2}}{p_a}\right)^{1/\kappa}, \quad \zeta_{0,2} = p_{g0,2} V_{g0}^{\kappa}. \tag{5.44b}$$

The additional volumes $V_{o,1}, V_{o,2}$ in V_a is due to the variable pressure-dependent oil volume in the hydraulic accumulators. The time derivative of p_a can now be written as:

$$\dot{p}_a = \begin{cases} \beta \dfrac{q_a - A_a w_p}{V_{0,a} + A_a s_p}, & \text{if } p_a \leq p_{g0,2}, \\ \dfrac{\kappa \beta p_a (q_a - A_a w_p)}{\kappa p_a (V_{0,a} + A_a s_p + V_{g0,2}) + (\beta - \kappa p_a)\left(\frac{\zeta_{0,2}}{p_a}\right)^{1/\kappa}}, & \text{if } p_{g0,2} < p_a < p_{g0,1}, \\ \dfrac{\kappa \beta p_a (q_a - A_a w_p)}{\kappa p_a (\bar{V}_{0,a} + A_a s_p) + (\beta - \kappa p_a)\left[\left(\frac{\zeta_{0,1}}{p_a}\right)^{1/\kappa} + \left(\frac{\zeta_{0,2}}{p_a}\right)^{1/\kappa}\right]}, & \text{if } p_a \geq p_{g0,1}, \end{cases} \tag{5.45}$$

with $\bar{V}_{0,a} = V_{0,a} + V_{g0,1} + V_{g0,2}$.

The full model is simplified to an 8th-order nonlinear dynamic system with state vector

$$\mathbf{x} = \begin{bmatrix} q_2 & \dot{q}_2 & p_a & p_b & s_s & w_s & \lambda_+ & \lambda_- \end{bmatrix}^{\mathrm{T}} \in \mathbb{R}^8, \tag{5.46}$$

and described by the following set of equations:

$$D\ddot{q}_2 + g(q_2) = J(q_2)\Big[\Big((p_a - \Delta p_{ha}(q_2, \dot{q}_2)\Big) A_a - p_b A_b\Big] - \tau_f(\dot{q}_2), \tag{5.47a}$$

$$\tau_f = \begin{cases} \tau_{C_+} \tanh\left(\dfrac{\dot{q}_2}{\sigma}\right) + k_{v_+} \dot{q}_2, & \text{if } \dot{q}_2 \geq 0, \\ \tau_{C_-} \tanh\left(\dfrac{\dot{q}_2}{\sigma}\right) + k_{v_-} \dot{q}_2, & \text{if } \dot{q}_2 < 0, \end{cases} \tag{5.47b}$$

$$\dot{p}_a = \begin{cases} \beta \dfrac{q_a - A_a w_p}{V_{0,a} + A_a s_p}, & \text{if } p_a \leq p_{g0,2}, \\ \dfrac{\kappa \beta p_a (q_a - A_a w_p)}{\kappa p_a (V_{0,a} + A_a s_p + V_{g0,2}) + (\beta - \kappa p_a)\left(\frac{\zeta_{0,2}}{p_a}\right)^{1/\kappa}}, & \text{if } p_{g0,2} < p_a < p_{g0,1}, \\ \dfrac{\kappa \beta p_a (q_a - A_a w_p)}{\kappa p_a (\bar{V}_{0,a} + A_a s_p) + (\beta - \kappa p_a)\left[\left(\frac{\zeta_{0,1}}{p_a}\right)^{1/\kappa} + \left(\frac{\zeta_{0,2}}{p_a}\right)^{1/\kappa}\right]}, & \text{if } p_a \geq p_{g0,1}, \end{cases} \tag{5.47c}$$

Die approbierte gedruckte Originalversion dieser Diplomarbeit ist an der TU Wien Bibliothek verfügbar
The approved original version of this thesis is available in print at TU Wien Bibliothek.
TU Bibliothek Your knowledge hub WIEN

$$\dot{p}_b = \frac{\beta}{V_{0,b} + (l_p - s_p)A_b}(q_b + w_p A_b), \tag{5.47d}$$

$$q_a = \begin{cases} C_d A_{sa}(s_s)\sqrt{\frac{2}{\rho}}\sqrt{\Delta p_c}, & \text{if } s_s < 0, \\ \operatorname{sgn}(p_t - p_h) C_d A_{ta}(s_s)\sqrt{\frac{2}{\rho}}\sqrt{|p_h - p_t|}, & \text{if } s_s \geq 0, \end{cases} \tag{5.47e}$$

$$q_b = \begin{cases} C_d A_{sb}(s_s)\sqrt{\frac{2}{\rho}}\sqrt{\Delta p_c}, & \text{if } s_s \geq 0, \\ \operatorname{sgn}(p_t - p_b) C_d A_{tb}(s_s)\sqrt{\frac{2}{\rho}}\sqrt{|p_b - p_t|}, & \text{if } s_s < 0, \end{cases} \tag{5.47f}$$

and (5.39n) - (5.39u).

5.6 Simulation and Experimental Validation

To simulate and validate the system, both the full and reduced-order models were implemented in MATLAB/SIMULINK. The dynamic models of the pilot valves were implemented using MATLAB *Transfer Fcn* blocks according to (3.32), while the remaining components of the hydraulic system and the equation of motion for the inner boom were implemented using MATLAB *Function* blocks. The system was simulated in the continuous-time domain using the variable-step solver *ode15s*. First, the full model was validated against the measurements, and then the reduced-order model was compared to the full model.

To evaluate the full model, the measured solenoid currents i_+, i_- from the test trajectories are used as inputs to the MATLAB/SIMULINK model, and the predicted state variables $p_h, p_b, q_2, \dot{q}_2$ are compared to the corresponding measurements. The four validation trajectories reported in this work are summarized in Table 5.1. The table lists the positions of the outer and telescopic booms, load conditions during the measurements, and the achieved accuracy of the full model. For simplicity, the remaining generalized coordinates were omitted as they do not affect the inner boom's dynamics. The model's accuracy for each validation trajectory is assessed by calculating the mean absolute difference between the predicted and measured angles of the inner boom:

$$\text{MAE} = \frac{1}{n}\sum_{i=1}^{n} |q_2(t_i) - \hat{q}_2(t_i)|, \tag{5.48}$$

where q_2 denotes the predicted inner boom angle, $\hat{q}_2$ the measured inner boom angle and t_i the sampling points. Figure 5.12 - Figure 5.15 present the validation trajectories and the qualitative results comparing the measured data and the model's prediction. The trajectories vary in terms of environmental and load conditions, as well as dynamic behavior. The first two trajectories were measured indoors with the crane in a folded position (i.e., $q_3 = 4.59\,\text{rad}$) and with a retracted telescopic boom. This configuration is characterized by the lowest absolute value of the potential force $g(\mathbf{q})$ and, consequently, the lowest load pressure. The first trajectory in Figure 5.12 represents a slowly-varying movement simulating a repetitive push-pull operation, while the second trajectory in

Die approbierte gedruckte Originalversion dieser Diplomarbeit ist an der TU Wien Bibliothek verfügbar
The approved original version of this thesis is available in print at TU Wien Bibliothek.
TU Bibliothek Your knowledge hub WIEN

Trajectory	q_3 [rad]	q_4 [m]	Log	MAE [rad]
1	4.59	0	No	0.019
2	4.59	0	No	0.021
3	0.28	2.2	No	0.035
4	0.28	2.8	Yes	0.037

Table 5.1: Description of the validation trajectories and the prediction error of the full model in comparison to the measurements.

Figure 5.13, with a general shape, was included to demonstrate the model's robustness in highly dynamic applications. The third and fourth trajectories, depicted in Figure 5.14, Figure 5.15, were measured outdoors with an extended telescopic boom and an outer boom angle of $q_3 = 0.28\,\text{rad}$ to mimic real-world operational conditions. The third trajectory was recorded with an empty gripper, while the fourth trajectory corresponds to the highest load pressure scenario with a wooden log in the gripper. Due to limitations in the measurement setup, the exact mass of the log was not directly measured. Instead, it was approximated based on its volume and wood density.

The quantitative and qualitative analysis indicates that the model achieves high accuracy when compared with indoor measurements. However, in outdoor experiments involving the highest load pressure, the model's accuracy decreases slightly. Factors contributing to this performance drop include discrepancies between the modeled and actual friction forces in the cylinder, inaccuracies in the crane's kinematic and load models, unmodeled dynamics of the hose burst valve, rough estimations of the main valve parameters, and the assumption of constant fluid compressibility.

Die approbierte gedruckte Originalversion dieser Diplomarbeit ist an der TU Wien Bibliothek verfügbar
The approved original version of this thesis is available in print at TU Wien Bibliothek.
TU Bibliothek Your knowledge hub WIEN

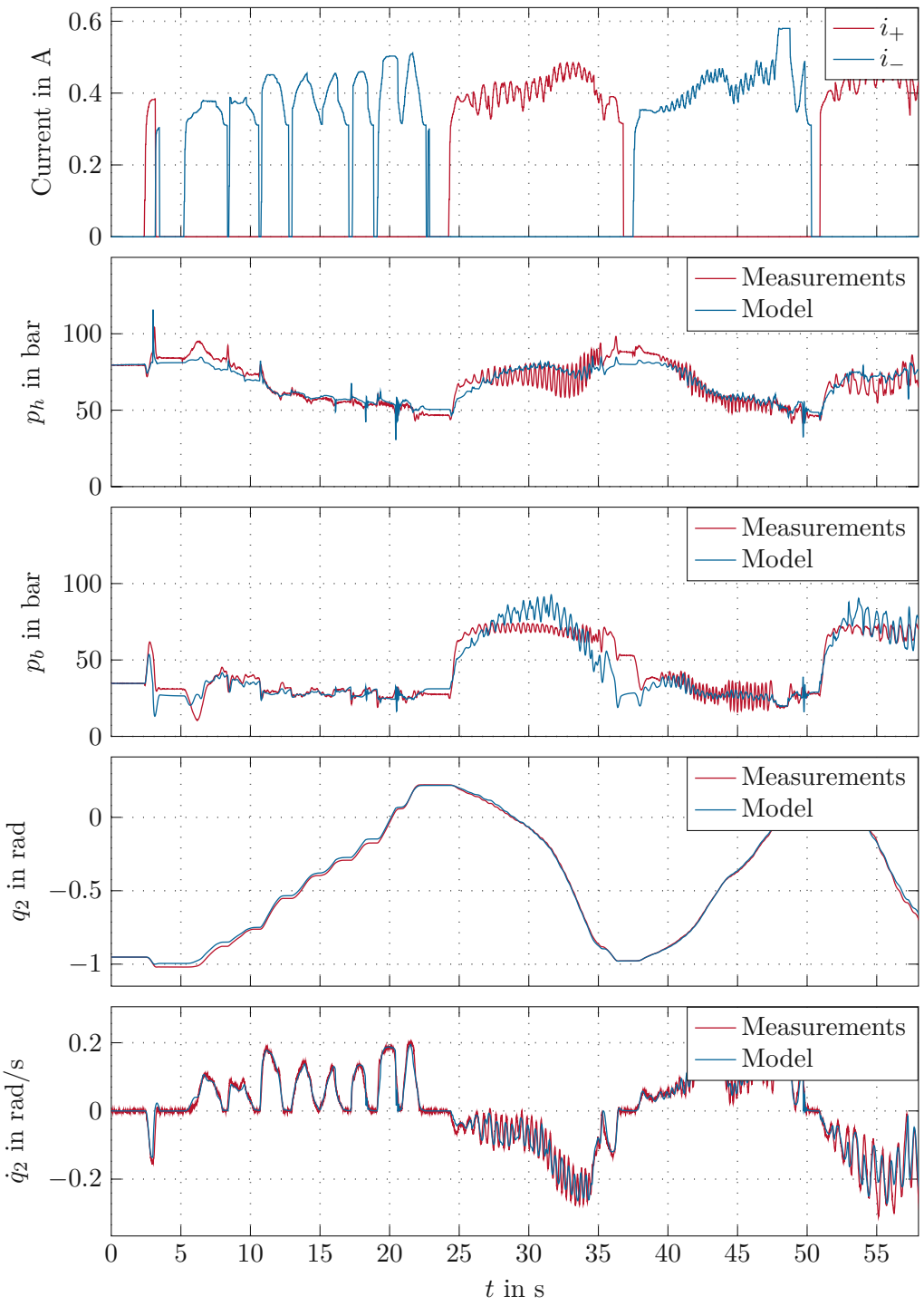

Figure 5.12: Comparison of the measurements with the full model's predictions for Trajectory 1 from the validation dataset.

Die approbierte gedruckte Originalversion dieser Diplomarbeit ist an der TU Wien Bibliothek verfügbar
The approved original version of this thesis is available in print at TU Wien Bibliothek.
TU Bibliothek Your knowledge hub WIEN

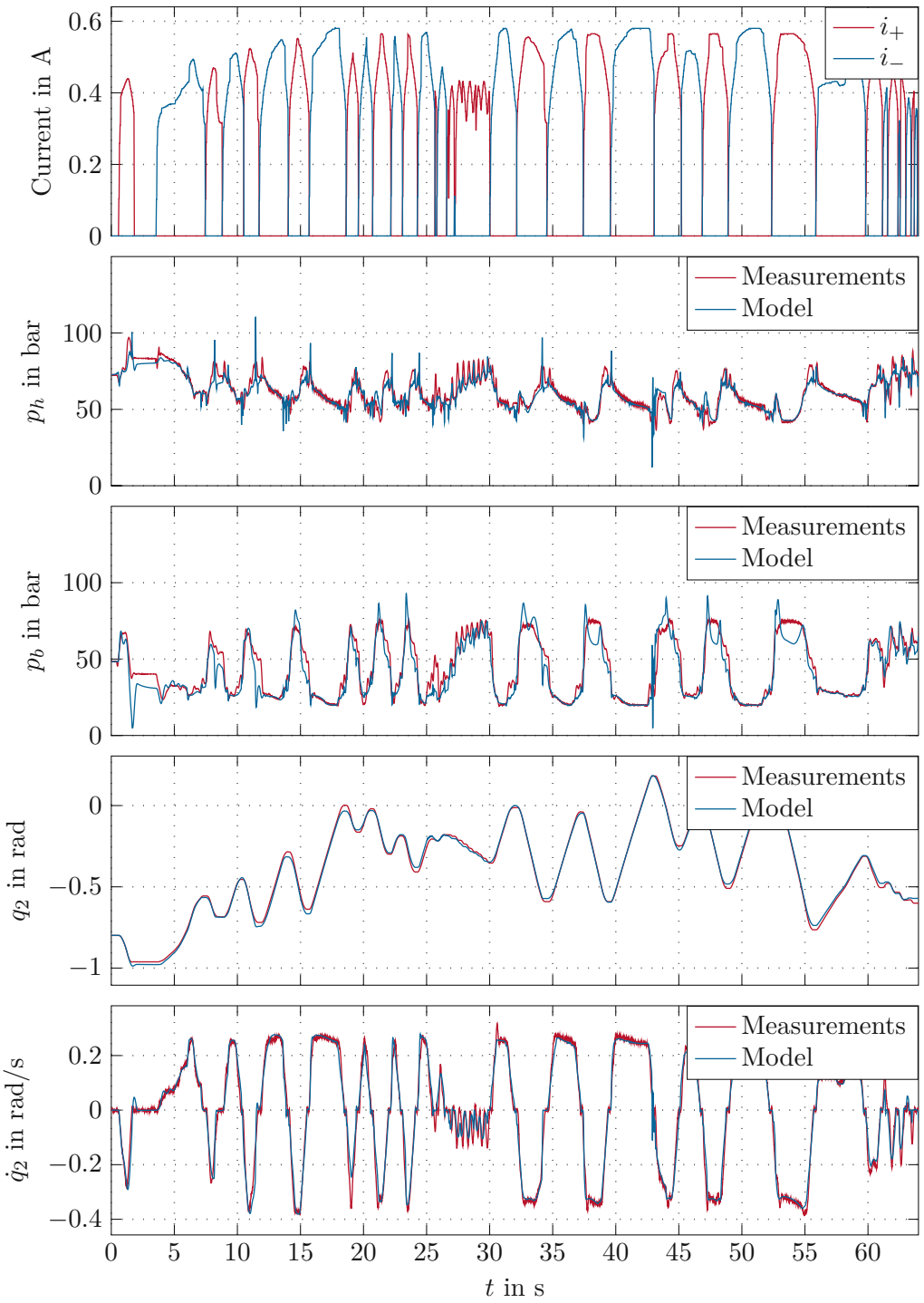

Figure 5.13: Comparison of the measurements with the full model's predictions for Trajectory 2 from the validation dataset.

Die approbierte gedruckte Originalversion dieser Diplomarbeit ist an der TU Wien Bibliothek verfügbar
The approved original version of this thesis is available in print at TU Wien Bibliothek.

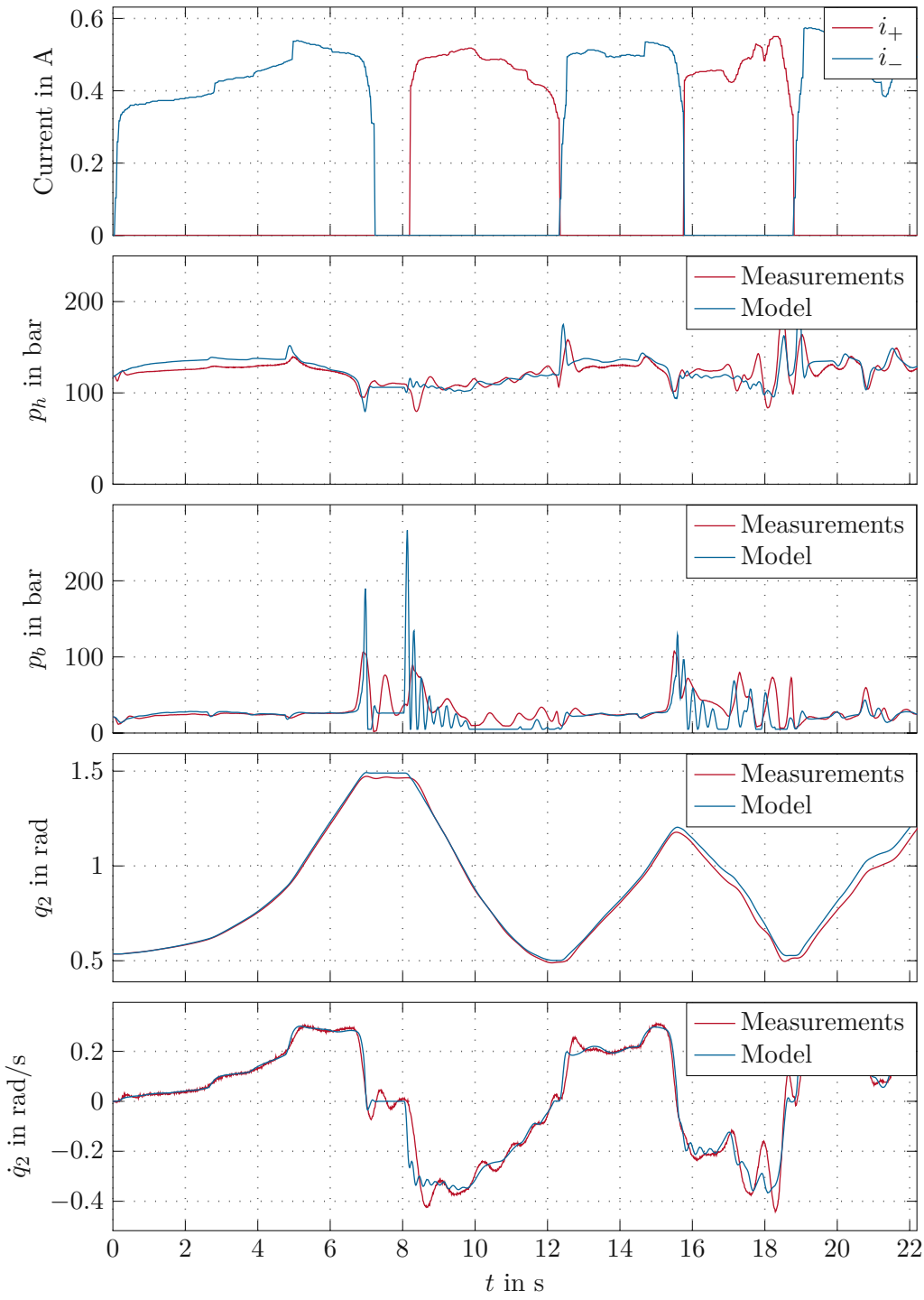

Figure 5.14: Comparison of the measurements with the full model's predictions for Trajectory 3 from the validation dataset.

Die approbierte gedruckte Originalversion dieser Diplomarbeit ist an der TU Wien Bibliothek verfügbar
The approved original version of this thesis is available in print at TU Wien Bibliothek.
TU Bibliothek Your knowledge hub WIEN

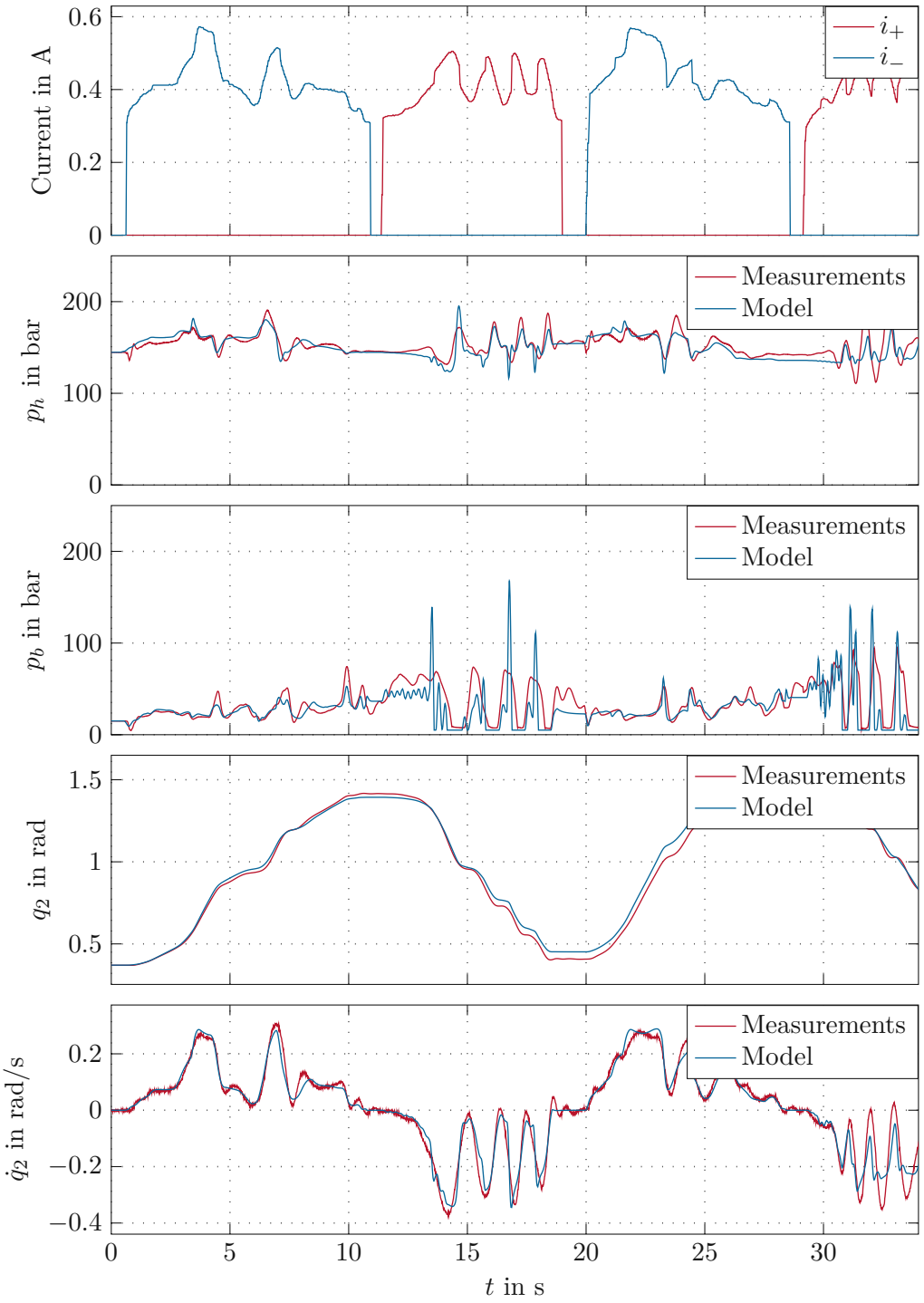

Figure 5.15: Comparison of the measurements with the full model's predictions for Trajectory 4 from the validation dataset.

Die approbierte gedruckte Originalversion dieser Diplomarbeit ist an der TU Wien Bibliothek verfügbar
The approved original version of this thesis is available in print at TU Wien Bibliothek.

Finally, the full model is compared against the reduced-order model using the same four validation trajectories. The reduced-order model's accuracy was evaluated by calculating the mean absolute difference between the inner boom angle predicted by the full model and that predicted by the reduced-order model. Table 5.2 summarizes the validation trajectories and the achieved accuracy of the reduced-order model. The qualitative results are shown in Figure 5.16 - Figure 5.19. As illustrated in the figures, the reduced-order model effectively approximates the full model in both indoor and outdoor experiments. The difference between the full model and the reduced-order model is most evident in the scenarios during high-frequency pressure variations in the cylinder, which cause the hydraulic accumulators to undergo pressurization and depressurization. In such cases, the dynamics of the hydraulic accumulators become significant and can no longer be ignored, leading to mismatch between the reduced-order and full models. However, while these discrepancies are apparent in the hydraulic pressures, their effect on the hydraulic force $f_p = p_a A_a - p_b A_b$ and consequently on the position and velocity of the inner boom is minimal. These findings suggest that the reduced-order model is well-suited for controller design purposes.

Trajectory	q_3 [rad]	q_4 [m]	Log	MAE [rad]
1	4.59	0	No	0.009
2	4.59	0	No	0.018
3	0.28	2.2	No	0.013
4	0.28	2.8	Yes	0.025

Table 5.2: Description of the validation trajectories and the prediction error of the reduced-order model compared to the full model.

Die approbierte gedruckte Originalversion dieser Diplomarbeit ist an der TU Wien Bibliothek verfügbar
The approved original version of this thesis is available in print at TU Wien Bibliothek.

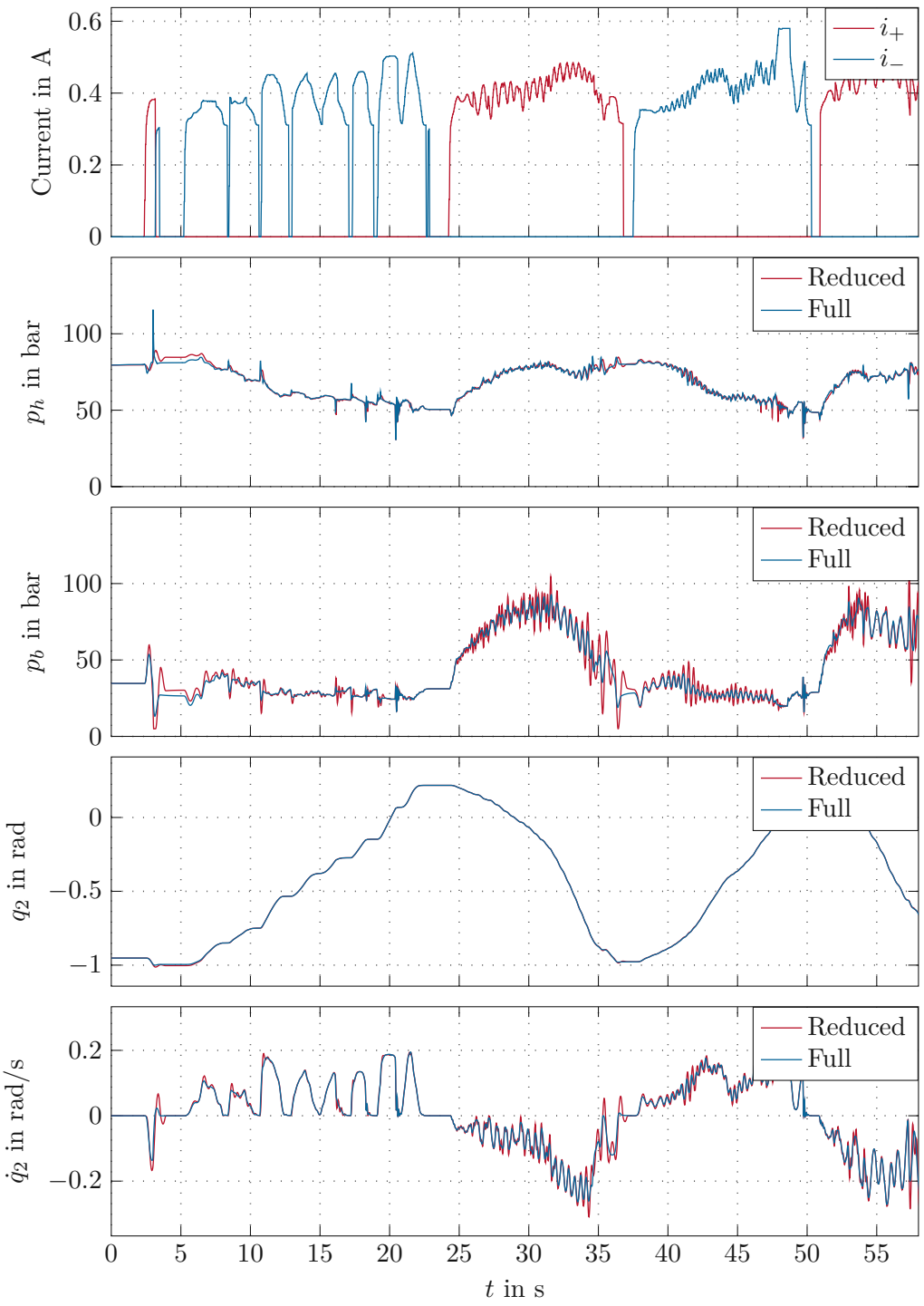

Figure 5.16: Comparison of the full model and the reduced-order model for Trajectory 1 from the validation dataset.

Die approbierte gedruckte Originalversion dieser Diplomarbeit ist an der TU Wien Bibliothek verfügbar
The approved original version of this thesis is available in print at TU Wien Bibliothek.

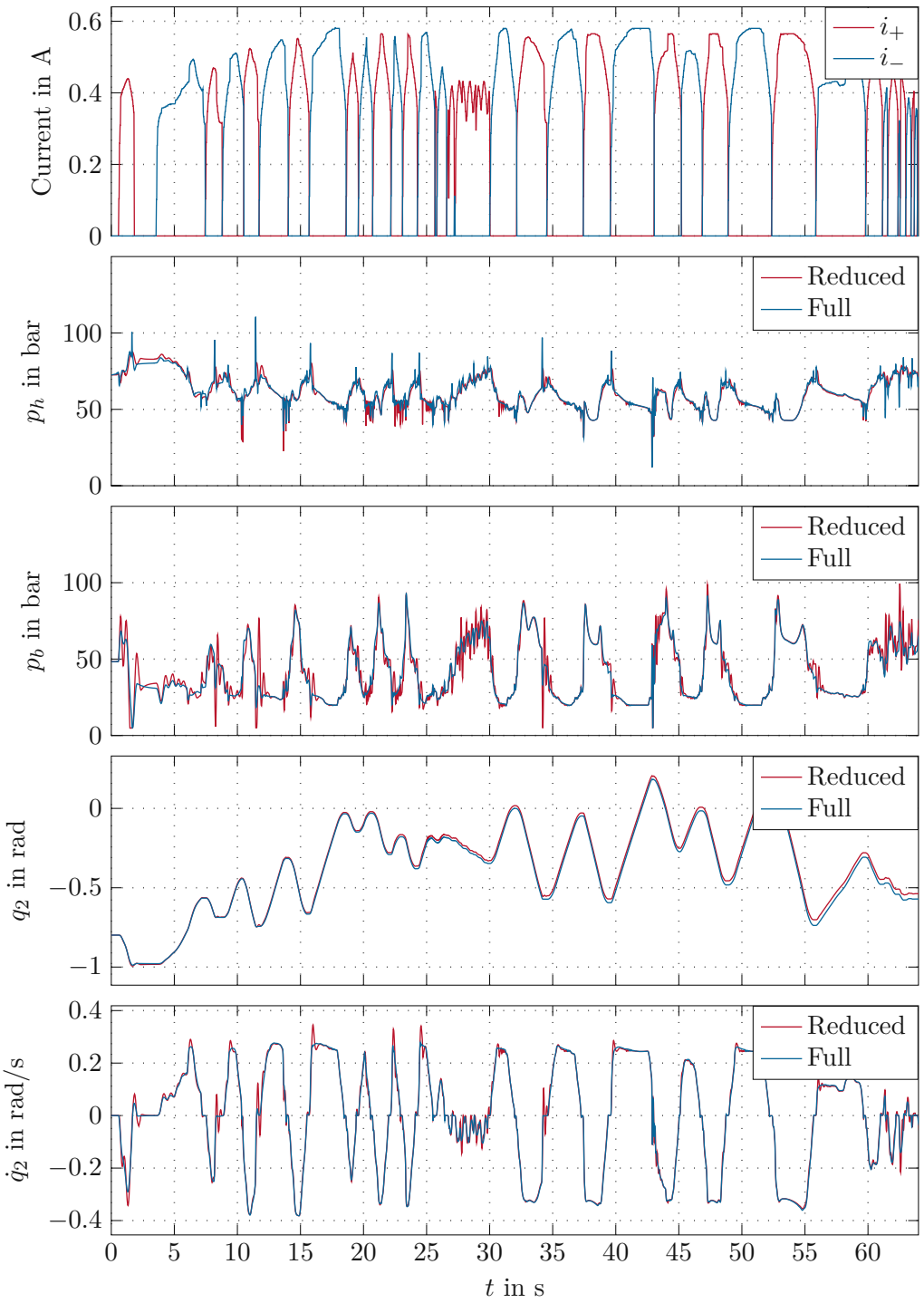

Figure 5.17: Comparison of the full model and the reduced-order model for Trajectory 2 from the validation dataset.

Die approbierte gedruckte Originalversion dieser Diplomarbeit ist an der TU Wien Bibliothek verfügbar
The approved original version of this thesis is available in print at TU Wien Bibliothek.

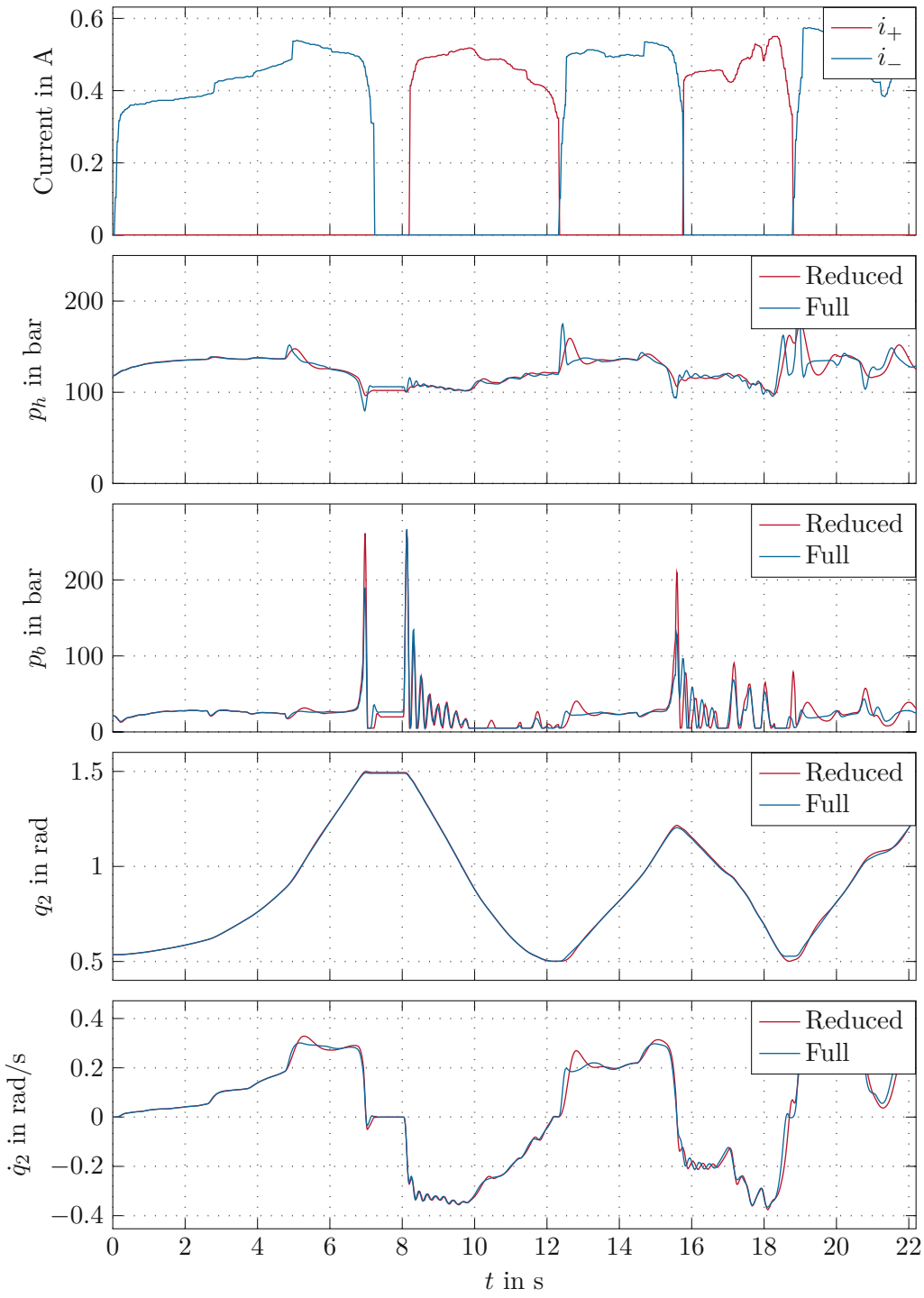

Figure 5.18: Comparison of the full model and the reduced-order model for Trajectory 3 from the validation dataset.

Die approbierte gedruckte Originalversion dieser Diplomarbeit ist an der TU Wien Bibliothek verfügbar
The approved original version of this thesis is available in print at TU Wien Bibliothek.

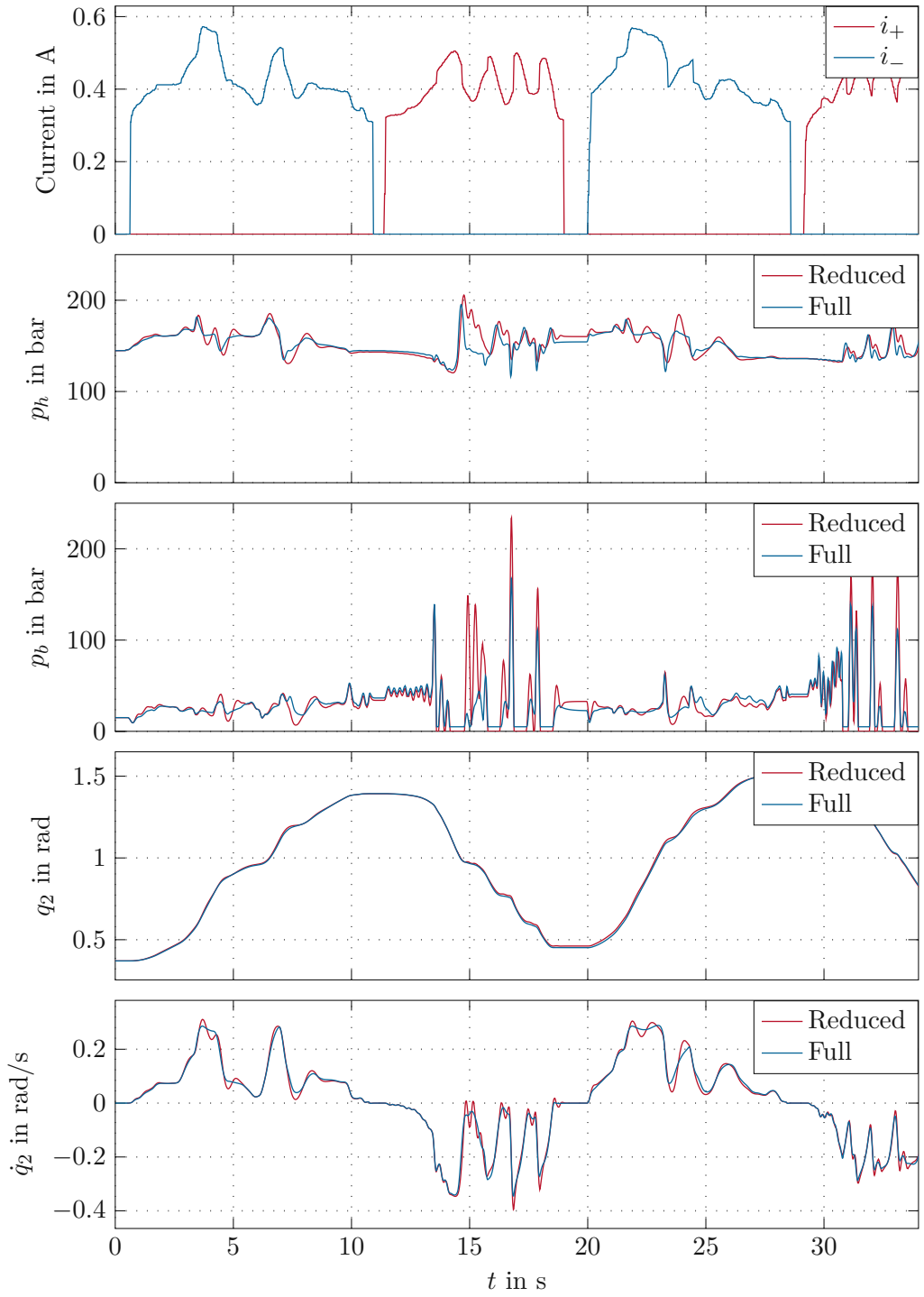

Figure 5.19: Comparison of the full model and the reduced-order model for Trajectory 4 from the validation dataset.

Die approbierte gedruckte Originalversion dieser Diplomarbeit ist an der TU Wien Bibliothek verfügbar
The approved original version of this thesis is available in print at TU Wien Bibliothek.

6 Control System Design

This chapter details the design of a tracking controller for the inner boom. The primary goal of the controller is to regulate the motion of the inner boom so that it accurately follows a given reference trajectory $q_2^*(t)$. The block diagram of the tracking controller is shown in Figure 6.1. The tracking controller is a cascade controller, composed of a feedforward controller, a feedback position controller, and a feedback force controller. The feedforward controller calculates the desired actuator force f_p^f based on the reference trajectory, its derivatives, and the mathematical model of the crane. Due to inevitable discrepancies between the actual behavior and the mathematical model, the feedback position controller is used to stabilize the inner boom's motion along the reference trajectory. The combined output of the feedforward and feedback position controllers, $f_p^* = f_p^f + f_p^c$, serves as the set point for the feedback force controller. The objective of the feedback force controller is to control the hydraulic actuator force by computing the desired solenoid currents i_+^c, i_-^c, ensuring that f_p follows f_p^*. In the following sections, each component of the tracking controller will be derived and discussed in detail. The controller will be designed for the reduced-order model and subsequently validated in MATLAB/SIMULINK using the full model of the inner boom.

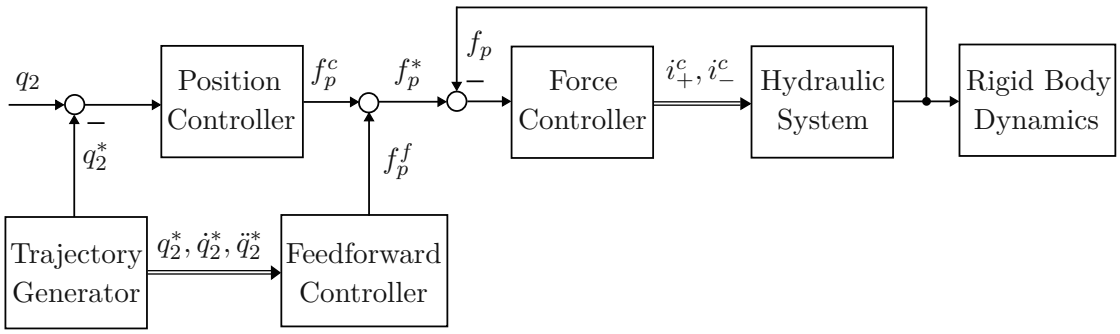

Figure 6.1: Block diagram of the tracking controller.

6.1 Feedforward and Feedback Position Controllers

The equation of motion for the reduced-order inner boom model is expressed as

$$D\ddot{q}_2 + g(q_2) = J(q_2)f_p - \tilde{\tau}_f(q_2, \dot{q}_2). \tag{6.1}$$

The feedforward actuator force for a given reference trajectory q_2^* can be computed from the equation of motion as

$$f_p^f(q_2^*, \dot{q}_2^*, \ddot{q}_2^*) = \frac{1}{J(q_2^*)}\Big(D\ddot{q}_2^* + g(q_2^*) + \tilde{\tau}_f(q_2^*, \dot{q}_2^*)\Big). \tag{6.2}$$

Die approbierte gedruckte Originalversion dieser Diplomarbeit ist an der TU Wien Bibliothek verfügbar
The approved original version of this thesis is available in print at TU Wien Bibliothek.

The control law for the feedback position controller is designed by analyzing the dynamics of the error system

$$\mathbf{x}_e^p = \begin{bmatrix} q_2 - q_2^* \\ \dot{q}_2 - \dot{q}_2^* \end{bmatrix} = \begin{bmatrix} x_{e1}^p \\ x_{e2}^p \end{bmatrix} \tag{6.3a}$$

$$\dot{\mathbf{x}}_e^p = \begin{bmatrix} x_{e2}^p \\ \frac{1}{D}\Big(J(q_2) f_p - g(q_2) - \tilde{\tau}_f(q_2, \dot{q}_2) - J(q_2^*) f_p^f + g(q_2^*) + \tilde{\tau}_f(q_2^*, \dot{q}_2^*) \Big) \end{bmatrix}. \tag{6.3b}$$

After substituting $f_p = f_p^f + f_p^c$ into (6.3b), the dynamics of the error system is given by

$$\dot{\mathbf{x}}_e^p = \begin{bmatrix} x_{e2}^p \\ \frac{1}{D}\Big[J(q_2) f_p^c + \Big(J(q_2) - J(q_2^*) \Big) f_p^f + g(q_2^*) - g(q_2) + \tilde{\tau}_f(q_2^*, \dot{q}_2^*) - \tilde{\tau}_f(q_2, \dot{q}_2) \Big] \end{bmatrix}. \tag{6.4}$$

Since the angle q_2 and the angular velocity $\dot{q}_2$ are measurable variables, the nonlinear term in the equation (6.4) can be compensated. The control law

$$f_p^c = \frac{1}{J(q_2)} \Big[- \Big(J(q_2) - J(q_2^*) \Big) f_p^f - \Big(g(q_2^*) - g(q_2) \Big) - \Big(\tilde{\tau}_f(q_2^*, \dot{q}_2^*) - \tilde{\tau}_f(q_2, \dot{q}_2) \Big) + u \Big], \tag{6.5}$$

leads to the linear error system

$$\dot{\mathbf{x}}_e^p = \mathbf{A}\mathbf{x}_e^p + \mathbf{b}u, \tag{6.6a}$$

$$\mathbf{A} = \begin{bmatrix} 0 & 1 \\ 0 & 0 \end{bmatrix}, \quad \mathbf{b} = \begin{bmatrix} 0 \\ \frac{1}{D} \end{bmatrix}, \tag{6.6b}$$

with the new input u. In the next step, the continuous-time linear error system is discretized [30]:

$$\mathbf{x}_{e,k+1}^p = \mathbf{\Phi}\mathbf{x}_{e,k}^p + \mathbf{\Gamma}u_k, \tag{6.7a}$$

$$\mathbf{\Phi} = \exp(\mathbf{A}T_s) = \begin{bmatrix} 1 & T_s \\ 0 & 1 \end{bmatrix}, \tag{6.7b}$$

$$\mathbf{\Gamma} = \int_0^{T_s} \exp(\mathbf{A}\tau) \mathrm{d}\tau \mathbf{b} = \begin{bmatrix} \frac{T_s^2}{2D} \\ \frac{T_s}{D} \end{bmatrix}, \tag{6.7c}$$

where T_s denotes the sampling period. The state vector $\mathbf{x}_{e,k}^p$ of the error system is augmented with the integral component [30]

$$x_{eI,k+1}^p = x_{eI,k}^p + T_s(q_{2,k} - q_{2,k}^*) = x_{eI,k}^p + T_s \boldsymbol{\gamma}^{\mathrm{T}} \mathbf{x}_e^p, \tag{6.8a}$$

Die approbierte gedruckte Originalversion dieser Diplomarbeit ist an der TU Wien Bibliothek verfügbar
The approved original version of this thesis is available in print at TU Wien Bibliothek.
TU Bibliothek Your knowledge hub WIEN

$$\boldsymbol{\gamma} = \begin{bmatrix} 1 \\ 0 \end{bmatrix}, \tag{6.8b}$$

$$q_{2,k} = q_2(kT_s), \quad q^*_{2,k} = q^*_2(kT_s), \tag{6.8c}$$

leading to the augmented error system described by the following equation

$$\underbrace{\begin{bmatrix} \mathbf{x}^p_{e,k+1} \\ x^p_{eI,k+1} \end{bmatrix}}_{\tilde{\mathbf{x}}^p_{e,k+1}} = \underbrace{\begin{bmatrix} \boldsymbol{\Phi} & \mathbf{0} \\ T_s\boldsymbol{\gamma}^{\mathrm{T}} & 1 \end{bmatrix}}_{\tilde{\boldsymbol{\Phi}}} \underbrace{\begin{bmatrix} \mathbf{x}^p_{e,k} \\ x^p_{eI,k} \end{bmatrix}}_{\tilde{\mathbf{x}}^p_{e,k}} + \underbrace{\begin{bmatrix} \boldsymbol{\Gamma} \\ 0 \end{bmatrix}}_{\tilde{\boldsymbol{\Gamma}}} u_k, \tag{6.9a}$$

$$\tilde{\mathbf{x}}^p_{e,k+1} = \tilde{\boldsymbol{\Phi}}\tilde{\mathbf{x}}^p_{e,k} + \tilde{\boldsymbol{\Gamma}} u_k. \tag{6.9b}$$

The control law [30]

$$u_k = \tilde{\mathbf{k}}^{\mathrm{T}}\tilde{\mathbf{x}}^p_{e,k}, \tag{6.10}$$

results in the closed-loop error system

$$\tilde{\mathbf{x}}^p_{e,k+1} = (\tilde{\boldsymbol{\Phi}} + \tilde{\boldsymbol{\Gamma}}\tilde{\mathbf{k}}^{\mathrm{T}})\tilde{\mathbf{x}}^p_{e,k}. \tag{6.11}$$

The controllability matrix $\mathcal{R}\left(\tilde{\boldsymbol{\Phi}}, \tilde{\boldsymbol{\Gamma}}\right)$ of the augmented error system (6.9), defined as

$$\mathcal{R}\left(\tilde{\boldsymbol{\Phi}}, \tilde{\boldsymbol{\Gamma}}\right) = \left[\tilde{\boldsymbol{\Gamma}}, \tilde{\boldsymbol{\Phi}}\tilde{\boldsymbol{\Gamma}}, \tilde{\boldsymbol{\Phi}}^2\tilde{\boldsymbol{\Gamma}}\right], \tag{6.12}$$

has full rank. Thus, Ackermann's formula can be utilized to determine the feedback gain vector $\tilde{\mathbf{k}}^{\mathrm{T}}$ and position the eigenvalues of the closed-loop system's dynamics matrix at desired locations, ensuring stable error dynamics [30]. The poles of the linear system in (6.6a) are placed at -3. The pole placement was carefully tuned after extensive testing on the validation dataset to achieve a balance between tracking performance, robustness, and smoothness. By combining (6.5) and (6.10) the control law for the feedback position controller is expressed as

$$f^c_{p,k} = \frac{1}{J(q_{2,k})}\left[\left(J(q^*_{2,k}) - J(q_{2,k})\right)f^f_{p,k} - g(q^*_{2,k}) + g(q_{2,k}) - \tilde{\tau}_f(q^*_{2,k}, \dot{q}^*_{2,k}) + \tilde{\tau}_f(q_{2,k}, \dot{q}_{2,k}) + u_k\right], \tag{6.13a}$$

$$u_k = \tilde{\mathbf{k}}^{\mathrm{T}}\tilde{\mathbf{x}}^p_{e,k}, \tag{6.13b}$$

$$f^f_{p,k} = \frac{1}{J(q^*_{2,k})}\left(D\ddot{q}^*_{2,k} + g(q^*_{2,k}) + \tilde{\tau}_f(q^*_{2,k}, \dot{q}^*_{2,k})\right). \tag{6.13c}$$

It is important to note that while the nonlinear compensation term in (6.5) is assumed to be evaluated continuously, this is not feasible on a digital computer with a finite sampling rate. However, for applications where a sufficiently high sampling rate can be used, discrete-time evaluation of the control law usually leads to satisfying results [36].

Die approbierte gedruckte Originalversion dieser Diplomarbeit ist an der TU Wien Bibliothek verfügbar
The approved original version of this thesis is available in print at TU Wien Bibliothek.
TU Bibliothek Your knowledge hub WIEN

6.2 Feedback Force Controller

The control law for the feedback force controller is derived by analyzing the following error system:

$$x_e^f = f_p - f_p^*, \tag{6.14}$$

with $f_p^* = f_p^f + f_p^c$. The desired dynamics of the error system (6.14) can be expressed as

$$\dot{x}_e^f = \dot{f}_p - \dot{f}_p^* = -k_p x_e^f - k_i \int x_e^f \, \mathrm{d}t. \tag{6.15}$$

Calculating the time derivative $\dot{f}_p^*$ requires differentiating the measured signal, which inherently amplifies noise and leads to poor estimation of $\dot{f}_p^*$. To address this issue, the time derivative is approximated using the time derivative of the feedforward force

$$\dot{f}_p^* \approx \dot{f}_p^f. \tag{6.16}$$

By substituting (6.16) into (6.15), the dynamics of the error system can be written as

$$\dot{x}_e^f = \dot{f}_p - \dot{f}_p^f = \dot{p}_a A_a - \dot{p}_b A_b - \dot{f}_p^f = -k_p x_e^f - k_i \int x_e^f \, \mathrm{d}t. \tag{6.17}$$

The time derivative of p_a depends on the value of p_a requiring consideration of three distinct cases:

$$\dot{p}_a = \begin{cases} \beta \dfrac{q_a - A_a w_p}{V_{0,a} + A_a s_p}, & \text{if } p_a \leq p_{g0,2}, \\ \dfrac{\kappa \beta p_a (q_a - A_a w_p)}{\kappa p_a (V_{0,a} + A_a s_p + V_{g0,2}) + (\beta - \kappa p_a)\left(\dfrac{\zeta_{0,2}}{p_a}\right)^{1/\kappa}}, & \text{if } p_{g0,2} < p_a < p_{g0,1}, \\ \dfrac{\kappa \beta p_a (q_a - A_a w_p)}{\kappa p_a (\bar{V}_{0,a} + A_a s_p) + (\beta - \kappa p_a)\left[\left(\dfrac{\zeta_{0,1}}{p_a}\right)^{1/\kappa} + \left(\dfrac{\zeta_{0,2}}{p_a}\right)^{1/\kappa}\right]}, & \text{if } p_a \geq p_{g0,1}, \end{cases} \tag{6.18}$$

To avoid redundancy, the control law derivation will be demonstrated for the case $p_a \leq p_{g0,2}$, as the derivations for other cases follow an analogous procedure. By substituting (6.18) into (6.17), the dynamics of the error system follows as

$$\begin{aligned} \frac{A_a \beta q_a}{V_{0,a} + A_a s_p} - \frac{A_b \beta q_b}{V_{0,b} + (l_p - s_p) A_b} = -k_p x_e^f - k_i \int x_e^f \, \mathrm{d}t + \dot{f}_p^f + \\ + \frac{\beta A_a^2 w_p}{V_{0,a} + A_a s_p} + \frac{\beta A_b^2 w_p}{V_{0,b} + (l_p - s_p) A_b}. \end{aligned} \tag{6.19}$$

There are two cases to consider, based on the sign of the right-hand side of (6.19). If the right-hand side is positive, then $q_a > 0, q_b < 0$ leading to

$$\begin{aligned} A_a \beta \frac{C_d A_{sa}(s_s) \sqrt{\dfrac{2}{\rho}} \sqrt{\Delta p_c}}{V_{0,a} + A_a s_p} - A_b \beta \frac{\operatorname{sgn}(p_t - p_b) C_d A_{tb}(s_s) \sqrt{\dfrac{2}{\rho}} \sqrt{|p_b - p_t|}}{V_{0,b} + (l_p - s_p) A_b} = \\ - k_p x_e^f - k_i \int x_e^f \, \mathrm{d}t + \dot{f}_p^f + \frac{\beta A_a^2 w_p}{V_{0,a} + A_a s_p} + \frac{\beta A_b^2 w_p}{V_{0,b} + (l_p - s_p) A_b} \end{aligned} \tag{6.20}$$

Die approbierte gedruckte Originalversion dieser Diplomarbeit ist an der TU Wien Bibliothek verfügbar
The approved original version of this thesis is available in print at TU Wien Bibliothek.
TU Bibliothek Your knowledge hub WIEN

otherwise $q_a \leq 0$ and $q_b \geq 0$:

$$A_a\beta\frac{\operatorname{sgn}(p_t-p_h)C_dA_{ta}(s_s)\sqrt{\frac{2}{\rho}}\sqrt{|p_h-p_t|}}{V_{0,a}+A_as_p}-A_b\beta\frac{C_dA_{sb}(s_s)\sqrt{\frac{2}{\rho}}\sqrt{\Delta p_c}}{V_{0,b}+(l_p-s_p)A_b}= \\ -k_px_e^f-k_i\int x_e^f\,\mathrm{d}t+\dot{f}_p^f+\frac{\beta A_a^2w_p}{V_{0,a}+A_as_p}+\frac{\beta A_b^2w_p}{V_{0,b}+(l_p-s_p)A_b}. \tag{6.21}$$

After substituting

$$\Psi^+=A_a\beta\frac{C_d\sqrt{\frac{2}{\rho}}\sqrt{\Delta p_c}}{V_{0,a}+A_as_p}, \tag{6.22a}$$

$$\Omega^+=-A_b\beta\frac{\operatorname{sgn}(p_t-p_b)C_d\sqrt{\frac{2}{\rho}}\sqrt{|p_b-p_t|}}{V_{0,b}+(l_p-s_p)A_b}, \tag{6.22b}$$

$$\Psi^-=A_a\beta\frac{\operatorname{sgn}(p_t-p_h)C_d\sqrt{\frac{2}{\rho}}\sqrt{|p_h-p_t|}}{V_{0,a}+A_as_p}, \tag{6.22c}$$

$$\Omega^-=-A_b\beta\frac{C_d\sqrt{\frac{2}{\rho}}\sqrt{\Delta p_c}}{V_{0,b}+(l_p-s_p)A_b}, \tag{6.22d}$$

$$\Sigma=-k_px_e^f-k_i\int x_e^f\,\mathrm{d}t+\dot{f}_p^f+\frac{\beta A_a^2w_p}{V_{0,a}+A_as_p}+\frac{\beta A_b^2w_p}{V_{0,b}+(l_p-s_p)A_b}, \tag{6.22e}$$

into (6.20) and (6.21), the equations can be expressed in a compact form which yields

$$\Psi^+A_{sa}(s_s)+\Omega^+A_{tb}(s_s)=\Sigma, \tag{6.23a}$$

$$\Psi^-A_{tb}(s_s)+\Omega^-A_{sb}(s_s)=\Sigma. \tag{6.23b}$$

The desired spool position, s_s^*, can be determined by solving (6.23) for s_s. However, since the orifice areas are highly nonlinear functions of s_s and the equations cannot be solved analytically, the desired spool position must be determined by numerically solving the nonlinear equation at each sampling step. While this is not a significant issue when the controller is simulated in MATLAB/SIMULINK, it can pose challenges when implemented on a digital computer with limited computational resources. Therefore, for controller implementation, the nonlinear orifice areas are approximated as piecewise linear functions, as illustrated in Figure 6.2 and Figure 6.3. By modeling the orifice areas as piecewise linear functions, a closed-form solution for (6.23) can be obtained, allowing the desired spool position s_s^* to be efficiently computed at each sampling step.

Given known s_s^*, the desired pilot control pressure difference is determined using the static relationship

$$p_+^*-p_-^*=\frac{ks_s^*}{A_s}. \tag{6.24}$$

Die approbierte gedruckte Originalversion dieser Diplomarbeit ist an der TU Wien Bibliothek verfügbar
The approved original version of this thesis is available in print at TU Wien Bibliothek.
TU Bibliothek Your knowledge hub WIEN

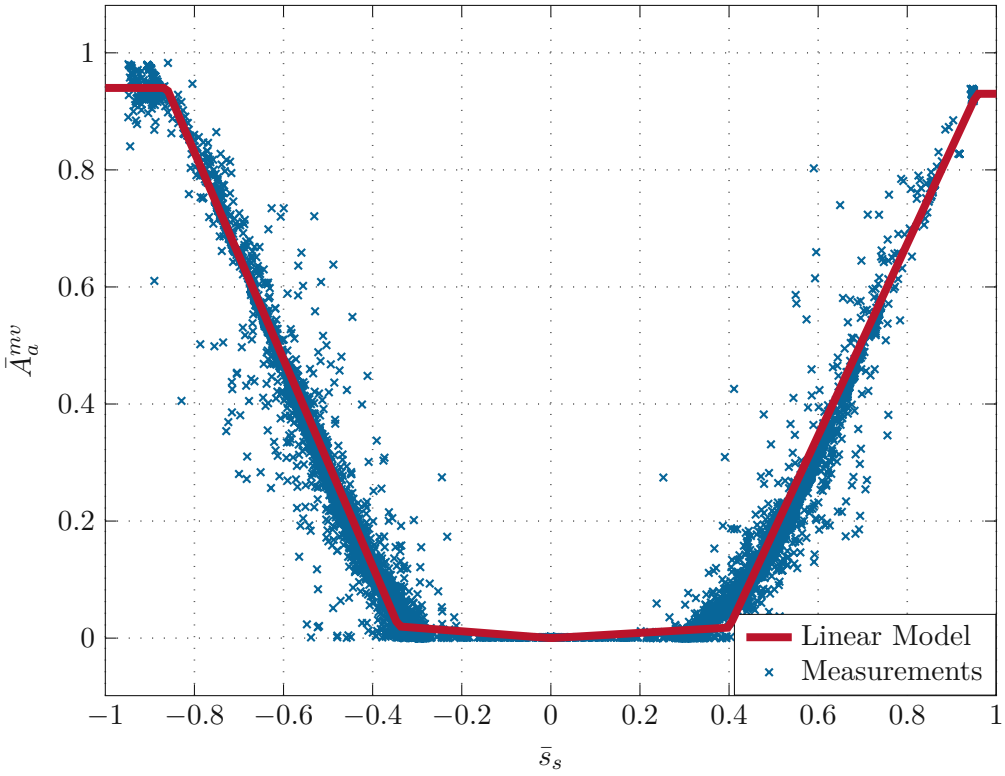

Figure 6.2: Comparison between the linear model of the normalized orifice area $\bar{A}_a^{mv}$ and the measurements.

Die approbierte gedruckte Originalversion dieser Diplomarbeit ist an der TU Wien Bibliothek verfügbar
The approved original version of this thesis is available in print at TU Wien Bibliothek.

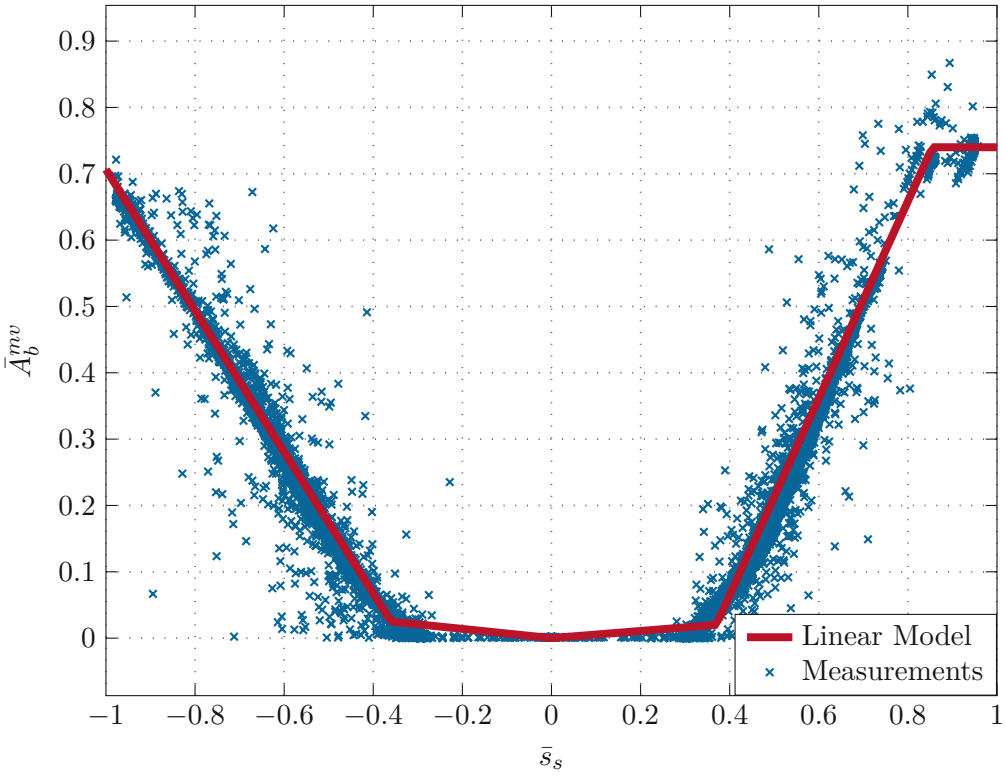

Figure 6.3: Comparison between the linear model of the normalized orifice area $\bar{A}_b^{mv}$ and the measurements.

Die approbierte gedruckte Originalversion dieser Diplomarbeit ist an der TU Wien Bibliothek verfügbar
The approved original version of this thesis is available in print at TU Wien Bibliothek.
TU Bibliothek Your knowledge hub WIEN

To improve the responsiveness of the pilot valves, both pilot valves are assumed to remain active during control. The detailed mapping of the pilot control pressure difference to the individual pressures p_+ and p_- is outside the scope of this work. Instead, a simple linear mapping is assumed. Additionally, the pilot control pressures are offset to 5 bar in the neutral position to reduce the power consumption. The function mapping $p_+ - p_-$ to the pilot control pressures p_+, p_- is illustrated in Figure 6.4. The controller output (i_+^c, i_-^c) is calculated from the desired pilot control pressures (p_+^*, p_-^*) as follows:

$$i_+^c = h^{-1}(p_+^*), \tag{6.25}$$

$$i_-^c = h^{-1}(p_-^*), \tag{6.26}$$

where h^{-1} is the inverse of the static output nonlinearity of the identified pilot valve model.

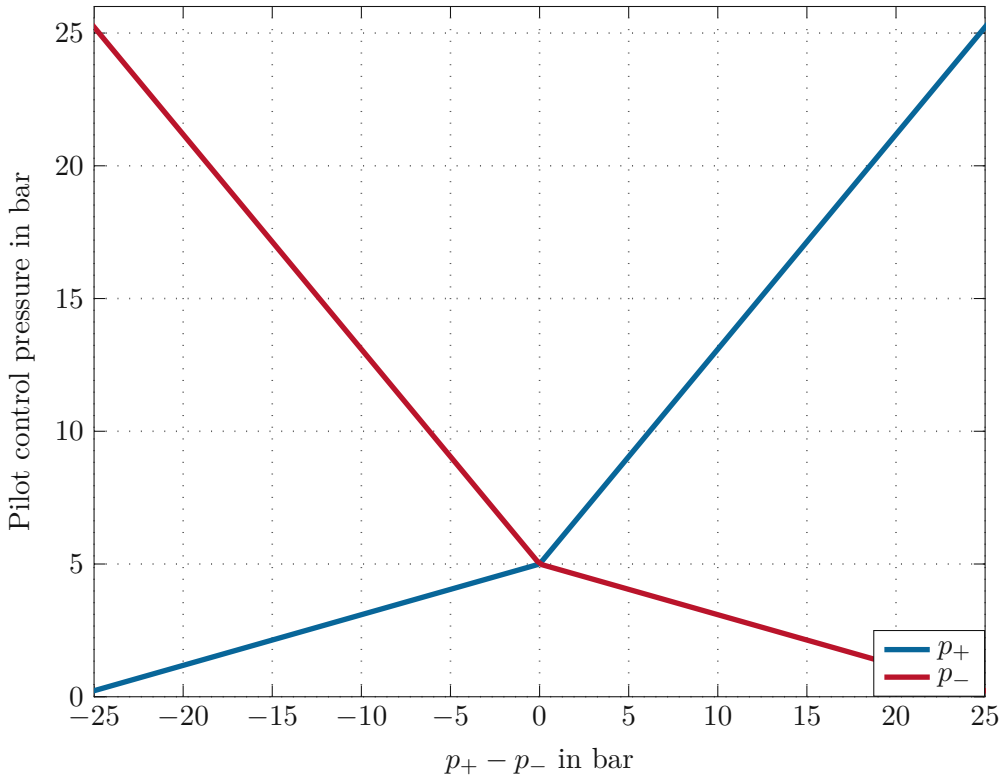

Figure 6.4: The relationship between the pilot control pressure difference and the individual pilot pressures.

6.3 Trajectory Generator

As detailed in the next section, the measured trajectories will be used as desired trajectories to evaluate the controller's performance. To achieve this, a trajectory generator is necessary for filtering the measured trajectories and calculating their time derivatives. The trajectory

Die approbierte gedruckte Originalversion dieser Diplomarbeit ist an der TU Wien Bibliothek verfügbar
The approved original version of this thesis is available in print at TU Wien Bibliothek.

generator is implemented as a state-variable filter, described by the following equations [29]

$$\frac{\mathrm{d}}{\mathrm{d}t}\mathbf{x}_f = \begin{bmatrix} 0 & 1 & 0 & 0 \\ 0 & 0 & 1 & 0 \\ 0 & 0 & 0 & 1 \\ -f_0 & -f_1 & -f_2 & -f_3 \end{bmatrix} \mathbf{x}_f + \begin{bmatrix} 0 \\ 0 \\ 0 \\ 1 \end{bmatrix} u = \mathbf{A}_f \mathbf{x}_f + \mathbf{b}_f u \tag{6.27a}$$

$$\mathbf{y}_f = \begin{bmatrix} y_f \\ \dot{y}_f \\ \ddot{y}_f \\ \dddot{y}_f \end{bmatrix} = \begin{bmatrix} f_0 & 0 & 0 & 0 \\ 0 & f_0 & 0 & 0 \\ 0 & 0 & f_0 & 0 \\ 0 & 0 & 0 & f_0 \end{bmatrix} \mathbf{x}_f = \mathbf{C}_f \mathbf{x}_f, \tag{6.27b}$$

where u represents the measured unfiltered trajectory, and the coefficients f_0, f_1, f_2, f_3 are derived from the desired poles of the state-variable filter's transfer function. The poles are placed at -10 to balance noise reduction and signal fidelity, resulting in a filtered signal that closely resembles the desired trajectory. The next step involves discretizing the continuous-time state-variable filter to handle discrete measured signals, allowing for implementation on a digital computer with a sampling period T_s:

$$\mathbf{x}_{f,k+1} = \mathbf{\Phi}_f \mathbf{x}_{f,k} + \mathbf{\Gamma}_f u_k, \tag{6.28a}$$

$$\mathbf{y}_{f,k} = \mathbf{C}\mathbf{x}_{f,k}, \tag{6.28b}$$

$$\mathbf{\Phi}_f = \exp(\mathbf{A}_f T_s), \quad \mathbf{\Gamma}_f = \int_0^{T_s} \exp(\mathbf{A}_f \tau)\mathrm{d}\tau \mathbf{b}_f, \tag{6.28c}$$

6.4 Controller Implementation and Validation

The trajectory generator and the controllers are implemented in MATLAB/SIMULINK as MATLAB *Function* blocks. The closed-form expressions of the control laws are derived in MAPLE and exported into MATLAB/SIMULINK as MATLAB expressions using the *Matlab* command. For the simulations, the discrete-time function blocks of the controllers and the trajectory generator are updated with a sample time of $T_s = 10\,\mathrm{ms}$, matching the sample time of the available electronic hardware. For the feedback force controller, the parameters k_p, k_i are calculated so that the poles of the error system in (6.15) are placed at -11. This pole placement was chosen after extensive testing to ensure robust performance across the validation trajectories while maintaining precise tracking accuracy. The dynamics of the system is simulated in continuous-time domain and the measurable state variables are sampled with sampling period $T_s = 10\,\mathrm{ms}$ aligning with the sampling time of the installed sensor electronics. To model the real behavior of the sensors, noise is applied to the pressure and angle signals before they are fed to the controllers. The pressure sensor noise is modeled as a combination of white noise and quantization noise, while the angle of the inner boom is only affected by quantization noise. White noise and quantization noise are generated using the *Band-Limited White Noise* and *Quantizer* blocks from the MATLAB/SIMULINK library. The power spectral density (PSD) for the pressure noise is set to $\mathrm{PSD}_p = 3\,\mathrm{MPa}^2/\mathrm{Hz}$, chosen to closely match the measurement data. The quantization interval for the pressure noise is 0.1 bar, and for the angle noise, it is $360°/2^{14}$.

Die approbierte gedruckte Originalversion dieser Diplomarbeit ist an der TU Wien Bibliothek verfügbar
The approved original version of this thesis is available in print at TU Wien Bibliothek.
TU Bibliothek Your knowledge hub WIEN

The angle trajectories measured during the second measurement stage are used as reference trajectories for tracking. These trajectories are fed into the trajectory generator to produce smooth reference trajectories $q_2^*(t)$ and their time derivatives. The controller's tracking performance is assessed in MATLAB/SIMULINK by controlling the system and comparing the actual trajectory of the inner boom with the reference trajectory. To make the results more interpretable, the actual piston position s_s is compared with the reference piston position, defined as $s_p^* = s_p(q_2^*)$. Three metrics are employed to quantitatively evaluate the controller's tracking performance:

$$\text{MAE} = \frac{1}{n}\sum_{i=1}^{n} |s_p(t_i) - s_p^*(t_i)|, \tag{6.29a}$$

$$\text{RMSE} = \sqrt{\frac{\sum_{i=1}^{n}(s_p(t_i) - s_p^*(t_i))^2}{n}}, \tag{6.29b}$$

$$\text{MAXE} = \max_{1\leq i\leq n} |s_p(t_i) - s_p^*(t_i)|, \tag{6.29c}$$

where MAE denotes the mean absolute error, RMSE the root mean square error and MAXE the maximum error for the reference trajectory $s_p^*(t)$. The validation of the tracking controller also includes a robustness test against variations in the system parameters. Four parameters were considered: initial pressure in the hydraulic accumulators $p_{g0,1}, p_{g0,2}$, bulk modulus of the oil β, cylinder friction force $\tilde{\tau}_f$, and load mass. These parameters were perturbed from their nominal values to simulate possible operational conditions. The variation in the initial accumulator pressure is attributed to changes in environmental temperature, while the reduction in bulk modulus value reflects potential air bubble compression and dissolution in the oil. The minimum and maximum values for each parameter are summarized in Table 6.1, representing the expected operational range.

Parameter	Minimum value	Maximum value
$p_{g0,1}, p_{g0,2}$	0.76 × nominal value	1.1 × nominal value
β	0.2 × nominal value	nominal value
$\tilde{\tau}_f$	0.5 × nominal value	1.5 × nominal value
Load	0 kg	2000 kg

Table 6.1: Minimum and maximum parameter values for the control system robustness test.

It's important to note that the maximum bulk modulus value corresponds to the nominal value, and thus only the minimum value is used in the robustness tests. Similarly, since the load is not considered in the controller design, a nominal load of 0 kg is assumed, and only the maximum load value is tested. In total, five test configurations, outlined in Table 6.2, were used for the validation, whereas configuration C0 represents the nominal parameter case.

Die approbierte gedruckte Originalversion dieser Diplomarbeit ist an der TU Wien Bibliothek verfügbar
The approved original version of this thesis is available in print at TU Wien Bibliothek.
TU Bibliothek Your knowledge hub WIEN

Configuration	β	Load	$p_{g0,1}, p_{g0,2}$	$\tilde{\tau}_f$
C0	Nominal	Min.	Nominal	Nominal
C1	Min.	Max.	Min.	Min.
C2	Min.	Max.	Min.	Max.
C3	Min.	Max.	Max.	Min.
C4	Min.	Max.	Max.	Max.

Table 6.2: Test configurations for the control system robustness test.

For each test configuration, nine trajectories from the validation dataset were evaluated. Table 6.3 presents the quantitative results of the controller's performance, averaged across the validation trajectories.

Configuration	MAE [mm]	MAXE [mm]	RMSE [mm]
C0	1.3	7.9	1.9
C1	2.9	21.5	4.4
C2	3.8	32.5	6.1
C3	3.8	33	6
C4	3.7	32.4	5.8

Table 6.3: Tracking performance of the controller while the model parameters were perturbed from their nominal values.

For qualitative illustration, the tracking performance for a single reference trajectory under all test configurations is presented in Figure 6.5 - Figure 6.9. The higher maximum errors observed in configurations C1 - C4 are attributed to the gripped log, which causes the actual trajectory to deviate from the reference trajectory, as evident in the first row of the figures. A time frame of approximately 5 seconds is required to account for the instantaneous load perturbation and stabilize the reference trajectory. As expected, the controller underperforms in scenarios where the reduced-order model fails to accurately approximate the full model. These scenarios include cases where the dynamics of the hydraulic accumulators become significant and during fast retraction of the cylinder, where the impact of the hose burst valve and the resulting pressure difference $p_a - p_h$ becomes pronounced. This underperformance not only reduces tracking accuracy but can also lead to high-frequency, high-amplitude oscillations in the hydraulic force, as evidenced in the test case with nominal parameters and no load mass (Figure 6.5). While these oscillations have only a marginal effect on the piston position and are not harmful in a simulation environment, this behavior must be further investigated and tested on a real crane, as it could potentially lead to system instability. During the simulations, it was observed that the oscillations could be significantly dampened by placing the poles of the force controller less aggressively. However, this approach noticeably worsens overall tracking performance across the validation trajectories. Despite these challenges, the overall quantitative and qualitative results demonstrate the control strategy's ability to handle variations in the

Die approbierte gedruckte Originalversion dieser Diplomarbeit ist an der TU Wien Bibliothek verfügbar
The approved original version of this thesis is available in print at TU Wien Bibliothek.
TU Bibliothek Your knowledge hub WIEN

model parameters and external disturbances. This suggests the controller's suitability for deployment on a real crane, where its strong tracking performance makes it a viable candidate for automated logging tasks.

Die approbierte gedruckte Originalversion dieser Diplomarbeit ist an der TU Wien Bibliothek verfügbar
The approved original version of this thesis is available in print at TU Wien Bibliothek.
TU Bibliothek Your knowledge hub WIEN

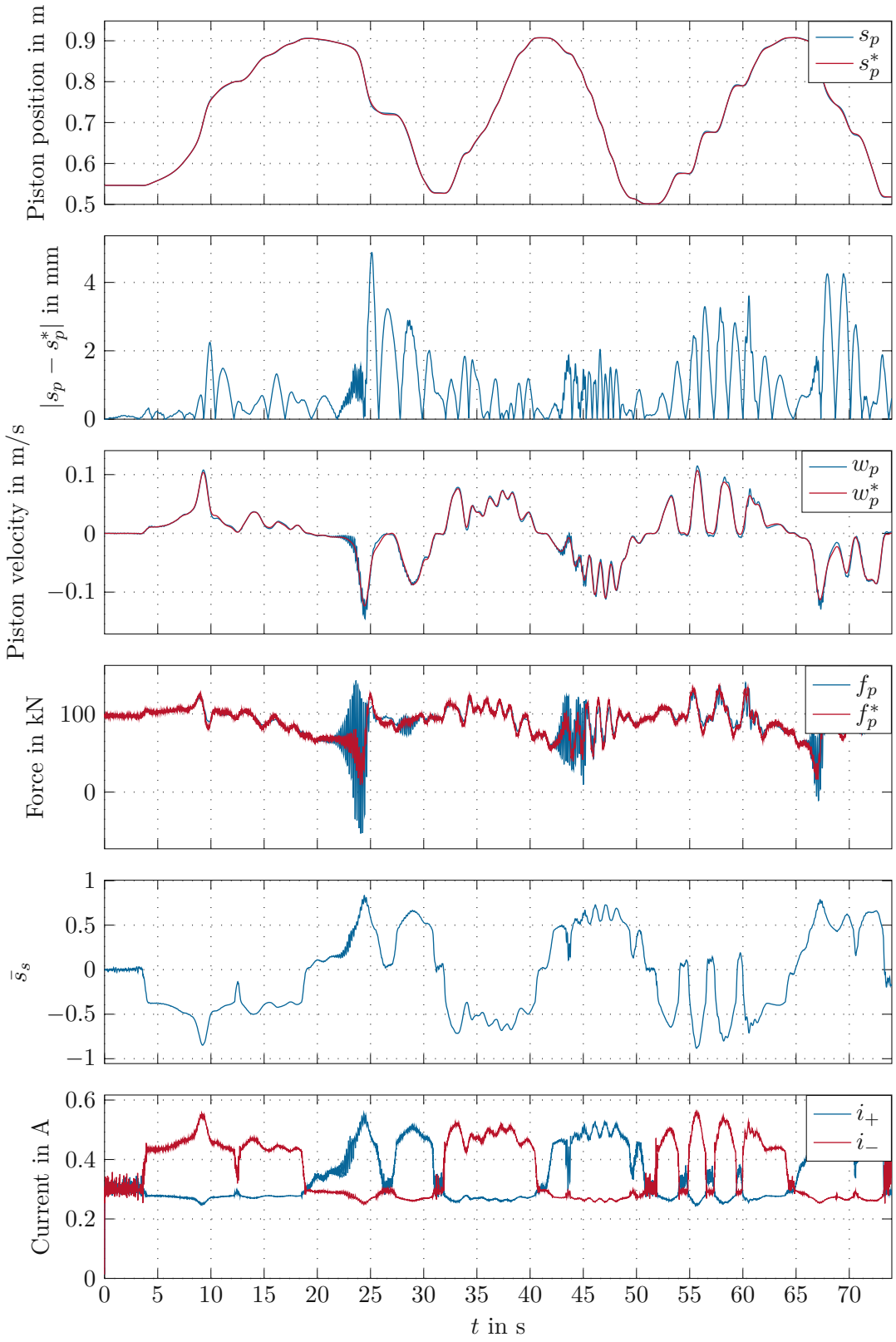

Figure 6.5: Tracking performance with the nominal parameters.

Die approbierte gedruckte Originalversion dieser Diplomarbeit ist an der TU Wien Bibliothek verfügbar
The approved original version of this thesis is available in print at TU Wien Bibliothek.

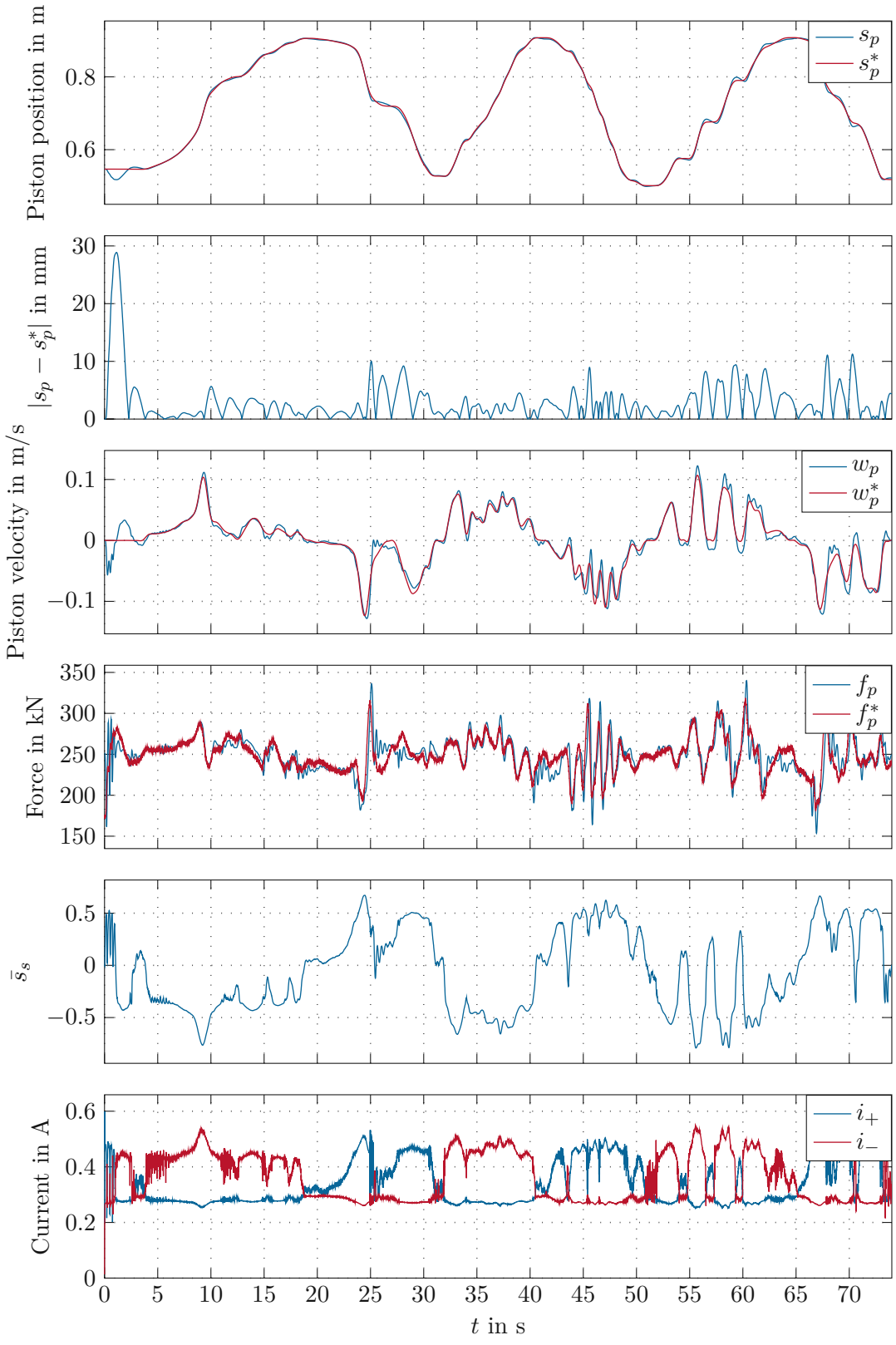

Figure 6.6: Tracking performance with the parameters according to test configuration C1.

Die approbierte gedruckte Originalversion dieser Diplomarbeit ist an der TU Wien Bibliothek verfügbar
The approved original version of this thesis is available in print at TU Wien Bibliothek.

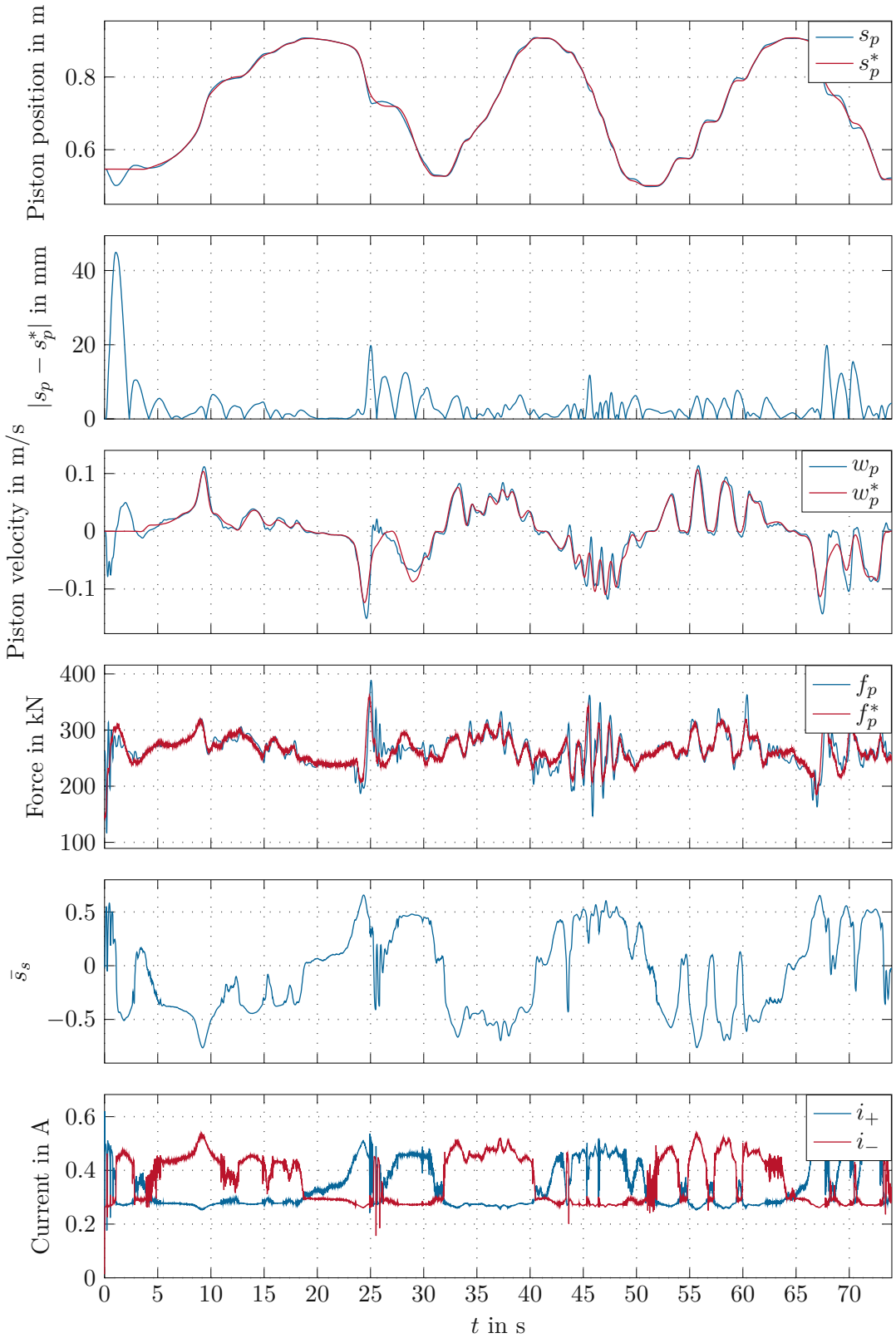

Figure 6.7: Tracking performance with the parameters according to test configuration C2.

Die approbierte gedruckte Originalversion dieser Diplomarbeit ist an der TU Wien Bibliothek verfügbar
The approved original version of this thesis is available in print at TU Wien Bibliothek.

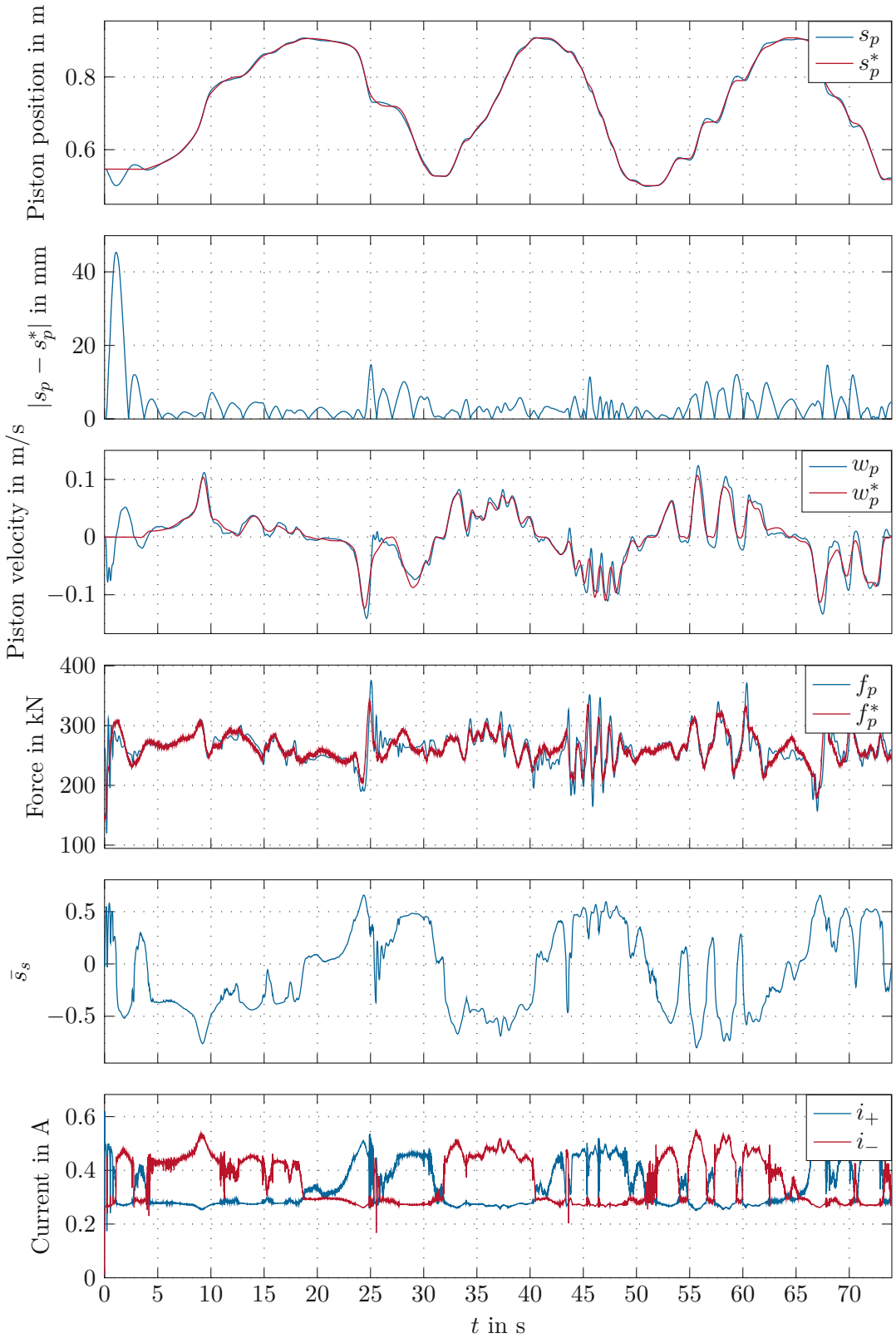

Figure 6.8: Tracking performance with the parameters according to test configuration C3.

Die approbierte gedruckte Originalversion dieser Diplomarbeit ist an der TU Wien Bibliothek verfügbar
The approved original version of this thesis is available in print at TU Wien Bibliothek.

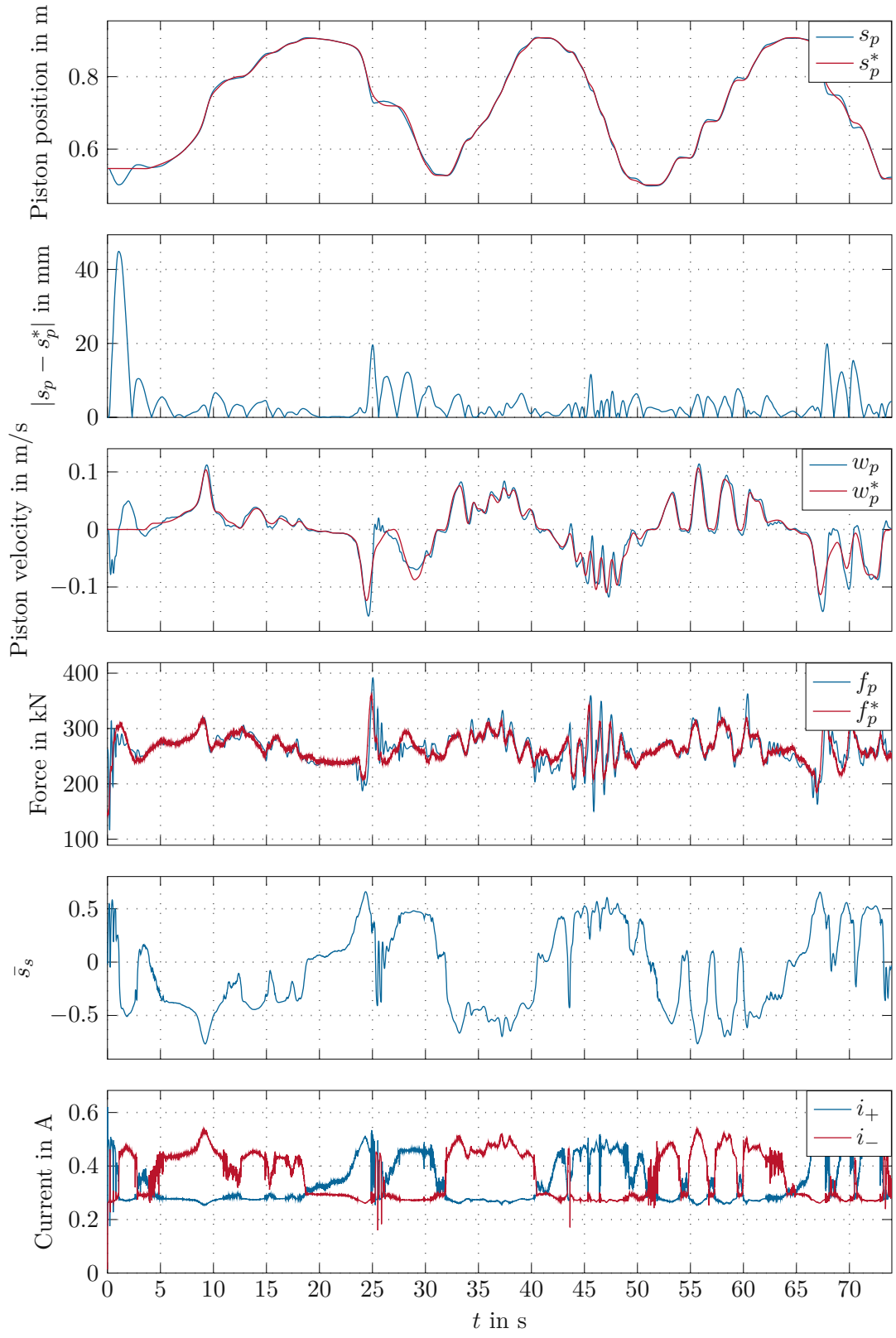

Figure 6.9: Tracking performance with the parameters according to test configuration C4.

Die approbierte gedruckte Originalversion dieser Diplomarbeit ist an der TU Wien Bibliothek verfügbar
The approved original version of this thesis is available in print at TU Wien Bibliothek.

7 Conclusion

This thesis presented an approach for the mathematical modeling and control of the inner boom of a forestry crane *Palfinger Epsilon TZ17*. Starting with the analysis of the original hydraulic circuit, in Chapter 2, a simplified version of the hydraulic circuit is derived where only relevant components are included. The chapter describes the setup under study and gives a short overview of the hydraulic components of the system.

In Chapter 3 the equations of motion of the hydraulic manipulator were formulated using the Euler-Lagrange equations. Since only the inner boom link is analyzed in this work, the equations of motion were further simplified to single equation of motion describing the dynamics of the inner boom link. Additionally, the mathematical models for the hydraulic cylinder, main valve, and hydraulic accumulators were derived and presented.

Chapter 4 outlines detailed description of the measurements conducted in this work, including their corresponding physical setups. The measurements were divided into two stages with the aim of identifying the unknown parameters of the model and validating the mathematical model of the system. In the first stage, the measurements were conducted specifically for the system identification of the pilot valves. In the second stage, cylinder chamber pressures, boom position, and velocity were measured to estimate unknown parameters of the hydraulic system and validate the mathematical model of the entire system.

Chapter 5 focuses on parameter estimation and system identification of the hydraulic components. First, system identification of the pilot valves was described. The behavior of the pilot valves was modeled using a Wiener model - a combination of a linear dynamic system with a static output nonlinearity. Next, parameter estimation of the hose burst valve, the main valve, and P-Spline modeling of the nonlinear orifice areas were presented. By combining the derived and estimated mathematical models of the hydraulic components, the full model was constructed and validated in MATLAB/SIMULINK. Finally, the full model was simplified to the reduced-order model for controller design.

Chapter 6 details the design of the tracking controller. The primary goal of the controller is to regulate the motion of the inner boom so that it accurately follows a given reference trajectory. The tracking controller is a cascaded controller, composed of a feedforward controller, a feedback position controller, and a feedback force controller. The controller was designed for the reduced-order model and subsequently validated in MATLAB/SIMULINK using the full model of the inner boom. The validation of the tracking controller also included the robustness test against variations in system parameters. Four parameters were considered: initial pressure in the hydraulic accumulators, bulk modulus of the oil, cylinder friction force, and load mass. Finally, the quantitative and qualitative results of the evaluation were presented and discussed.

Based on the validation results, it is evident that the mathematical model successfully captures the major dynamics of the system. However, there is potential for further

Die approbierte gedruckte Originalversion dieser Diplomarbeit ist an der TU Wien Bibliothek verfügbar
The approved original version of this thesis is available in print at TU Wien Bibliothek.
TU Bibliothek Your knowledge hub WIEN

improvements by incorporating the dynamics of the hose burst valve and more accurately estimating the main valve parameters, either by disassembling the valve or by measuring the spool position. Additional enhancements could include a more detailed model of the friction force in the hydraulic cylinder and accounting for non-constant fluid compressibility.

Regarding controller performance, the results demonstrate the control strategy's robustness to variations in model parameters and external disturbances. This robustness, combined with its strong tracking performance, suggests that the controller is well-suited for deployment on a real crane and holds promise for automated logging tasks. The next logical step would be to implement the controller on real hardware and test it on the crane.

During trajectory tracking, high-frequency and high-amplitude oscillations in the hydraulic force were observed. One possible solution to mitigate these oscillations and improve overall tracking performance would involve redesigning the controller for the full model, incorporating the dynamics of the hydraulic accumulators. Another option could be modifying the experimental setup by removing the hydraulic accumulators and comparing the results with and without them. Finally, alternative control strategies, such as model predictive control or first- and second-order sliding mode control, could be explored to further enhance tracking performance.

Die approbierte gedruckte Originalversion dieser Diplomarbeit ist an der TU Wien Bibliothek verfügbar
The approved original version of this thesis is available in print at TU Wien Bibliothek.
TU Bibliothek Your knowledge hub WIEN

Bibliography

[1] R. Visser and O. F. Obi, "Automation and robotics in forest harvesting operations: Identifying near-term opportunities," *Croatian journal of forest engineering*, vol. 42, no. 1, pp. 13–24, Aug. 2020, doi: https://doi.org/10.5552/crojfe.2021.739.

[2] A. Halme and M. Vainio, "Forestry robotics - why, what and when," in *Autonomous Robotic Systems*. Springer London, 1998, pp. 149–162, doi: https://doi.org/10.1007/bfb0030804.

[3] P. La Hera and D. Ortíz Morales, "Model-based development of control systems for forestry cranes," *Journal of Control Science and Engineering*, vol. 2015, no. 1, p. 256 951, 2015, doi: https://doi.org/10.1155/2015/256951.

[4] Palfinger, *Controlling the tip of the crane more efficiently and intuitively*, May 2021. eprint: https://www.palfinger.com/en/news/controlling-the-tip-of-the-crane-more-efficiently-and-intuitively_n_874536. (visited on 11/10/2024).

[5] Hydrauliska Industri AB, *Crane tip control taking ease of use to a new level*, Jul. 2020. eprint: https://www.hiab.com/en/media/newsroom/hiab-crane-tip-control. (visited on 11/10/2024).

[6] P. La Hera, O. Mendoza-Trejo, H. Lideskog, and D. O. Morales, "A framework to develop and test a model-free motion control system for a forestry crane," *Biomimetic Intelligence and Robotics*, vol. 3, no. 4, p. 100 133, Dec. 2023, doi: https://doi.org/10.1016/j.birob.2023.100133.

[7] P. L. Hera, U. Mettin, I. R. Manchester, and A. Shiriaev, "Identification and control of a hydraulic forestry crane," *IFAC Proceedings Volumes*, vol. 41, no. 2, pp. 2306–2311, 2008, doi: https://doi.org/10.3182/20080706-5-kr-1001.00389.

[8] D. O. Morales, S. Westerberg, P. La Hera, U. Mettin, L. B. Freidovich, and A. S. Shiriaev, "Open-loop control experiments on driver assistance for crane forestry machines," in *2011 IEEE International Conference on Robotics and Automation*, Shanghai, China: IEEE, May 2011, pp. 1797–1802. [Online]. Available: https://doi.org/10.1109/icra.2011.5980266.

[9] A. Hansson and M. Servin, "Semi-autonomous shared control of large-scale manipulator arms," *Control Engineering Practice*, vol. 18, no. 9, pp. 1069–1076, Sep. 2010, doi: https://doi.org/10.1016/j.conengprac.2010.05.015.

[10] N. D. Manring and R. C. Fales, *Hydraulic Control Systems*. Wiley, Sep. 2019, doi: https://doi.org/10.1002/9781119418528.

Die approbierte gedruckte Originalversion dieser Diplomarbeit ist an der TU Wien Bibliothek verfügbar
The approved original version of this thesis is available in print at TU Wien Bibliothek.
TU Bibliothek Your knowledge hub WIEN

[11] P. La Hera, B. Ur Rehman, and D. Ortiz Morales, "Electro-hydraulically actuated forestry manipulator: Modeling and identification," in *2012 IEEE/RSJ International Conference on Intelligent Robots and Systems*, Vilamoura-Algarve, Portugal: IEEE, Oct. 2012, pp. 3399–3404. [Online]. Available: https://doi.org/10.1109/iros.2012.6385656.

[12] C. Vazquez, S. Aranovskiy, L. Freidovich, and L. Fridman, "Second order sliding mode control of a mobile hydraulic crane," in *53rd IEEE Conference on Decision and Control*, Los Angeles, CA, USA: IEEE, Dec. 2014, pp. 5530–5535. [Online]. Available: https://doi.org/10.1109/cdc.2014.7040254.

[13] W. Kemmetmüller, *Regelungstechnik Seminar (SS 2013)*. Institut für Automatisierungs- und Regelungstechnik, TU Wien, 2013.

[14] G. Bauer and M. Niebergall, *Ölhydraulik: Grundlagen, Bauelemente, Anwendungen*. Springer Fachmedien Wiesbaden, 2020, doi: https://doi.org/10.1007/978-3-658-27027-8.

[15] Palfinger, *The new generation 3*. eprint: https://www.palfingerepsilon.com/00%20Prospekte/Generation%203/KP-PR102%20M3%20-%20EN_low.pdf. (visited on 11/10/2024).

[16] TTControl, *TTC 580 Datasheet*. eprint: https://www.ttcontrol.com/sites/default/files/documents/TTControl-HY-TTC_580-Datasheet.pdf. (visited on 11/10/2024).

[17] Parker-Hannifin Corporation, *K220LS Mobile Directional Control Valve*. eprint: https://www.parker.com/literature/HY17-8537-UK_K220.pdf. (visited on 11/10/2024).

[18] W. Kemmetmüller and A. Kugi, *Skriptum zur VU Modellbildung (SS 2023)*. Institut für Automatisierungs- und Regelungstechnik, TU Wien, 2023.

[19] M. Jelali and A. Kroll, *Hydraulic Servo-systems*. Springer London, 2003, doi: https://doi.org/10.1007/978-1-4471-0099-7.

[20] D. MacCloy and H. R. Martin, *Control of fluid power, Analysis and design* (@Ellis Horwood series in engineering science), 2., (rev.) ed. Ellis Horwood, 1980.

[21] V. V. Syčev, *The differential equations of thermodynamics*, 2. ed., rev. Mir Publ., 1992.

[22] G. Kluge and G. Neugebauer, *Grundlagen der Thermodynamik* (Spektrum-Lehrbuch). Spektrum, Akad. Verl., 1994.

[23] J. S. Cundiff, *Fluid power circuits and controls, Fundamentals and applications* (Mechanical engineering series). Boca Raton, FL: CRC Press, 2002.

[24] S. Aranovskiy and C. Vazquez, "Control of a single-link mobile hydraulic actuator with a pressure compensator," in *2014 IEEE Conference on Control Applications (CCA)*, Juan Les Antibes, France: IEEE, Oct. 2014, pp. 216–221. [Online]. Available: https://doi.org/10.1109/cca.2014.6981354.

[25] O. Nelles, *Nonlinear System Identification*. Springer Berlin Heidelberg, 2001, doi: https://doi.org/10.1007/978-3-662-04323-3.

Die approbierte gedruckte Originalversion dieser Diplomarbeit ist an der TU Wien Bibliothek verfügbar
The approved original version of this thesis is available in print at TU Wien Bibliothek.
TU Bibliothek Your knowledge hub WIEN

[26] C. Bohn and H. Unbehauen, *Identifikation dynamischer Systeme*. Springer Fachmedien Wiesbaden, 2016, doi: https://doi.org/10.1007/978-3-8348-2197-3.

[27] L. Ljung, *System identification* (Prentice Hall information and system sciences series), 2nd ed. Upper Saddle River, N.J.: Prentice Hall, 1999.

[28] M. Gevers and G. Li, *Parametrizations in Control, Estimation and Filtering Problems: Accuracy Aspects*. Springer London, 1993, doi: https://doi.org/10.1007/978-1-4471-2039-1.

[29] A. V. Oppenheim, *Discrete-time signal processing* (Always learning), Third edition, Pearson New international edition, R. W. Schafer, Ed. Harlow: Pearson, 2014.

[30] A. Kugi, *Skriptum zur VU Automatisierung (WS 2019)*. Institut für Automatisierungs- und Regelungstechnik, TU Wien, 2019.

[31] Bosch Rexroth, *Pilot-operated directional control valves, Type 4WRLE*. eprint: https://www.boschrexroth.com/media/7e391226-f2a7-4bfc-b8f3-52e2a3142e8b. (visited on 12/15/2024).

[32] G. James, D. Witten, T. Hastie, and R. Tibshirani, *An Introduction to Statistical Learning: with Applications in R*. Springer US, 2021, doi: https://doi.org/10.1007/978-1-0716-1418-1.

[33] T. Hastie, R. Tibshirani, and J. Friedman, *The Elements of Statistical Learning*. Springer New York, 2009, doi: https://doi.org/10.1007/978-0-387-84858-7.

[34] HAWE Hydraulik, *2-way fow control valves type SB, SQ*. eprint: https://productfinder.hawe.com/downloads/D6920-01-en.pdf. (visited on 11/12/2024).

[35] A. Steinböck, *Skriptum zur VU Optimierung (WS 2024)*. Institut für Automatisierungs- und Regelungstechnik, TU Wien, 2024.

[36] J. Diwold, B. Kolar, and M. Schöberl, "Discrete-time flatness-based control of a gantry crane," *Control Engineering Practice*, vol. 119, p. 104 980, Feb. 2022, doi: https://doi.org/10.1016/j.conengprac.2021.104980.

Die approbierte gedruckte Originalversion dieser Diplomarbeit ist an der TU Wien Bibliothek verfügbar
The approved original version of this thesis is available in print at TU Wien Bibliothek.
TU Bibliothek Your knowledge hub WIEN

Declaration of the Use of Generative AI Tools

I declare that I have used generative AI tools only as an aid, with my own contributions predominating in this work.

Die approbierte gedruckte Originalversion dieser Diplomarbeit ist an der TU Wien Bibliothek verfügbar
The approved original version of this thesis is available in print at TU Wien Bibliothek.
TU Bibliothek Your knowledge hub WIEN

Eidesstattliche Erklärung

Hiermit erkläre ich, dass die vorliegende Arbeit gemäß dem Code of Conduct - Regeln zur Sicherung guter wissenschaftlicher Praxis (in der aktuellen Fassung des jeweiligen Mitteilungsblattes der TU Wien), insbesondere ohne unzulässige Hilfe Dritter und ohne Benutzung anderer als der angegebenen Hilfsmittel, angefertigt wurde. Die aus anderen Quellen direkt oder indirekt übernommenen Daten und Konzepte sind unter Angabe der Quelle gekennzeichnet. Die Arbeit wurde bisher weder im In- noch im Ausland in gleicher oder in ähnlicher Form in anderen Prüfungsverfahren vorgelegt.

Wien, January 2025

Amanzhol Salykov

Die approbierte gedruckte Originalversion dieser Diplomarbeit ist an der TU Wien Bibliothek verfügbar
The approved original version of this thesis is available in print at TU Wien Bibliothek.
TU Wien Bibliothek Your knowledge hub